OPTIMISATION OF METHODS FOR SNOW AVALANCHE DETECTION IN SAR IMAGES

Supporting the development of snow avalanche mapping and monitoring of Svalbard

TU Delft Delft University of Technology

D.S. Wesselink

August 2015

Slab avalanche at Lindholmhøgda, Svalbard
Image courtesy of Jelte van Oostveen - 20 March 2015

Optimisation of Methods for Snow Avalanche Detection in SAR images

Supporting the development of snow avalanche mapping and monitoring of Svalbard

Master of Science Thesis

Submitted in partial fulfilment of the degree of Master of Science
in Geoscience and Remote Sensing at Delft University of Technology

D.S. (Dieuwertje) Wesselink

August, 2015

Faculty of Civil Engineering and Geosciences · Delft University of Technology

The work described in this thesis was carried out at the department of Geoscience and Remote Sensing of the Delft University of Technology in the Netherlands and at the Northern Research Institute Tromsø in Norway.

dswesselink@gmail.com

‘花鳥風月’

Table of Contents

List of Figures

List of Tables

Preface

Without knowing what was ahead of me I joined Jelte on the crazy adventure to Tromsø last October. While being on fieldwork in Iceland I figured that I actually preferred being more outdoors and maybe even living outside of the Netherlands. Jelte's PhD gave me a chance to chase that dream. After returning from Iceland we packed all our stuff and within three weeks we were on the other side of the Arctic Circle.

While exploring my options for master theses in Tromsø, I came across NORUT (Northern Research Institute Tromsø). I have been very lucky that Eirik Malnes offered me a project at NORUT combining two of the greatest things; snow and remote sensing. With little knowledge about snow and snow avalanches, except for snowboarding during winter holidays, I started the project. The idea was to improve snow avalanche detection by using satellite data to create a safer environment in mountainous regions. To be able to execute an engineering thesis with such a social value sounded very appealing to me. Back in the Netherlands it was very easy to convince Roderik Lindenbergh to supervise me. And so the thesis journey started little over nine months ago.

Like usual writing a thesis goes with ups and downs, but it would not have been a success without the guidance of my supervisors. Many thanks goes to Eirik, who has taught me so much about snow avalanche detection and has always been helpful to answer or discuss my questions. Also plenty of thanks to Roderik for supervising me via e-mail (with a very high response time) and a few Skype discussions. Thanks also to NORUT for hosting me during all these months and for i.e. taking me up to Ny-Ålesund on Svalbard where I had the best time as a fieldwork assistant. Moving to Tromsø has opened many doors. Most of them I could not have imagined a year ago (such as field days in the snow, -30^oC and 79^{o}North).

Last but not least, special thanks to my friends and family (my mom, my dad and Lenie, and my awesome big brothers Marnix, Vincent en Edzard (I still look up to you guys...)) for supporting me in my decision to move to Tromsø and explore what I like to do best. Despite the fact that living in the high North meant less real-life contact.

And final finally, very special thanks to Jelte for keeping me sane, especially during the last few hectic weeks. I am grateful for the adventurous trips we have already made and the once still ahead of us. Because there will be plenty.

Dieuwertje Wesselink, Tromsø, August 15, 2015

Executive summary

Avalanches form a threat to people travelling in mountainous regions as well as for infrastructure and buildings. They cause around 250 fatalities annually worldwide (Schweizer, 2008). Avalanche research is needed to get a more profound understanding of the avalanche activity in space and time. Just like other inhabited, mountainous regions worldwide, the infrastructure and people living and travelling in and around Svalbard's main settlement area Nordenskiöld Land are directly affected by both naturally and artificially triggered avalanches. According to Norwegian Geotechnical Institute (2015) over 60 people passed away in the last ten years in Norway and Svalbard due to fatal avalanches. To limit the number of future fatalities, forecasting services are interested in knowledge on avalanche activity in space and time to verify their warning system. They rely on information about the frequency, location and extent of debris fields, as provided by avalanche experts.

As avalanche terrain is mostly remote and inaccessible, it can be dangerous or even impossible to obtain necessary field information on avalanche events. It is especially crucial to gain this information during strong winds and blowing snow when an increased avalanche danger is present. By applying satellite technology, large areas can be monitored at once with both a high spatial resolution and a high acquisition frequency. Specifically, satellite-borne Synthetic Aperture Radar (SAR) has the advantage of being daylight and weather independent. The area of interest, Nordensköld Land, experiences over four months of polar darkness per year. Consequently, the most applicable technique for avalanche monitoring is SAR.

Avalanche debris has an increased surface roughness and snow density compared to the surrounding unperturbed snow causing a higher backscatter signal. Therefore the debris fields appear bright in SAR images. Manual detection of avalanches in these images has already been proven to be successful by Eckerstorfer et al. (2014b). This can be, however, a very time-consuming task when dealing with large avalanche cycles where up to 400 debris fields are located in a single image. The main goal of this research project is to optimise avalanche detection in SAR images by exploring the option of automatic detection of avalanche debris fields.

Hence, we present a method to automatically detect avalanche debris fields in SAR images. It is designed and tested on both RADARSAT-2 Ultra Fine (UF) mode and Sentinel-1A Extra Wide swath (EW) mode images covering Nordensköld Land. Sentinel-1A has the advantage of obtaining images twice per day over Svalbard and is made available for free. Due to the high costs to acquire RADARSAT-2 data over Svalbard, the images have a low acquisition

frequency. The UF mode images are geocoded to a pixel spacing of $3m$ compared to $40m$ for the EW mode images. Both modes detect the location of debris fields, but the extent is only clearly distinguishable in the UF mode images.

In case of automatic detection, the backscatter coefficient of the debris fields is compared to the backscatter coefficient from a reference image. This reference image should be obtained during dry snow conditions or during a snow-free summer. The difference in backscatter coefficient between the two images is determined by subtracting the reference image from the avalanche image. By applying a threshold value on the difference image the debris fields are successfully located. However, their also exists areas where the difference between avalanche and reference image is above the threshold value, but are noise instead of debris fields. These pixels are false alarms and need to be eliminated by a filter.

Automatic detection using a median filter is applied to the ascending RADARSAT-2 'VV'-polarised images in UF mode. This leads to 100% probability of detection for threshold values of $1.9dB$ or below and over 50 false alarms. Using a Remove Small Objects (RSO) filter instead of a median filter results in a lower detectability, but also in less false alarms; 69% and over 20 false alarms. By applying automatic detection using a RSO filter and threshold value of $3.4dB$ on the descending Sentinel-1A EW mode images in 'HV'-polarisation, 100% of the debris fields were detected, but at the expense of 13 false alarms.

None of the designed automatic detection methods resulted in a 100% probability of detection and zero false alarms, but they do confirm that automatic detection of avalanches in these SAR images is possible. They also show that the automatic detection method is depended on the characteristics of the input data. For the RADARSAT-2 UF mode images the best result is obtained by using a median filter and a threshold value of $1.9dB$, while for the Sentinel-1A EW mode images a RSO filter in combination with a threshold value of $3.4dB$ resulted in the optimum detection. By combining a regular detection of the whole of Svalbard by the coarse Sentinel-1A EW mode images and a more specified forecasting using the fine RADARSAT-2 UF mode images avalanche maps can be created indicating both location and extent of debris fields. These maps can be of great value for avalanche warning services, although further research is necessary before automatically generated avalanche maps can be included in daily operations.

Chapter 1

General introduction and project setup

Whether human or naturally released, snow avalanches cause road closures, community evacuations and around 250 fatalities annually worldwide (Schweizer, 2008). They mostly occur in snow covered mountainous regions. According to Norwegian Geotechnical Institute (2015) over 60 people passed away in the last ten years in Norway and Svalbard due to a fatal avalanche. The need to develop a method to monitor and map avalanche activity therefore strongly exists. Besides, there is a big potential to improve operational avalanche warning services. Although efforts have been made to reduce the number of fatalities and the damage of infrastructure by protection structures, improving the understanding of avalanche activity in space and time is still necessary.

In the last decades research has been conducted on avalanche detection using different kind of methods and techniques. As avalanche terrain is mostly remote and inaccessible, it can be dangerous or even impossible to obtain necessary information. Optical and radar remote sensing sensors can be used to monitor avalanche events. These can be either ground-based or deployed on airborne or spaceborne platforms; each combination having its advantages and disadvantages.

In January 2015, an avalanche has taken the life of a snowmobile driver in Fardalen near Longyearbyen on Svalbard. Longyearbyen is the main settlement on Svalbard and has a population of little over 2000 people. The archipelago of Svalbard is located between 74^o and 81^o north latitude and 10^o to 35^o east longitude in the Arctic Ocean - see Figures 1.1 and 1.2. The warm Gulf Stream causes Svalbard to have a rather mild Arctic climate making the area to be habitable. The islands groups are relatively easy accessible and therefore also attractive for researchers. This incident stresses the need for avalanche research. The area around Longyearbyen is called in Nordenskiöld Land and will be the area of interest for this research project. A topographic map of Nordenskiöld Land is presented in Figure 1.3.

As Svalbard experiences polar night for almost four months per year, satellite radar remote sensing is an applicable technique to identify avalanche debris fields. Important for avalanche monitoring are the spatial and temporal coverage of the satellite. The accuracy of the extent and the estimation of the release date of the avalanche is improved by a high spatial and a

Figure 1.1: Topographic map of Svalbard relative to Norway (Malone, 2014). The red square indicates Svalbard.

Figure 1.2: Topographic map of Svalbard (Norwegian Polar Institute, 2015). The red square indicates Nordenskiöld Land.

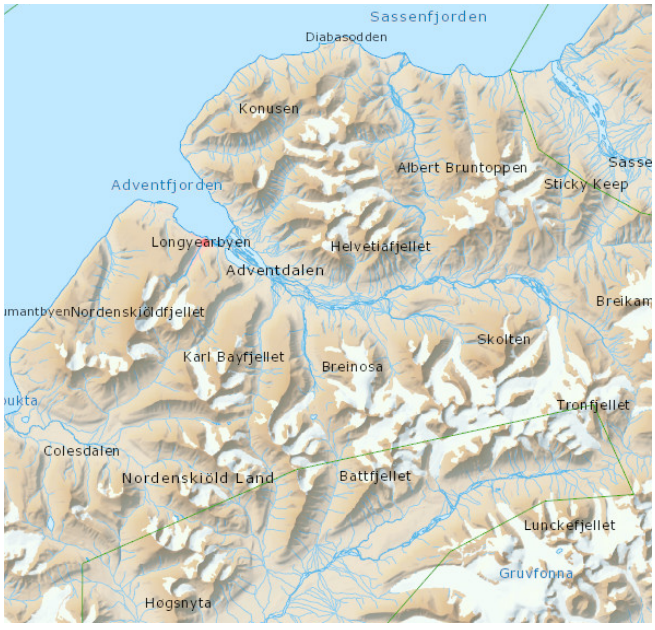

Figure 1.3: Topographic map of Nordenskiöld Land on Svalbard, which is the area around the main settlement Longyearbyen. The map is obtained from toposvalbard.npolar.no (Norwegian Polar Institute, 2015).

high acquisition frequency, respectively. Nordenskiöld Land is covered by both RADARSAT-2 and Sentinel-1A satellites. RADARSAT-2 can obtain images with a pixel spacing of $3m$ in Ultra Fine (UF) mode, but is very costly to acquire images daily. It has a repeat cycle of 24 days (Canadian Space Agency, 2011). On the other hand, the images obtained by Sentinel-1A have a pixel spacing of $40m$ in Extra Wide swath (EW) mode and a repeat cycle of 12 days. The satellite passes Nordenskiöld Land twice per day; during descending and ascending track, and thus has a high acquisition frequency.

In the following sections the problem statement and the outline of this thesis are discussed to present the goals and to give an overview of the work carried out during this project. In Section 1.1 the main research question and the subquestions are presented which are defined by the motivation and objectives for executing the project. The reading guidance for this thesis is given in Section 1.2.

1.1 Problem statement

The motivation for carrying out this research project is to get a profound understanding of avalanche formation in space and time. Information on the avalanche activity is one of the gaps in avalanche research as identified by Buhler et al. (2014). The motivation is further elaborated on in Subsection 1.1.1. The research questions designed to carry out the project are presented in Subsection 1.1.2.

1.1.1 Motivation and objectives

Both naturally and artificially triggered avalanches directly affect the infrastructure and people living and travelling in and around Svalbard's main settlement Longyearbyen. Crucial in basic avalanche hazard assessment and warning is the knowledge of avalanche activity in space and time in a given region. Avalanche terrain is commonly remote and inaccessible and in combination with poor weather conditions or high avalanche danger it can be impossible at times to acquire the necessary information.

Buhler et al. (2014) conducted a study to assess the technical feasibility and commercial viability of improving the European avalanche warning services by applying satellite technology. Three user groups were identified who are interested in avalanche monitoring systems: National and regional warning services, alpine services and the general public. They also identified several gaps in the avalanche research of which the three most important ones are information on avalanche activity, snow surface and snow pack stability. Each one having a different ideal coverage, temporal and spatial resolution.

For this research project, the focus lies on obtaining information on the avalanche activities. Especially information on the location of the avalanches can be useful in bad weather conditions or critical snow situations. Buhler et al. (2014) also investigated available technologies to close the information gaps within avalanche research. An useful operational product for monitoring avalanche activity is based on terrestrial radars which enables real-time detection of avalanches. However, these sensors only cover smaller areas. Avalanche events can also be mapped by optical and radar satellite data which cover larger areas at once. A disadvantage of optical sensors is their dependency on clear sky conditions. Radar satellite remote sensing

does not suffer from weather or light dependency as the microwave signals can penetrate through clouds.

According to Eckerstorfer et al. (2014b) satellite-borne radar remote sensing, i.e. Synthetic Aperture Radar (SAR) images, can be used to detect and map avalanches. They have proven that RADARSAT-2 UF mode images are sufficient enough to manually detect avalanches. However, as manual detection of avalanches can be labour intensive and too time-consuming, automated detection of avalanche debris is advised. The main problem of using RADARSAT-2 data is the low temporal resolution. On the other hand, the temporal resolution of the Sentinel-1A is very beneficial for avalanche detection. A recent study by Malnes et al. (2015) shows successful manual detection of avalanches in Sentinel-1A Interferometric Wide swath (IW) images and hopeful results for automatic detection. However, for Svalbard Sentinel-1A only provides regularly images in EW mode. Thus this research project is designed to test whether the spatial resolution of EW mode images is sufficient for both manual and automatic detection.

The following goals are expressed as the project objectives. They are based on the preceding motivation for carrying out this research.

- Familiarise with methods for avalanche detection using a selection of RADARSAT-2 images.
- Evaluate manual detection methods by comparison of the results using different imaging modes, i.e. RADARSAT-2 UF, ScanSAR Narrow (SCNA) and ScanSAR Wide (SCWA) beam mode.
- Design automatic detection methods for RADARSAT-2 and Sentinel-1A images.
- Evaluate and optimise the automatic detection methods.

1.1.2 Research question and subquestions

The objectives and goals listed in the previous subsection can be translated into the following main research question:

To what extent is automatic detection of snow avalanches possible from Synthetic Aperture Radar amplitude data?

The main research question is divided into several subquestions, which are split up into three groups and listed below.

Available methods to detect avalanches

- What kind of methods for mapping and monitoring of snow avalanches are currently available? And what are their advantages and disadvantages?
- Which technique suits best for avalanche detection on Svalbard? And why?
- How would automatic detection of avalanches in SAR images be helpful for avalanche research?

Automatic detection of debris fields in SAR images

- How can avalanches be automatically detected in SAR images?
- Is it possible to detect avalanches automatically in RADARSAT-2 UF mode images having a pixel spacing of $3m$? And in Sentinel-1A EW mode images having a pixel spacing of $40m$?
- What are the conditions/limitations of the method(s)?

Validation of automatically detected avalanches

- What is the probability of detection of avalanche debris fields by the designed automatic detection method(s)? And what is the difference between RADARSAT-2 and Sentinel-1A?
- How can the results be assessed and validated?

By answering these questions the understanding of avalanche activity in time and space is improved and using this the automatic detection of avalanche debris fields in SAR images can be optimised. Each chapter covers one or several of the subquestions.

1.2 Thesis outline

In order to study the detection of avalanche debris fields a basic background on avalanche characteristics and formation is needed. Chapter 2 gives the relevant basics of avalanches with a focus on the avalanche climate on Svalbard and the available terrestrial, airborne and spaceborne techniques are discussed. The chapter concludes with a section on what sensor and platform combination is used for this research project. The radar system theory, processing of radar data and the use of SAR for avalanche detection is presented in Chapter 3. Subsequently, the available data, e.g. radar data and meteorological data, is given in Chapter 5. Stated in Chapter 4 is an overview of the workflow on how to obtain the final results and the outline of the designed automatic detection method. Chapter 7 shows the application of the workflow on the available RADARSAT-2 and Sentinel-1A images. The results are both presented and discussed in this chapter as the detection is an iterative process; the analysis of the manual detection forms the input for the automatic detection and the assessment of the automatic detection helps in optimising the automatic detection method. Finally, the key findings and suggestions for further research are discussed in Chapter 8.

1.3 Support

The research project as defined in this thesis is a collaboration between the *Geoscience and Remote Sensing (GRS)* department at the Delft University of Technology (TU Delft) and the *Northern Research Institute (NORUT)* in Tromsø. This Norwegian institute conducts research relevant to the High North within the fields of technology and social science commissioned for private and public sectors. NORUT exists of several departments of which cooperation has been established with the 'Remote Sensing, Satellites and UAS'.

Chapter 2

Background on snow avalanches and monitoring techniques

Every year Svalbard experiences a large number of snow avalanches, hereafter called avalanches. This Norwegian archipelago is located in the Arctic Ocean and has a population of little over 2600 people. On January 24^{th}, 2015, an avalanche in Fardalen near Longyearbyen took the life of a snowmobile driver (NRK, 2015). Besides fatalities, large avalanches pose a hazard to the infrastructure as well. This chapter presents the necessary background on avalanches and their formation, especially on Svalbard. Section 2.1 introduces different types of avalanches and snow climates. The avalanche climate on Svalbard is discussed in Section 2.2. Regardless their type all avalanches can be categorised by both a destructive- and relative-size scale system as explained in Section 2.3. Section 2.4 deals with the assessment of the avalanche danger and forecasting. For the forecasting knowledge of historic avalanche activity is crucial and thus there different kinds of mapping techniques have been developed in the last century. These instruments can be either ground-based, airborne or spaceborne and are presented in Sections 2.5, 2.6 and 2.7, respectively.

2.1 Types of avalanches and snow climates

Avalanches are rapid snow mass movements occurring in snow covered mountainous areas worldwide. The topographical and meteorological conditions as well as the mechanical properties of snow make avalanche release a complex process. A distinction can be made between *loose and slab avalanches* and *dry and wet snow* avalanches (McClung and Schaerer, 2011). Most of the fatalities are caused by slab avalanches, where a cohesive slab on top of a sliding surface or weak layer gets released. Weak layers are distinguished by being relatively less cohesive than the other layers within the snowpack. The various layers are formed by different precipitation events and by the influence of wind. Solar radiation and air temperature cause melting/refreezing and snow metamorphism within the snowpack. Temperature changes and additional loading, i.e. a skier, a snowmobile or precipitation, can cause a fracture to be

initiated in the weak layer. If the fracture propagates it can trigger an avalanche. Whether the crack propagates and to what extent depends on the snowpack properties, e.g. Snow Water Equivalent (SWE), temperature, grain type and size.

Figures 2.1 and 2.2 show respectively a slab avalanche at Lindholmhøgda on Svalbard and the debris of a slab avalanche in Skavskogen nearby Tromsø in Norway. Visualised in the upper figure are the crown, bed surface and avalanche path. The latter one is the fixed terrain wherein a possible avalanche can occur and move. The bed surface is the surface on which the slab slides. This can be a weak layer within the snowpack or the ground surface. The crown face is the top periphery of the slab and has an angle of 90° to the bed surface. In general slab avalanches occur on slopes with an angle between $25{\sim}55^o$. However, human released avalanches are mostly located on terrain with a slope angle between $35{\sim}45^o$ (McClung and Schaerer, 2011).

Varying climatic conditions which are referred to as snow climates cause different types of snow and thus avalanches. It is important to classify the *snow avalanche climate* as it characterises the type of avalanches occurring in that area. The three following types of snow climates can be distinguished, each having their own characteristics and avalanche potential (McClung and Schaerer, 2011).

- Maritime
  The coastal mountainous areas, i.e. western United States and Norway, have a maritime snow climate with mild air temperatures. This results in heavy snowfall and thus a thick and consistent snowpack that gets affected by rainfall events characteristic for this climate type.
- Continental
  Areas located at higher elevation and more inland, i.e. the Alps, have a continental snow climate. The conditions are characterised by lower air temperatures resulting in less snowfall. Therefore the snowpack is relatively shallow. The fluctuation in air temperature throughout the season causes a variety of layers within the snowpack.
- Transitional
  The inter-mountainous areas, i.e. the Columbia mountains, have a transitional snow climate. The snow depth is intermediate and although it is characterised by mild air temperatures, it does not experience as much rain events as in a maritime snow climate.

There also exist exceptions where coastal areas have a continental snow climate, and vice versa. The formation of avalanches differs per region due to these varying snow climates and thus demanding a specified forecast for each area. In case of a continental snow climate the major avalanches are caused by a combination of certain weather conditions and buried structural weaknesses. In a maritime snow climate these buried structural weaknesses are not so common, as the snowpack is deep and relatively warm. However, rainfall could result in ice layers that act as sliding planes for slabs. More on the snow avalanche climate on Svalbard can be found in Section 2.2.

2.2 Avalanche climate on Svalbard

Due to the meteorological maritime influence Svalbard experiences a rather mild climate compared to other high Arctic locations. Eckerstorfer and Christiansen (2011a) defined the

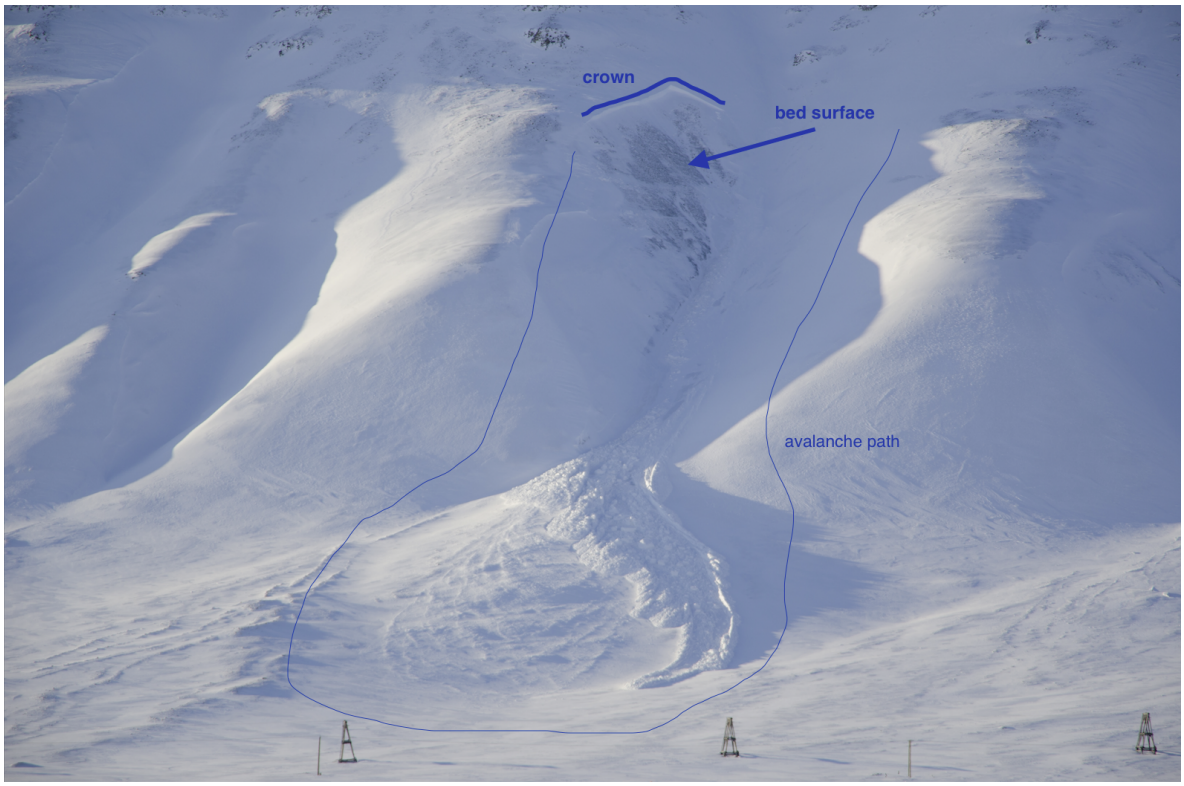

Figure 2.1: Photograph of a slab avalanche at Lindholmhøgda on Svalbard. This avalanche is classified as D2-R2 according to the scale system defined by Greene et al. (2010). 20 March 2015, © *Jelte van Oostveen*.

Figure 2.2: Photograph of slab avalanche debris in Skavskogen nearby Tromsø in Norway. 15 January 2015, © *Dieuwertje Wesselink*.

climate on Svalbard as a *High Arctic maritime snow climate*. The snowpack on Svalbard very thin due to the low air temperatures and little precipitation. Often a layer of cup-shaped crystals called *depth hoar* can be found at the bottom with icy layers and wind slabs on top. Depth hoar forms due to large temperature gradients within the snowpack and due to its poor crystal bonding it is considered as a weak layer. Large temperature gradients are common in Svalbard's thin snowpacks due to the relatively warm permafrost ground and cold snow surface (low air temperatures). As depth hoar is relatively strong in compression, it often fails in either shear or collapses.

The landscape of Svalbard is characterised by high relief mountains - see Figure 2.3 and 2.4. For at least eight months a year the higher grounds and areas more inland are covered by snow. The semi-permanent Siberian high pressure and Icelandic low pressure systems cause a prevailing wind direction from the southeast (Eckerstorfer and Christiansen, 2011b). In combination with the typical topography and the lack of vegetation the prevailing wind cause the formation of cornices. A *cornice* is an overhanging mass of snow deposited by the wind usually formed on ridge crests. *Cornice falls* can easily trigger slab avalanches and are common on Svalbard. The starting zone of avalanches released by cornice falls have a rather high slope angle as their fracture line is close to the ridge (Eckerstorfer et al., 2014a).

2.3 Destructive- and relative-size classification of avalanches

The destructive potential of avalanches is expressed by a classification system based on the path length, the mass and the impact pressure. Table 2.1 shows the *destructive-size scale* system that originates from Canada. Five categories (D1∼D5) are distinguished; starting from avalanches with small destructive potential by being relatively harmless to people, up to the largest avalanches known which are able to destroy complete villages. The mass in tonnes defines the size of the avalanche and covers the amount of snow released in the starting zone plus the amount entrained or deposited during downslope motion (McClung and Schaerer, 2011). To complete the classification a *relative-size scale* (R1∼R5) is introduced as well shown in Table 2.2. This scale denotes the size of the avalanche relative to the path from being very small up to maximum (Greene et al., 2010, Chapter 3). For the class 'maximum relative to path' the complete potential avalanche path is covered. Using these scale systems it is easy to quickly classify avalanches in the field. As an example, the slab avalanche presented in Figure 2.1 can be classified as D2-R2. To express the potential danger of avalanches a different scale system is used, called the avalanche danger scale.

2.4 Avalanche danger assessment and forecasting

The prediction of occurrence or forecasting of avalanches is highly uncertain as it is impossible yet to determine the exact trigger of an avalanche. Improvements on the forecasting can be made by close monitoring avalanche dangerous areas. To minimise the uncertainty regarding the instability of the snowpack attempts on avalanche forecasting are being made (McClung, 2002). Through avalanche bulletins the avalanche danger level is communicated to the public. The avalanche danger level indicates the snowpack stability and the avalanche triggering probability. The danger scale is divided into five levels; Low (1) to Extreme (5), where a

Figure 2.3: Photograph of Colletthøgda and Kronebreen (glacier) showing plateau mountains characteristic for Svalbard. Clearly visible are the gullies where avalanches can slide down through. 27 May 2015, © *Dieuwertje Wesselink*.

Figure 2.4: Photograph of Longyearbyen and characteristic plateau mountains of Svalbard, taken from the South. The mountain on the left shows some cornice formation at the ridge. 4 March 2015, © *Dieuwertje Wesselink*.

Table 2.1: Avalanche destructive-size scale system denoting destructive potential, typical mass and typical path length of avalanche (Greene et al., 2010).

Data Code	Destructive potential	Typical mass	Typical path length
D1	Relatively harmless to people	$< 10t$	$10m$
D2	Could bury, injure, or kill a person	10^2t	$100m$
D3	Could bury a car, destroy a small building, or break a few trees	10^3t	$1{,}000m$
D4	Could destroy a railway car, large truck, several buildings, or a forest with an area up to 4 hectares	10^4t	$2{,}000m$
D5	Largest snow avalanches known; could destroy a village or forest of 40 hectares	10^5t	$3{,}000m$

Table 2.2: Avalanche relative-size scale system denoting size of avalanche relative to path (Greene et al., 2010).

Data code	Relative to path
R1	very small
R2	small
R3	medium
R4	large
R5	maximum

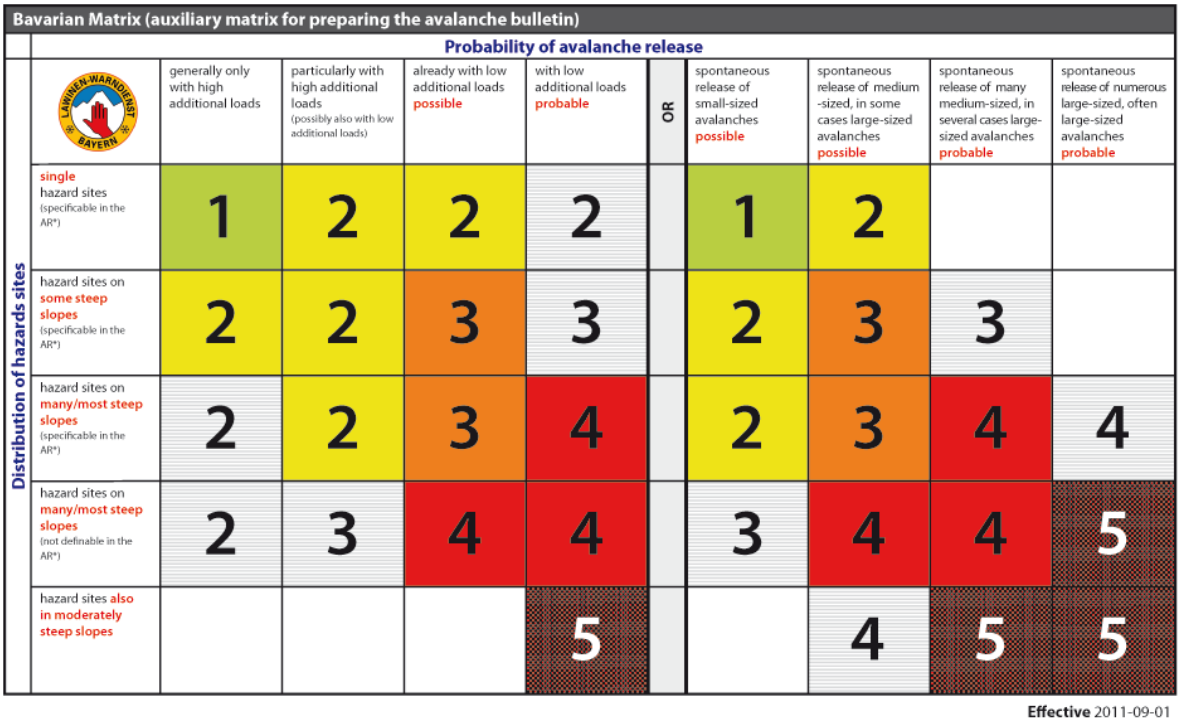

Figure 2.5: Bavarian matrix to determine avalanche danger level based on distribution of hazard sites and probability of avalanche release (European Avalanche Warning Services, 2015).

Figure 2.6: Photograph of a snowpit dug near Longyearbyen on Svalbard. The sticks indicate different layers within snowpack; in total 11 layers were identified with varying thicknesses. 26 February 2015, *© Dieuwertje Wesselink*.

higher danger level means an increase in destructive size and/or an increase of the spatial distribution of the avalanches and/or a decrease in the needed force to trigger them (European Avalanche Warning Services, 2015). Using both meteorological and topographical factors the danger level is assessed. The slope, elevation, aspect, terrain type, surface, precipitation, wind, temperature, radiation and humidity all play a role. As well as the snowpack itself, including the layering, water content, temperature gradient and any persistent weak layers. Although the terrain is rather static, both the weather and snowpack are changing continuously causing the avalanche danger outlook to be changed often.

Even though the avalanche danger scale is a good indication of the existing danger, the system has some drawbacks. Firstly, avalanches can occur in any snow covered terrain. Secondly, the danger level is determined for a larger area, and not for a single slope. This can result in a underestimation of the avalanche danger for some of the slopes within the area and an overestimation for other slopes. Both spatial and temporal dense distributed data is needed for a good assessment. Snow profiles, instability tests, recent avalanche activity and weather data can help in making such an assessment.

Snow profiles are obtained by observing the stratigraphy of the snowpack after digging a snow pit such as the one in Figure 2.6. In a snow profile information about the location, meteorological conditions, temperature throughout the snowpack as well as the grain type, grain size and water content within the various layers is recorded. An example of a snow profile together with an explanation of the contents is presented in Section 5.4.2. To test the instability of the snowpack Extended Column Test (ECT)s, Compression Test (CT)s and/or Rutschblock tests can also be performed. More on these tests can be found in the Snow, Weather and Avalanches Guidelines by Greene et al. (2010).

In order to make the decision on the avalanche danger level easier the Bavarian matrix was introduced in 1993 by the Lawinenwarndienst Bayern and adopted by the European Avalanche Warning Services in 2005. On the axes of the Bavarian matrix, the avalanche trigger probability and the spatial distribution of instability are displayed - see also Figure 2.5. The left side of the matrix uses the sensitivity to trigger, while the right side uses the avalanche size. The danger level increases for higher probabilities of triggering and an increase in spatial distribution of instability. Different types of avalanches could lead to the same danger level.

Crucial in basic avalanche hazard assessment and warning is the knowledge of historic avalanche activity in space and time in a given region (Eckerstorfer et al., 2014b). Since the beginning of the 21^{st} century various kinds of sensors have been explored for both mapping wet snow and detecting avalanches. The forecasting services rely on avalanche activity records including the frequency, location and extent of the avalanche events to assess the safety for roads and ski resorts and verify the warning system. Field observations obtained by individuals, although useful, only provides isolated information and limited coverage. Radar-based techniques can operate independently of daylight and weather conditions and are able to provide temporal and spatially continuous datasets and therefore fill the data gaps. The three sections hereafter discuss the currently used techniques for detecting avalanches.

2.5 Ground-based sensors

One of the available techniques for monitoring avalanches is using time-lapse cameras, where a camera is set-up in the direction of the slope to observe it as long as desired. A disadvantage is that only a small area can be captured at once. Another disadvantage is the weather- and light dependency as bad weather and darkness block the visibility. An advantage of this technique, on the other hand, is that different time intervals can be set and slopes can be monitored frequently to closely capture changes. Even the origin of the avalanches can be recorded (Gauthier et al., 2014).

Another ground-based method is using terrestrial radar. Advantages of ground-based radars are their portability, fast acquisition time and the possibility of making repeat acquisitions within minutes. This way real-time snow information can be provided on a very local basis (Wiesmann et al., 2014). Martinez-Vazquez and Fortuny-Guasch (2008) developed an algorithm for automatic detection and classification of avalanche using ground-based Synthetic Aperture Radar (SAR). The technique is already applied in ski resorts to monitor critical slopes where avalanches form a risk for humans and infrastructure continuously. However, this method has the disadvantage of being limited to single slopes or small areas.

2.6 Airborne platforms

Optical instruments are passive sensors as they measure the solar radiation reflected or scattered from the earth's surface and do not emit radiation themselves. They can be mounted on airborne platforms to obtain moderate coverage. According to Bühler et al. (2009) and Lato et al. (2012) optical remote sensing imagery can be used for automated detection. The extent of the released avalanches can be automatically detected and exactly delineated in very high (sub meter) resolution images. An optical camera can also be mounted on an Unmanned

Airborne Vehicle (UAV). This makes it possible to fly closely over released avalanches, map the extent of the debris fields and calculate their volume (Malnes et al., 2014).

An advantage of using the airborne platform is the possibility to cover larger areas compared to the areas monitored using ground-based methods. However, there are limitations to this technique when it comes to weather conditions; again cloud cover and poor light conditions block the visibility. Also high resolution optical data and the use of airplanes or UAVs is often very costly.

2.7 Spaceborne platforms

According to Malnes et al. (2013) high resolution RADARSAT-2 images can be used to detect avalanches. Due to the high contrast between the low radar backscatter from the unperturbed snow and the high backscatter of the snow avalanche debris, the avalanches can be identified. Although detecting avalanches in very steep topography is difficult due to layover, shadow and foreshortening - explained in Subsection 3.1.1 -, the light and weather independency makes it a convenient technique during the polar night on Svalbard. In addition frequent mapping with variable geometry is available at Svalbard resolving the layover problem. Especially during bad weather periods, when an increased avalanche danger is present and information is crucial, acquisition of data by observers can be difficult and thus using SAR satellites for avalanche observations is useful for this area.

In this chapter various techniques and methods to detect avalanches were presented. Manual detection has successfully been performed on satellite-borne SAR C-band data, but can be a very time-consuming task. Although an automatic detection method using ground-based SAR has already been developed by Martinez-Vazquez and Fortuny-Guasch (2008), it will not be very suitable for obtaining a broad coverage as only a single slope or small area is monitored. Also the mountainous archipelago of Svalbard experiences polar night for almost four months per year and thus spaceborne SAR is applicable for avalanche monitoring. The next chapter will go into detail on radar remote sensing and its use for avalanche detection.

Chapter 3

Radar remote sensing for avalanche detection

This chapter shows the basics of radar remote sensing. Section 3.1 contains the main principles of radar, including Real Aperture Radar (RAR) and Synthetic Aperture Radar (SAR). The latter one is the technique used for this research project. Section 3.2 states the basic processing techniques for SAR images. And finally, the avalanche detection in SAR images is explained in Section 3.3.

3.1 Basic principles of radar

Radio Detection And Ranging (Radar) is an active remote sensing technique; meaning that it both emits and receives electromagnetic signals. The pulses sent out by the radar instrument are electromagnetic waves and have a wavelength in the order of centimetres to one meter. This technique is weather and light independent as the microwave signals are able to penetrate through clouds. Also the wavelength can be adjusted to the desired application. Using a larger wavelength, the penetration depth of the signal increases, but usually at the expense of spatial resolution. The transmitted signal is scattered in all directions when hitting the ground. The return in the direction of the receiver is called echo or *backscatter*. Information on the scattered object or surface can be obtained by recording the power and two-way travel time of the echo. Besides this, radar can also be used to obtain the range, altitude, direction and speed of aircraft, ships, motor vehicles, spacecraft and other objects. A well-known daily used application is the speed control of vehicles.

Mounting the radar on either a space- or airborne vehicle, images with high resolution and broad coverage can be obtained. Radars on space-borne vehicles or satellites can perform repeat passes over fixed areas, which is favourable for monitoring and mapping scattering characteristics and also movement of the earth's surface. The *swath* of the radar is the part of the surface that gets illuminated by the transmitted signal and is highly dependent on the antenna size. For space-borne vehicles, spatial resolutions of around $5{\sim}100m$ can

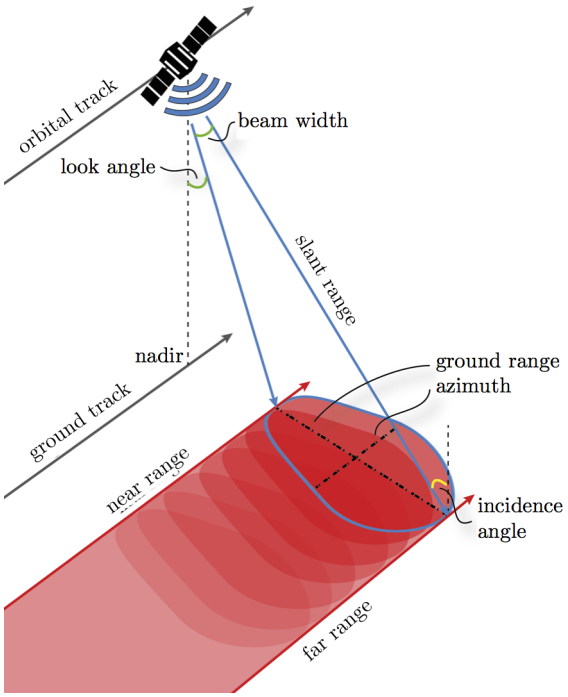

Figure 3.1: Schematic overview of imaging geometry of a side looking satellite-borne radar. In red is shown the swath covered by the satellite.

be obtained as the size of the antenna is limited to what can be carried on a satellite. To improve the resolution, synthetic aperture radars have been developed which will be explained in Subsection 3.1.5.

3.1.1 Side-looking radar viewing geometry and its image distortions

A schematic view of the imaging geometry of a radar acquisition mounted on a satellite is presented in Figure 3.1. The direction in which the radiation beam is transmitted is called the *Line Of Sight (LOS)* and often has a side-looking view. Side-looking views cause the radiation beam to be emitted in across-track or *range* direction, which is perpendicular to the flight or *azimuth* direction. The *spatial resolution* determines the level of detail of the image. The output of the radar range measurements is the *slant range*, which is the distance travelled by the electromagnetic wave from a point to the satellite in across-track direction. The *ground range* is the along-track range distance as projected on the ground. The slant range can be converted to ground range by applying terrain corrections obtained from a Digital Elevation Model (DEM). Due to the side-looking radar terrain elevations cause geometric distortions in the radar image like foreshortening, layover and shadowing.

The slope of a mountain or hill leaning towards the radar illumination is called the foreslope, while the slope pointing away is called the backslope. At a certain incidence angle the emitted pulse will reach the base, slope and top of the foreslope of a mountain at the same time, the slant range of these points will be smaller than they would be on a flat area. This phenomena is *foreshortening*. If the signal arrives at the top of an object before it reaches the bottom, the return signal from the top is received before the one from the base. A reversed order of surface elements on the ground appears in the image. Foreshortening of foreslopes will appear brighter in the radar image due to the superimposition of the slope. To minimise

the effects either a DEM of the area can be used or a larger incidence angle. However, using a larger incidence angle can result in an increase in *shadowing*. Shadowing occurs on backslopes, since no backscattered signal is received from these slopes as they are in the shadow of the topographic elevation. Higher incidence angle cause larger slopes. Due to the lack of backscatter signal, these shadowed areas appear darker in the radar image.

3.1.2 Radar backscatter signal

The radar backscatter coefficient σ_0 is the ratio of the backscattered power given an incident power per unit area - see Equation 3.1. The acquisition conditions are determinative for the backscatter signal. The *incidence angle* is defined as the angle between the incident radar beam and the normal of the ellipsoid at the reflected location, increasing from near to far range of the transmitted beam by a few degrees. The angle between the radar and the normal of the object reflecting the beam is the *local incidence angle* θ. With increasing local incidence angle, the reflected signal from the scattered objects decreases. Note that the angle can also vary per acquisition and for some applications there might be an optimum configuration.

$$\sigma_0 = \frac{\sigma}{A} \tag{3.1}$$

The acquisition conditions are determinative for the radar backscatter signal as they are the scattering characteristics of the surface or object, e.g. earth's surface. Besides the incidence angle, influences the surface roughness and relative permittivity the backscatter signal as well. Equation 3.2 is called the *radar equation* and relates the received power to the transmitted power, radar geometry, scattering properties of the surface and the radar backscatter coefficient (Rees, 2013). The transmitted power P_t and received power P_r are respectively the power transmitted by an antenna with gain G and the power received from an area A of the scattering surface at a distance R. The effective area of the antenna is given by A_e and can be expressed by the wavelength λ, efficiency of the antenna η and its gain - see Equation 3.3.

$$P_r = \frac{A_e G P_t}{(4\pi)^2 \eta R^4} \sigma^0 A \tag{3.2}$$

$$A_e = \frac{\lambda^2 G}{4\pi\eta} \tag{3.3}$$

For perfectly smooth surfaces none of the emitted radiation is reflected back to the antenna, while for rougher surfaces part of the scatter is captured. Thus increasing the *surface roughness* leads to an increase in backscatter signal; rough surfaces appear brighter in radar images than smooth surfaces. Whether a surface is smooth or rough is relative to the wavelength of the signal. As a rule of thumb: surfaces with height variations smaller than one-eight of the radar wavelength are smooth, while surfaces with height variations larger than half of the wavelength are rough. Also note, that for a given wavelength, the surface will appear smoother with increasing incidence angle. An increased backscatter can also be designated to the *relative permittivity* of the material, which describes the effect of the material on an electric field. The permittivity is influenced by the moisture content of a material. For natural vegetation such as soil and snow the dielectric constant increases with moisture content.

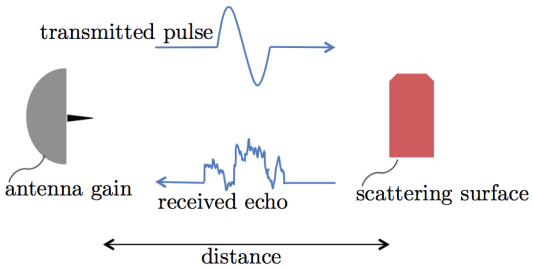

Figure 3.2: Schematic overview of radar equation, where P_t denotes power transmitted by an antenna with gain G and P_r power received from an area A of a scattering surface at distance R.

Varying brightness between pixels with constant backscatter can be due to random positive or negative interference of the electromagnetic waves backscattered from individual scatterers. All individual surfaces and objects within the swath are coherently summed and it appears as *speckle* or 'salt-and-pepper' noise in the image. Speckle can be reduced by for example applying filters.

3.1.3 Image enhancement in radar imaging

To get the required information from a satellite radar image both *contrast modification* and *spatial filtering* can be applied. One way to improve the contrast of the image is by *linear contrast stretching*, where a transfer function relating the output pixel value to the input pixel value is applied. Due to this reassigning of one pixel value to another the shape of the histogram of the image changes. Another method is *histogram equalisation*, where the aim is to ensure that all pixel values occur with equal frequency creating a more or less flat histogram (Rees, 2013). These types of contrast modification can be useful to improve the visibility of certain features in the image, e.g. avalanches debris fields. An example of spatial filtering especially effective for 'salt-and-pepper' noise is using a *median filter*. Based on the principle of a moving window a median filter recalculates the median using the surrounding entries within the defined window. The filter eliminates outliers, but changes the statistics of the image as well. Different window sizes can be chosen, e.g. 3x3 or 5x5 pixels. As the window size becomes larger the resulted image looks slightly more blurred, although the resolution is maintained.

3.1.4 Polarisation of electromagnetic waves

Polarisation is the phenomenon of (electromagnetic) waves oscillating in more than one direction, but always perpendicular to the direction of the wave. Transmitted and received waves can be either horizontally or vertically polarised and denoted by respectively an 'H' or 'V'. As the name suggests, the electric field of horizontally polarised waves is horizontal with respect to the slant range direction, while for vertically polarised it is perpendicular to the slant range direction. Recent remote sensing radars are also capable of alternating emitting and receiving both horizontally and vertically polarised waves. For *co-polarisation* the transmitted and received polarisation are identical and fixed, while different polarisation for both ways results in *cross-polarisation*. The polarisation of a radar system is indicated by two indices; e.g. 'HH' or 'VV' for co-polarisation and 'HV' or 'VH' for cross-polarisation. The first and second indices specify respectively the transmitted and received polarisation. Radar systems can be either

single ('HH' or 'VV'), dual ('HH'+'HV' or 'VV'+'VH') or quad ('HH'+'HV'+'VH'+'V') polarised. Co-polarisation gives more information in the line of direction of the beam, while cross-polarisation is more sensitive to surfaces with multiple scatterers, such as buildings. By combining data from the cross- and co-polarised channels more information can be obtained useful for research.

3.1.5 Real and Synthetic Aperture Radar

Radar systems are not able to emit and receive signals at the same time as they are working with a single antenna. Emitting and receiving is alternated by sending out pulses. These pulses are transmitted with a frequency called the *Pulse Repetition Frequency (PRF)*. An increased azimuth resolution can be achieved by increasing the PRF. The distance the signal travels within its *pulse length* or pulse duration equals the minimum distance two objects should have to be distinguished. The pulse length is determined as follows, with c the speed of light in $ms^{-1}$and B the signal bandwidth in Hz.

$$\Delta_r = \frac{c\tau}{2} = \frac{c}{2B} \tag{3.4}$$

For a RAR system with a pulse length of 5$\sim$100μs, according to Equation 3.4 the minimum separation distance is between 750m and 15km. This poor slant range resolution can be improved by introducing a *chirp*. Applying a chirp compression an increased frequency with time over the pulse length is created. The pulse length now becomes inversely proportional to the bandwidth of the chirp - see Equation 3.4. In case of Sentinel-1 the maximum chirp bandwidth is 100MHz, improving the slant range resolution to 1.5m.

To determine the ground resolution in azimuth direction, the wavelength of the pulse is needed. Usually, radar systems use the following three wavelengths with corresponding *bandwidths*: X-band (8-12GHz | 2.5-4cm), C-band (4-8GHz | 4-8cm) and L-band (1-2GHz | 15-30cm). Taking the ratio of the wavelength over the antenna length, the radar antenna beam width of the pulse can be determined as follows.

$$\beta_a = \frac{\lambda}{L} \tag{3.5}$$

In case of Sentinel-1 using C-band and an antenna length of 12.3m, according to Equation 3.5 a beam width of 0.003rad is obtained. With an altitude of 693km, the ground resolution becomes 2km. Improving the resolution could be done by increasing the antenna length, which is very impractical on a satellite. The limitation of the size of the antenna can be bypassed by creating a synthetic larger antenna. By emitting pulses from a moving sensor an effectively larger antenna is created, leading to an increased azimuth resolution and thus *spatial resolution*s up to even 1m (TerraSAR-X) can be reached. This technique is called SAR and shown in Figure 3.3. The echoes of the pulses transmitted are coherently integrated using SAR signal processing techniques. Consequently, the ground resolution equals the ratio of the physical antenna length over the 2 - see Equation 3.6.

$$\Delta_a = \frac{L}{2} \tag{3.6}$$

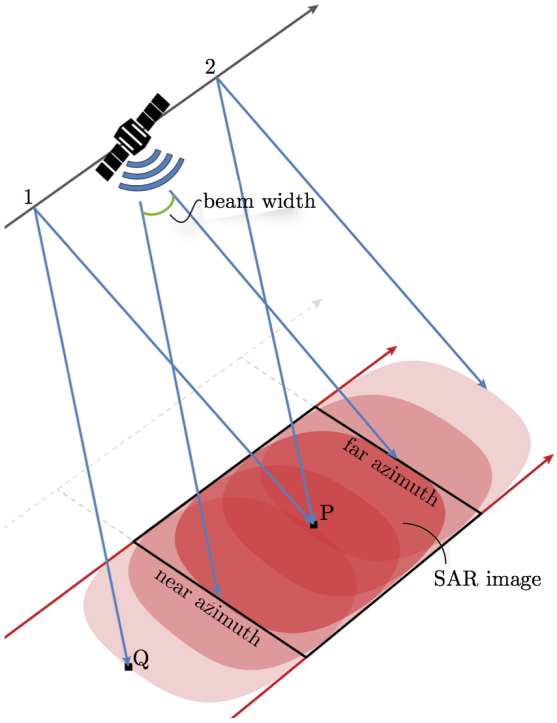

Figure 3.3: Schematic overview of imaging geometry by SAR principle. The echoes from the first until the last pulse that hit point P are recorded to create an artificially long antenna.

The ground resolution of the Sentinel-1 products improves to almost $6m$ when using SAR. SAR is an useful remote sensing technique improving the spatial resolution by some orders of magnitude.

3.2 Processing of Synthetic Aperture Radar data

Image processing involves different steps and starts with the raw data acquired by the receiving station. The product is called Level-0 or L0. The unfocused L0 products can be processed to generate various types of products useful for end users, such as L1B products. There are two types of L1B products; Single Look Complex (SLC) and Ground Range Detected (GRD). The SLC products are single-looked with phase and amplitude information and focused in slant-range geometry. The GRD products, on the other hand, is multi-looked (range x azimuth: 6x2) to reduce speckle noise, but at the expense of spatial resolution. The data is focused to ground range using an Earth ellipsoid model and maintaining the original satellite path direction.

GSAR is an automatic processing chain developed by Northern Research Institute (NORUT) and uses Level-1B GRD products to create geocoded SAR images cartographic projection UTM zone 33N, WGS-84, which is typical in Norway and Svalbard. Geocoding is needed to relate the spatial coordinates of the image to the corresponding spatial coordinates on the earth's surface. Instead of relying on Ground Control Point (GCP)s, the program uses precise orbit information together with a DEM for processing. The output of GSAR contains a radar backscatter coefficient image, a layover and shadow mask file to eliminate geometric distortions and a file with all local incidence angles. These are all used as input for this research project.

3.3 Avalanche detection using Synthetic Aperture Radar

Rott (1984) found that the ideal frequencies for monitoring snow with active microwave sensors are X- and C-band. This is due to the difference in backscatter signal between wet snow and the snow-free ground at these frequencies. The first avalanche detection using SAR images was conducted by Wiesmann et al. (2001). They designed a change detection algorithm and applied it on ERS1/2 data resulting in a visualisation of the avalanche debris fields. This method is based on the backscatter theory that will be explained in this section.

3.3.1 Radar backscatter theory

The backscatter signal received by the antenna of a satellite contains information about the scattering surface. Using varying frequencies different information can be obtained and used to determine dry or wet snow areas. The breakdown of the contribution to the backscatter signal is different for dry and wet snow, as illustrated in Figure 3.4. As shown by Magagi and Bernier (2003) the total scattering from the snow σ^T can be written as seen in equation 3.7.

$$\sigma^T = \sigma^g + \sigma^v + \sigma^{as} + \sigma^{gv} \tag{3.7}$$

The secondary volume scattering after reflection from the ground, the volume scattering within the snowpack, the scattering from the air-snow interface and the interaction term between volume inhomogeneities and lower boundary, i.e. the ground, are denoted as σ^g, σ^v, σ^{as} and σ^{gv}, respectively. Dry snow allows the radar signal to penetrate the snow up to $20m$ for C-band radar. Thus the largest contribution in dry snow stems from the ground surface, but the relative importance of σ^g/σ^v increases with frequency. By combining Ku- and X-band separation of the various volume- and surface-scattering components is possible as they are sensitive to volume scattering (ESA, 2012). In wet snow conditions the main backscatter contribution stems from the snow surface as electromagnetic waves are absorbed effectively in the surface layer (Ulaby et al., 1986).

The increased surface roughness and snow mass of avalanche debris cause a higher backscatter coefficient making it possible to discriminate avalanches from surrounding homogeneous snow cover. Figure 3.5 shows two RADARSAT-2 Ultra Fine (UF) images of a part of Nordenskiöld Land. The left image was acquired on 2013.06.10 shortly after avalanche activity. The bright tongue-shaped features are most likely avalanches. The image on the right shows the same area acquired on 2013.09.14; three months later at the end of the summer when avalanche activity is low and the avalanche debris of June has melted away. The bright areas from *'20130610'* are not visible in the reference image *'2030914'*. The high contrast between the low radar backscatter from unperturbed snow and the high backscatter from the avalanche debris fields makes it possible to visually identify avalanches in high resolution RADARSAT-2 C-band SAR imagery (Malnes et al., 2013).

3.3.2 Visualisation of Synthetic Aperture Radar images in RGB

Creating RGB images by combining two SAR images obtained using the same mode and track but with differing acquisition dates, possible avalanches show up clearer. RGB images

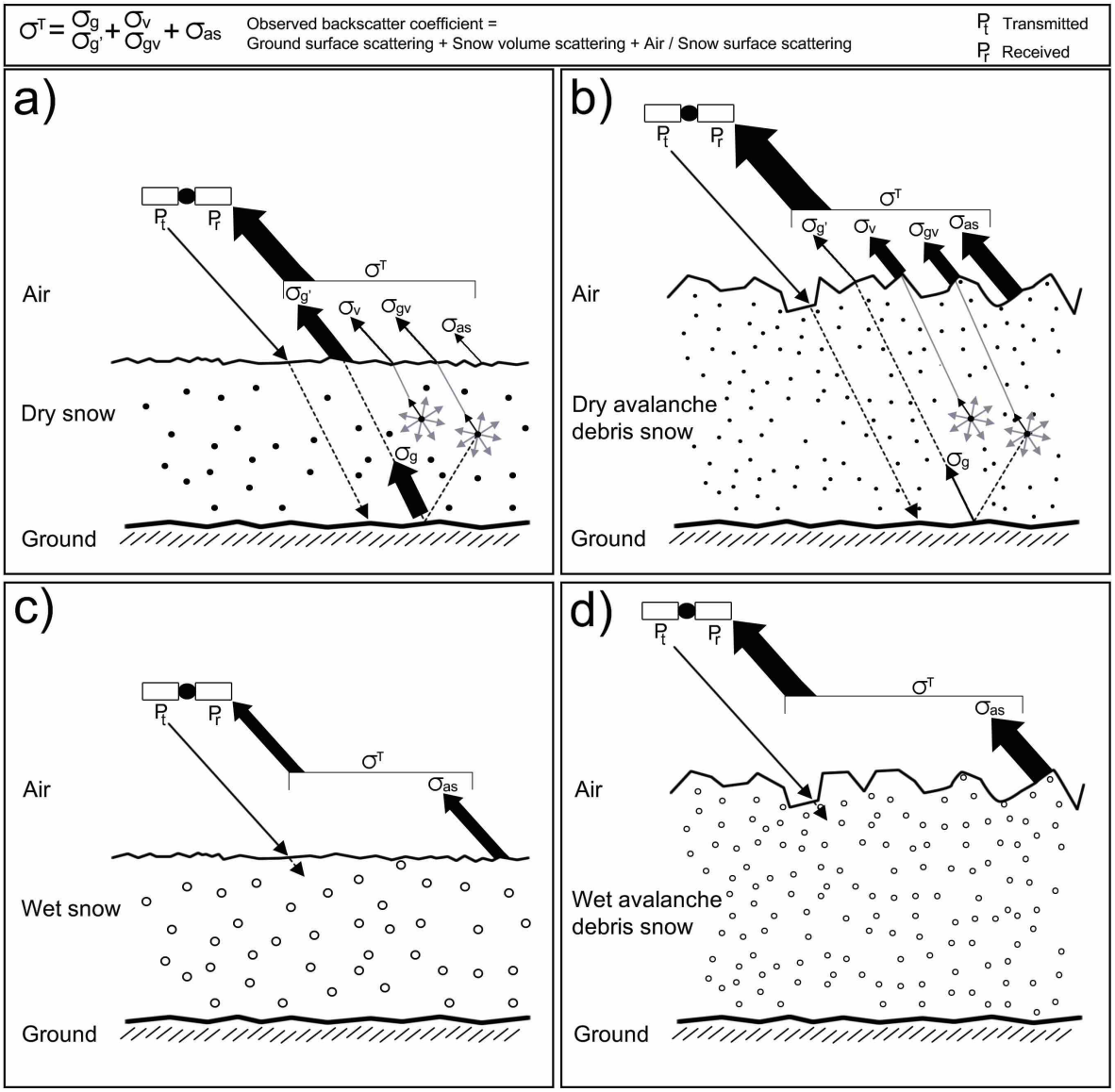

Figure 3.4: Illustration of backscatter theory for **a)** dry snow, **b)** dry avalanche debris snow, **c)** wet snow and **d)** wet avalanche debris snow (Eckerstorfer and Malnes, 2015).

are build up from three channels; red, green and blue. The image taken after the occurrence of an avalanche is placed in the green channel, whilst for the red and blue channel a reference image is used. The reference images are preferably taken in a snow-free or dry snow period to increase the contrast and thus the visibility of the avalanches in the green channel (Wiesmann et al., 2001). Either the same reference image can be taken for the red and blue channel or two different reference images.

Visualised in Figure 3.6 is the construction of such a RGB image from the same two images as used for Figure 3.5 covering Nordenskiöld Land, Svalbard. The image is constructed by *[RGB]= [20130914, 20130610, 20130914]*. Avalanche debris fields show up as bright green

(a) '20130610' **(b)** '20130914'

Figure 3.5: RADARSAT-2 UF mode images covering a part of Nordenskiöld Land on Svalbard. The avalanche image from 2013.06.10 shows debris fields as bright areas, while the reference image taken on 2013.09.14 does not show any avalanche activity. The two images can be used to create a RGB image for manual detection or a difference image for automatic detection.

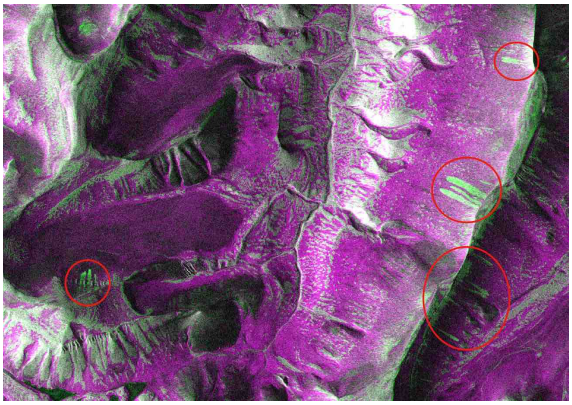

Figure 3.6: RGB image constructed from two RADARSAT-2 UF mode images covering a part of Nordenskiöld Land on Svalbard. The RGB image is constructed using an avalanche and a reference image acquired on 2013.06.10 and 2013.09.14, respectively: *[RGB]=[20130914, 20130610, 20130914]*. Avalanche debris fields appear as bright green tongue-shaped features and are encircled in red.

tongue-shape features, and yields better visible detection of the avalanches as compared to Figure 3.5a. The extended pink areas stem from wet snow in the avalanche image, while green areas are due to wet snow in the reference image.

For high resolution images a sharp contrast between the avalanche debris field and the surroundings exists, improving manual detection significantly. Manual detection of avalanches in RGB images can be done in a Geographical Information System (GIS) environment by simply delineating the green tongue-shaped features. This has been proven to be a successful method by Eckerstorfer et al. (2014b).

3.3.3 Change detection by thresholding

The algorithm of change detection is inspired on a similar algorithm for wet snow detection used by (Nagler and Rott, 2000). The low backscatter signal reflected by the melting snow is compared to a reference image obtained during dry snow or snow-free conditions. To separate wet snow from other surfaces a threshold of -3dB was found for both RADARSAT and ERS data. All test sites which were studied are located in Austria. To reduce the loss

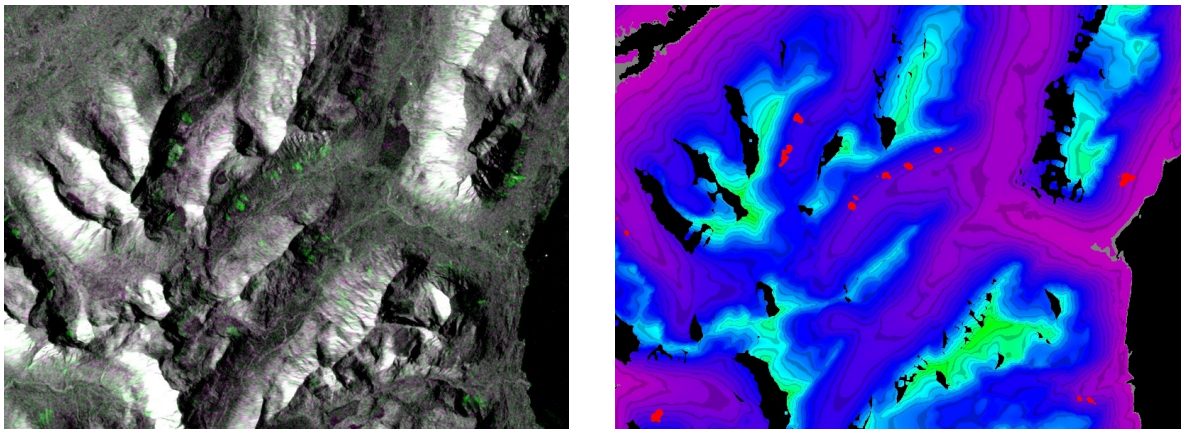

(a) RGB image **(b)** Classified image

Figure 3.7: Classification algorithm applied on Sentinel-1A IW images of Sennedalen nearby Tromsø in Norway. The RGB image is constructed from *'20150106'* and reference image *'20141213'*. The green tongue-shaped features are consistent with avalanche debris fields. The height map shows avalanche debris class in red and layover mask in black. *© Hannah Vickers, NORUT.*

of information due to layover, foreshortening and radar shadow images from ascending and descending passes can be combined. The thresholding is applied on the ratio of two geocoded SAR images acquired in the same mode but on different dates. One of the images shows avalanche activity, while the other image is taken in the winter with dry snow or during the snow-free summer. The result is a map showing the wet snow extent. Malnes et al. (2013) applied a similar algorithm on SAR images covering northern Norway to detect avalanches. Single SAR images were used and the contrast in backscatter inside the avalanche and the surrounding area analysed. For all three test areas backscatter differences in the order of $2dB$ were found.

3.3.4 Classification of SAR images

Categorising all pixels in an image in certain (i.e. predefined) classes or themes is called classification. Image classification can be divided into unsupervised and supervised classifiers (Duda et al., 2000). For the former one no training data is available and thus it is purely based on the statistical distribution of the input data. The later one make use of manual training of the data set to define the classes. The classification of avalanche debris is performed on the difference in backscatter between an image with visible avalanches and a reference image obtained during dry snow or snow-free conditions. To detect the avalanche debris fields κ-means clustering can be used, where each pixel is classified to the cluster with the nearest mean. The κ clusters or classes are defined beforehand and can be varied, e.g. two classes: avalanche & non-avalanche. This classification method cause the data to be divided into Voronoi cells (Duda et al., 2000). Figure 3.7 shows a Sentinel-1A Interferometric Wide swath (IW) mode RGB image and the classified version. The RGB is created by two images; one image obtained on 2015.01.06 and the reference image on 2014.12.13. The red areas are the classified avalanche debris fields and are consistent with the green tongue-shaped features shown in the left image.

Chapter 4

Methods for automatic detection of avalanches

An overview of the workflow for the avalanche detection in Synthetic Aperture Radar (SAR) images as used in this project is shown in Figure 4.1. This chapter explains all the steps visible in this figure. The first section elaborates on how to detect avalanche debris fields manually. As the desire to perform manual detection diminishes due to its labour intensity, an automatic detection method is designed. The design of the automatic detection is based on a quantitative analysis of the manual detection. The second and third section go into detail on respectively the quantitative analysis of the manual detection method and the set-up of the automatic detection. The last section discusses the assessment of the automatic detection.

4.1 Manual detection using RGB images

As explained in Subsection 3.3.2 RGB images are created to increase the visibility of the avalanche debris fields which is convenient for manual detection. These RGB image are build up from two (or three) different geocoded SAR images; an avalanche image acquired after the avalanche events in the green channel and one or two reference images acquired during dry snow or snow-free conditions in the red and blue channel. For this project the same reference image is used for both the red and blue channel. The manual detection is then performed by drawing vectors over the RGB image showing the avalanches as green tongue-shaped features. These vectors are drawn using the *Region Of Interest (ROI) Tool* in ENVI and exported as a shape file, which is a standard format for geographical vectors. ENVI is an image analysis software combining advanced image processing and geospatial analysis technology. From the shape file a mask is created to either clip out or mask out the avalanches to determine the difference in backscatter coefficients, the slope angle and local incidence angle at the location of the debris field. This is explained in the next section. The output of the manual detection is the RGB image with in yellow overlaid the detected debris fields.

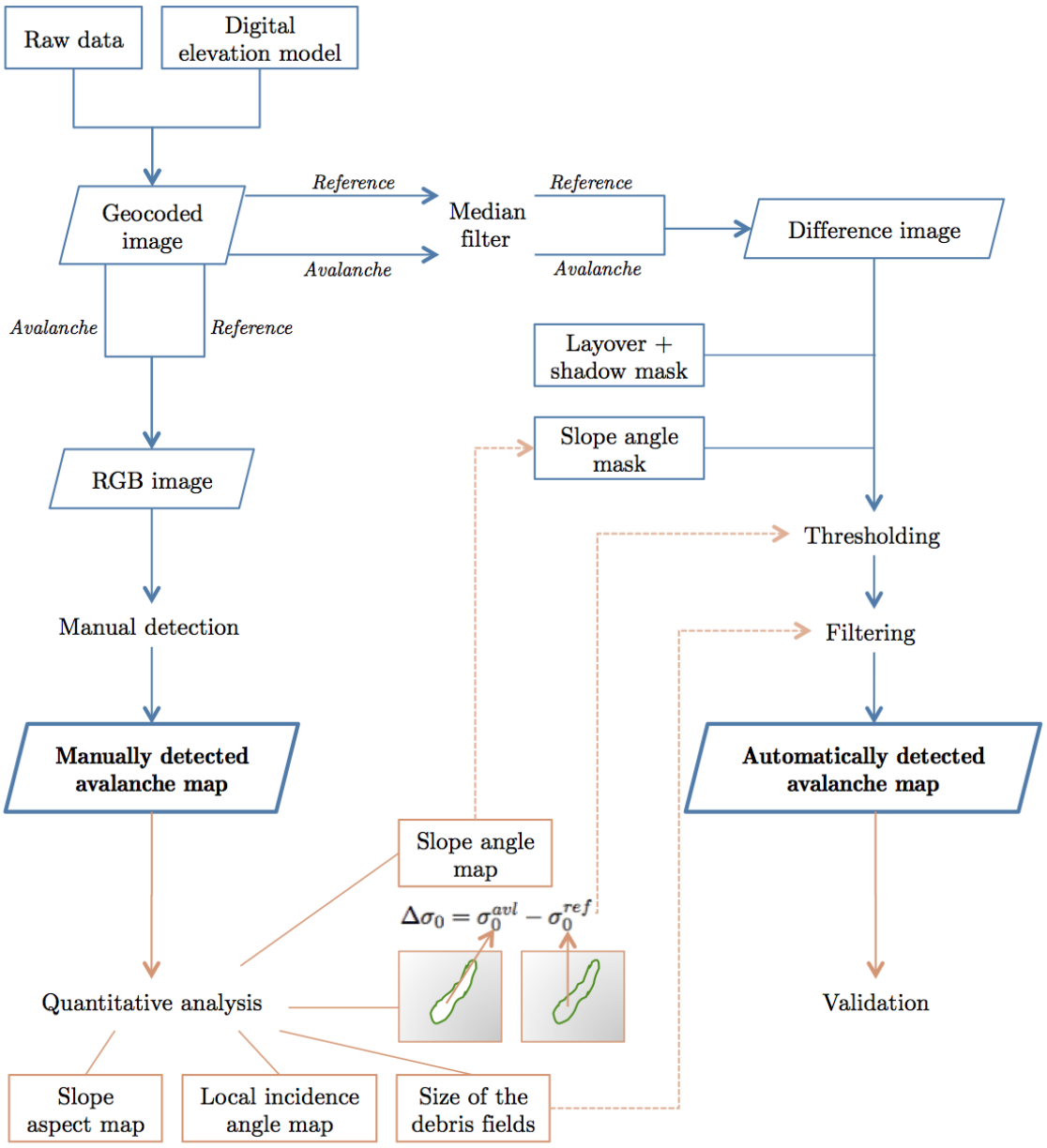

Figure 4.1: Workflow showing avalanche detection process of SAR images as designed in this research project.

4.2 Quantitative analysis of the manually detected avalanches

The analysis of the manually detected avalanches forms the boundary and input of the automatic detection method. From the available Digital Elevation Model (DEM) both a slope angle and a slope aspect map is created showing respectively the angle and aspect of all the slopes within Nordenskiöld Land. The slope angle map is used to determine the angles at which debris fields are found and to create a mask eliminating areas not prone to avalanches. The slope aspect denotes the direction the slope is facing, e.g. north, northeast, etc, and is

made to analyse the influence of the track (descending/ascending) on the detectability of the avalanches. Provided with the geocoded SAR image is a file containing all local incidence angles. Both the slope angle and aspect have an influence on the local incidence angle and this is analysed as well.

From the shape file created during manual detection a mask is made to either clip out or mask out the debris fields and to determine the backscatter coefficient within and outside of the avalanches. The difference in backscatter between the debris fields in the avalanche image σ_0^{avl} and the same area in the reference image σ_0^{ref} is calculated by Equation 4.1. This formula is applied to both the difference in backscatter within the detected avalanches as well as outside of the avalanches. Using $\Delta\sigma_0$ histograms are then made to get an overview of the distribution of backscatter coefficients. From these histograms a range of threshold values is selected as input for the thresholding in the automatic detection method.

$$\Delta\sigma_0 = \sigma_0^{avl} - \sigma_0^{ref} \tag{4.1}$$

Finally, the size of the manually detected debris fields is determined using the *Measurement Tool* in ENVI. The range of sizes determines the size of the filter applied after the thresholding, which is explained hereafter.

4.3 Automatic detection by thresholding and filtering

The automatic detection is based on the change detection by thresholding technique as discussed in Subsection 3.3.3. The script to automatically detect the avalanches works according to the following steps:

Step -1: Download data from satellite provider
Step 0: Generate the input
Create geocoded SAR images, a local incidence angle file and a layover & shadow mask file using GSAR. More on the SAR processing is given in Section 3.2.
Step 1: Apply a median filter
Reduce speckle by applying a median filter with a window size of 5x5 pixels on both the avalanche image and reference image separately. See paragraph below for an explanation of the median filter.
Step 2: Create a difference image
Subtract the reference image from the avalanche image showing the debris fields to create a difference image. This is done to analyse the backscatter increase of the debris fields.
Step 3: Create a slope angle mask
Use the DEM to create a slope angle file. According to McClung and Schaerer (2011) slab avalanches are triggered on slope angles between 25^o and 55^o. However, avalanches can slide down further and normally stop at lower slope angles. Therefore a mask is created eliminating areas not prone to avalanches, so $< 5^o$ and $> 55^o$.
Step 4: Apply the slope angle and layover & shadow mask
Eliminate areas where avalanche debris is not expected using the slope angle mask and mask out the areas affect by geometric distortions, such as layover and shadow.
Step 5: Apply thresholding
Use the outcome of the quantitative analysis to determine a range of threshold values to

optimise the automatic detection. The output of the thresholding is a binary image showing the pixel below and above the threshold value.

Step 6: Apply filtering

Apply a filter after the thresholding to get rid of noise. Two post-classification filters are defined; a median filter and a Remove Small Objects (RSO) filter. For the principle of the median filter and the RSO filter see the paragraphs below.

Step 7: Generate an output

Create an avalanche map showing the avalanche image with on top outlined the pixels which have been detected as avalanches automatically. For the high resolution images also maps are created showing which pixels are identified as avalanches manually and which are classified as avalanches automatically as well as their overlap.

Median filter

The median filter works by calculating for every pixel the median of the neighbouring pixels within the predefined window. Using this filter outliers are eliminated and therefore it is useful for speckle reduction. However, a downside is that the statistics of the image are changed. And although the resulted image looks slightly more blurred, the resolution is maintained. See also Subsection 3.1.3.

Remove Small Objects (RSO) filter

The RSO filter is based on eliminating areas which are smaller or larger than the size of the debris fields as derived from a quantitative analysis. The filter is applied on the binary image obtained after thresholding and is based on the 'bwconncomp' function in Matlab that uses a flood-fill algorithm to calculate the connecting areas with same pixel value. The flood-fill algorithm works as follows; it finds a complete area of connected pixels (of the same value) by testing for every pixel the 8-neighbouring pixels, which is the connectivity. For two-dimensional matrices the connectivity or condition of being connected can also be set to 4-neighbouring pixels which does not test diagonal neighbouring pixels. The algorithm repeats the steps for every pixel within the input matrix. The output of the algorithm is the number of connected components and an array containing for every group of connected components the linear indices of the pixels in that group. Using the output of the 'bwconncomp' function the filter then eliminates all connected groups smaller or larger than the boundary. This boundary is based on the size of debris fields, where also the pixel spacing of the image is taken into account.

4.4 Assessment of the automatically detected avalanches

The automatic detection methods are assessed by comparing the results to the performed manual detection. An avalanche map is created by overlaying the pixels assigned to the avalanche class by the automatic detection on top of the avalanche image. One of the most important information gaps in avalanche research is mapping the location and extent of avalanches (Buhler et al., 2014). Such an avalanche map fulfils to the wish of monitoring the location of avalanche activity. To optimise the automatic detection the avalanche map is compared to the result of the manual detection. The debris fields also manually detected are

encircled. All other automatically detected pixels are thus false alarms; pixels falsely labelled to the avalanche class. The optimum threshold value and post-classification is a trade-off between the correctly identified debris fields and the false alarms.

The probability of detection or True Positive Rate (TPR) is a measure to state the actual positives which are correctly identified as such. To determine the TPR, first the True Positive (TP), True Negative (TN), False Positive (FP) and False Negative (FN) need to be calculated - see Equation 4.2. The TP and TN represent the amount of pixels correctly identified as avalanche or as non-avalanche class, respectively. The FN are the pixels satisfying the condition (in this case manually detected avalanches) but fail to be allocated into this class. The FP are the pixels falsely labelled to the avalanche class or false alarms.

$$TPR = \frac{TP}{TP + FN} \tag{4.2}$$

To investigate the detectability of the extent of the debris fields maps are created showing the TP, TN, FP and FN. Especially for the high resolution images it is clear how much of the tongue-shape is captured by the manual and automatic detection.

Chapter 5

Data overview

The area around Longyearbyen on Svalbard is frequently covered by the RADARSAT-2 and Sentinel-1A satellites, both having a Synthetic Aperture Radar (SAR) system. The RADARSAT-2 satellite has been operational since 2007, while Sentinel-1A was launched in April 2014. Each satellite has different advantages due to the varying specifications. The following sections present some mission facts together with a description of the dataset available for this research project. Besides the SAR images obtained by the RADARSAT-2 and Sentinel-1A satellites, other data such as meteorological data, optical images and field observations are used to get a complete overview of the avalanche activity and to validate the detected avalanches. This is needed to optimise the detection method and to be sure that as much avalanche activity as possible is captured.

5.1 Synthetic Aperture Radar data

Multiple satellites exist which are able to obtain SAR data. These satellites are operated by different agencies. Among them is Sentinel-1 which is a constellation of two satellites, i.e. Sentinel-1A & Sentinel-1B. Sentinel-1A has been launched in April 2014, while Sentinel-1B is planned for 2016. An advantage of Sentinel-1A is the short repeat cycle of 12 days, which decreases to 6 days when using both Sentinel-1A and -1B. Another advantage is that the SAR data is free of charge and largely available. Although RADARSAT-2 has a large repeat cycle of 24 days, the Ultra Fine (UF) mode has a better resolution than Sentinel-1A. Therefore both RADARSAT-2 and Sentinel-1A data is used for this project. The mission facts from the two satellites is obtained from Canadian Space Agency (2011) and ESA Earth Online (2014) and shown in Table 5.1.

Both satellites cover the area of Nordenskiöld Land on Svalbard in different beam modes with varying characteristics. The RADARSAT-2 modes used during this project are UF, ScanSAR Narrow (SCNA) and ScanSAR Wide (SCWA), all obtained in 'VV'-polarisation. The ScanSAR modes are characterised by using electronic beam steering. The swath width is increased by using bursts of pulses with adapted Pulse Repetition Frequency (PRF) at

Table 5.1: Mission facts of RADARSAT-2 and Sentinel-1 obtained from Canadian Space Agency (2011) and ESA Earth Online (2014), respectively. Note that Sentinel-1B is scheduled to be launched in 2016, which increases the repeat cycle to only 6 days.

	RADARSAT-2	Sentinel-1A(/1B)
Operator	Canadian Space Agency	European Space Agency
Launch date	14 December 2007	3 April 2014(/2016)
Orbit	Sun-synchronous	Sun-synchronous, near-polar, circular
Altitude	$798km$	$693km$
Inclination	98.6^o	98.18^o
Repeat cycle	24 days	12 days (/6 days)
Imaging frequency	C-band at $5.405GHz$	C-band at $5.405GHz$

Table 5.2: Available RADARSAT-2 images in UF, SCNA and SCWA mode and Sentinel-1A images in EW mode covering Nordenskiöld Land on Svalbard. The pixel spacing is given in [ground range x azimuth]. The SCNA and SCWA mode images are obtained in 'HV'-polarisation, UF mode images in 'VV'-polarisation and EW mode images in both 'HH'- and 'HV'-polarisation.

	Beam mode	Pixel spacing [m]	Asc/desc _track	1st pass	2nd pass
RADARSAT-2 2013					
	UF	3x3	asc_187	10 June	14 September
	SCNA	50x50	asc_158	8 June	12 September
	SCWA	100x100	des_152	8 June	12 September
Sentinel-1A 2015					
	EW	40x40	des_052	2 March	14 March
	EW	40x40	asc_058	2 March	14 March
	EW	40x40	des_081	4 March	16 March
	EW	40x40	asc_087	4 March	16 March
	EW	40x40	des_096	5 March	17 March
	EW	40x40	asc_101	5 March	17 March
	EW	40x40	des_110	6 March	18 March
	EW	40x40	asc_116	6 March	18 March

the expense of resolution. The ScanSAR modes operate in both single and dual polarisation. The images in 'HV'-polarisation are available for this project. SCNA covers a swath width of about $300km$ with a pixel spacing of 25x25m [ground range x azimuth]. Covering a larger swath with of $450 \sim 500km$, SCWA has a pixel spacing of 50x50m. The highest resolution of the three beam modes is obtained UF mode having a pixel spacing of 3x3m. It operates only in single polarisation and has a swath width of $20km$ (Canadian Space Agency, 2011).

The Sentinel-1A data has a lower resolution than RADARSAT-2 in UF mode, but has a more beneficial repeat cycle - see Table 5.1. Sentinel-1A obtains in general at least two acquisitions (ascending and descending) every 12 days in both co- and cross-polarisation ('HH' and 'HV'). On Svalbard Sentinel-1A acquires on average two images each day; a descending and an ascending image. Although Interferometric Wide swath (IW) mode has a better spatial

resolution, Extra Wide swath (EW) mode provides a larger swath coverage of 400km and a pixel spacing of 40x40m. As sea-ice monitoring is the primary objective for Sentinel in the Arctic, broad coverage is desired and thus the data is only provided in EW mode. An overview of the SAR images available for this project is presented in Table 5.2. All images are geocoded to the cartographic projection; UTM zone 33N, WGS-84.

5.2 Digital Elevation Model

The topographic surface of the earth is characterised by the terrain morphology, e.g. elevation, slope, aspect, curvature and roughness. A Digital Elevation Model (DEM) is a three-dimensional representation of the topographic surface. A slope mask is created using the DEM and can be used to eliminate areas where avalanches do not occur according to McClung and Schaerer (2011) - see Section 2.1. The DEM used for this research project is provided by the Norwegian Polar Institute in Tromsø, Norway and has a horizontal resolution of 20m. Figure 5.1 shows the DEM covering Nordenskiöld Land, Svalbard. The yellow lines indicate the contour lines with an interval of 200m. In case of the UF mode image the DEM is resized to match the resolution of the SAR image having a pixel spacing of 3m.

5.3 Meteorological data

The meteorological conditions around the acquisition dates of the SAR images are analysed to investigate the influence on the avalanche detection. This is done by examining the wet snow cover maps from Snow, Ice and Avalanche Applications (SNAPS), provided by Northern Research Institute (NORUT), and the weather data obtained from the Norwegian Meteorological Institute and University Centre in Svalbard (UNIS). The SNAPS is a project focusing on snow and avalanche services within the Northern Periphery of Europe in Iceland, Norway, Sweden and Finland and provided (almost) daily snow maps indicating amongst others wet snow areas. The weather data from the Norwegian Meteorological Institute exists of air temperature, wind speed and wind direction and is provided as hourly averages. Wind speed, wind direction and air temperature can also be obtained from the web portal eKlima.no created by the Norwegian Meteorological Institute. The web portal provides free access to a climate database with historical daily averaged data and real time observations.

5.4 Available datasets for validation

Validation of the detected debris fields is done in multiple ways, e.g. by optical images and field observations. For this project as much validation data as possible is collected. However, as research on snow avalanche detection in SAR images is relatively young and little field data is available validation is challenging.

5.4.1 Multispectral optical images

Multispectral optical images of the entire earth are obtained by the Landsat-8 instruments and can potentially be used for validation of the detected avalanches in the SAR images. The

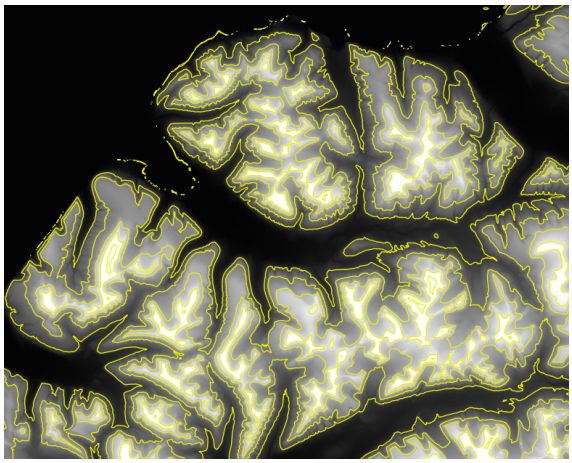

Figure 5.1: Top view of Digital Elevation Model (DEM) provided by Norwegian Polar Institute covering Nordenskiöld Land on Svalbard. The yellow lines indicate contour lines with an interval of 200m.

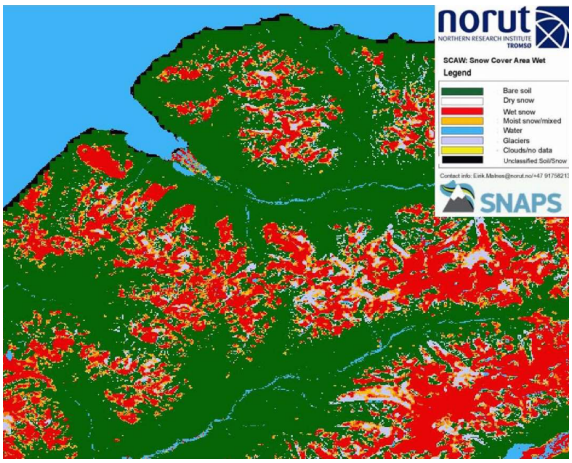

Figure 5.2: Wet snow map covering Nordenskiöld Land on Svalbard, provided by SNAPS. Data is obtained on June 8, 2014.

Landsat program is operated by National Aeronautics and Space Administration (NASA) and USGS and has included 8 satellites so far, of which only Landsat 7 and 8 are still in use. Landsat-8 was launched on February 11^{th} of 2013 and is planned to have a 5-year mission life (NASA, 2015). It carries two instruments; the Operational Land Imager (OLI) and the Thermal Infrared Sensor (TIRS) and measures at eleven different frequency ranges of the spectrum which are called bands. The spatial resolution of the images varies between 15m, 30m and 100m for respectively panchromatic, Visible (Vis)-Near Infrared (NIR)-Shortwave Infrared (SWIR) and Thermal Infrared (TIR). Only the shortest wavelengths, less than 0.680μm, sense visible light. The acquired images are made available online at *earthexplorer.usgs.gov*. To create a 'Natural Color' image the website uses the bands 6 (Vis: 1.57-1.65μm), 5 (NIR: 0.85-0.88μm) and 4 (SWIR: 0.64-0.67μm). The 'Thermal' images are one-band grey scale images created from band 10 (TIR: 10.60-11.19μm).

5.4.2 Field observations

The detected avalanches can also be validated using field observations. Field observations, such as photographs of avalanche events, snow profiles and stability test results can be published online at *regObs.no*. This website is a crowd-sourcing website to collect as much data as possible on the snow pack properties and the avalanche activity. To create the snow profiles websites such as *avanet.avatech.no* can be used. This website not only has a tool to create the profiles but also stores and publishes them. By using these crowd-sourcing website the density of the network is increased. The former website is designed for Norway and Svalbard, whereas the later website covers the whole world.

Snow profiles obtained in Svalbard - February 2015

A snowpack is characterised by multiple layers caused by different precipitation events and/or snowdrift. By digging snow pits these layers can be exposed and analysed by identifying the

Figure 5.3: Map of Nordenskiöld Land on Svalbard, obtained from toposvalbard.npolar.no (Norwegian Polar Institute, 2015). Red circles indicated locations where snow profiles from Figures 5.4 and 5.5 are obtained, namely Vannledningsdalen and Sarkofagen.

properties of the various layers - see Figure 5.3. The analysis is done according to Greene et al. (2010, Chapter 3). The identification of grain type, grain size and water content is classified according to the International Commission on Snow and Ice (ICSI) standards (Colbeck et al., 1990) and is a rather subjective task. The Snow Water Equivalent (SWE) is a measure for the amount of water contained in the snowpack and can be found by multiplying the density of the snow by the snow depth. The snow profiles presented in Figures 5.4 and 5.5 were obtained on February 20^{th} and 27^{th}, 2015 around Longyearbyen, Svalbard, respectively. These are also published on *avanet.avatech.no*. The coordinates, aspect and slope angle of the site as well as the meteorological parameters, such as air temperature, cloud cover, precipitation and wind velocity are also recorded in the snow profile. The snow depth was determined by using a probe. The first snow pit was located on the northwest-facing flank of Sukkertoppen called Vannledningsdalen. The second was situated on the northwest-facing slope of Gruvefjellet called Sarkofagen. Both locations are indicated in Figure 5.3. More on these snow profiles can be found in Section 7.3 on validation of the Sentinel-1A images.

5.4.3 Manual detection by other avalanche experts

The manual detection is assessed by letting other avalanche experts analyse the RGB images as well. By encircling the areas they would identify as debris field without knowledge of the performed manual detection they can be used to validate the manual detection. Although it is not a fully qualified way of validation the manual detection can be verified and is less dependent on the operator.

AvaNet Snow Profile

Organization: AG-346

Location: Vannledningsdalen, Svalbard
Date: 2015-02-20 10:36 am
Snowpit depth: 151 cm
Lat/Lng: 78.2169790, 15.6540580
Observer: Turid Haugen
Snowpack depth: 151 cm

Elevation:	42 m	Wind:	Calm	Mean denisty for the snow pack is 389.25 kg/m^3. The SWE is 0.59 m.
Slope:	20°	Blowing snow:	None	
Aspect:	300° NWbW	Precipitation:	No Precipitation	
Air temp.:	-20.1°C	Foot Pen. (PF):	2 cm	
Sky:	◯ Clear	Ski Pen. (PS):	--	

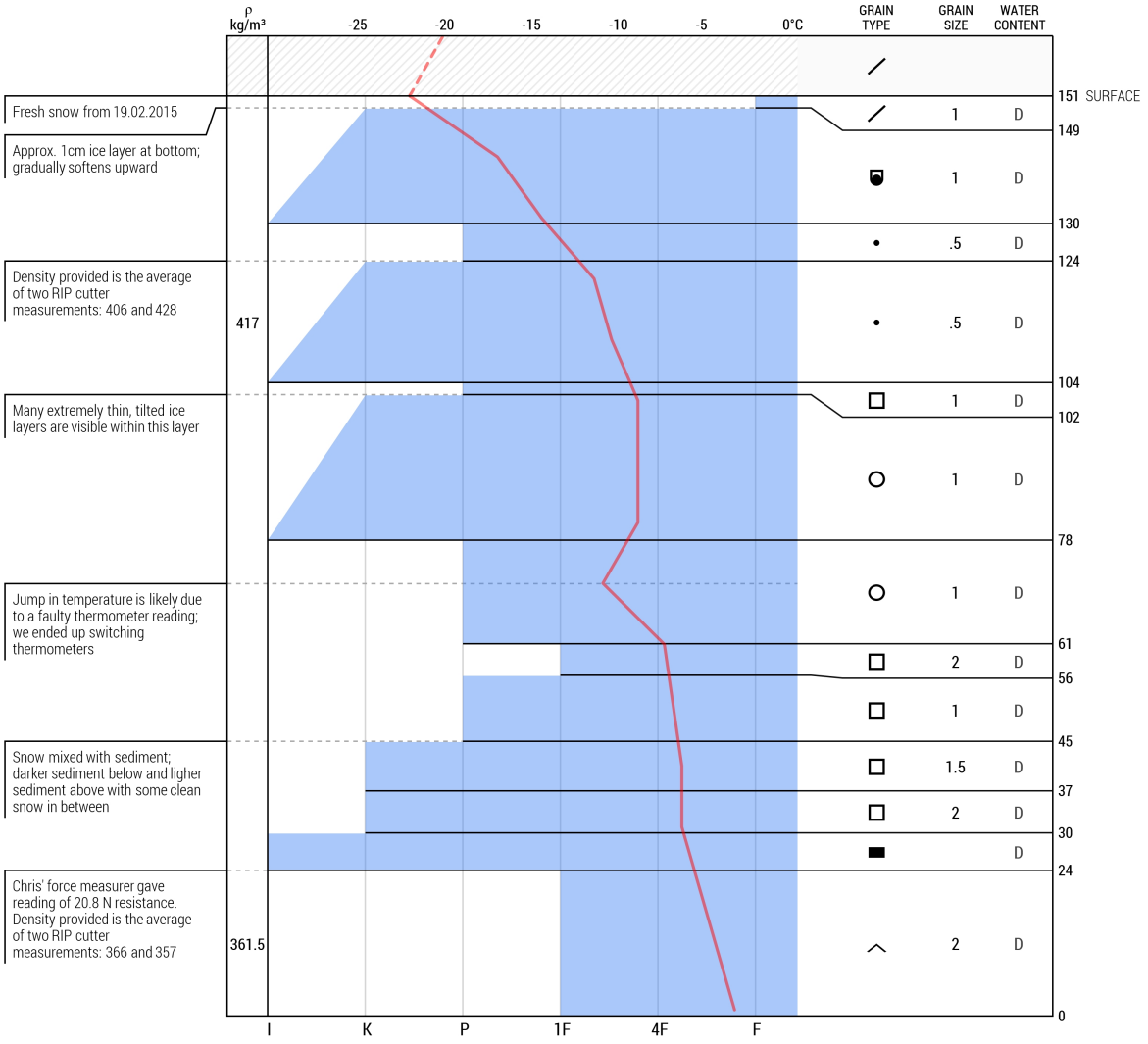

54E72C86A7C9900FACED9BEE

Powered by AVATECH

Figure 5.4: Snow profile #1 from February 20^{th}, 2015 at Vannledningsdalen on Svalbard, created using AvaNet. The red line indicates temperature within snowpack.

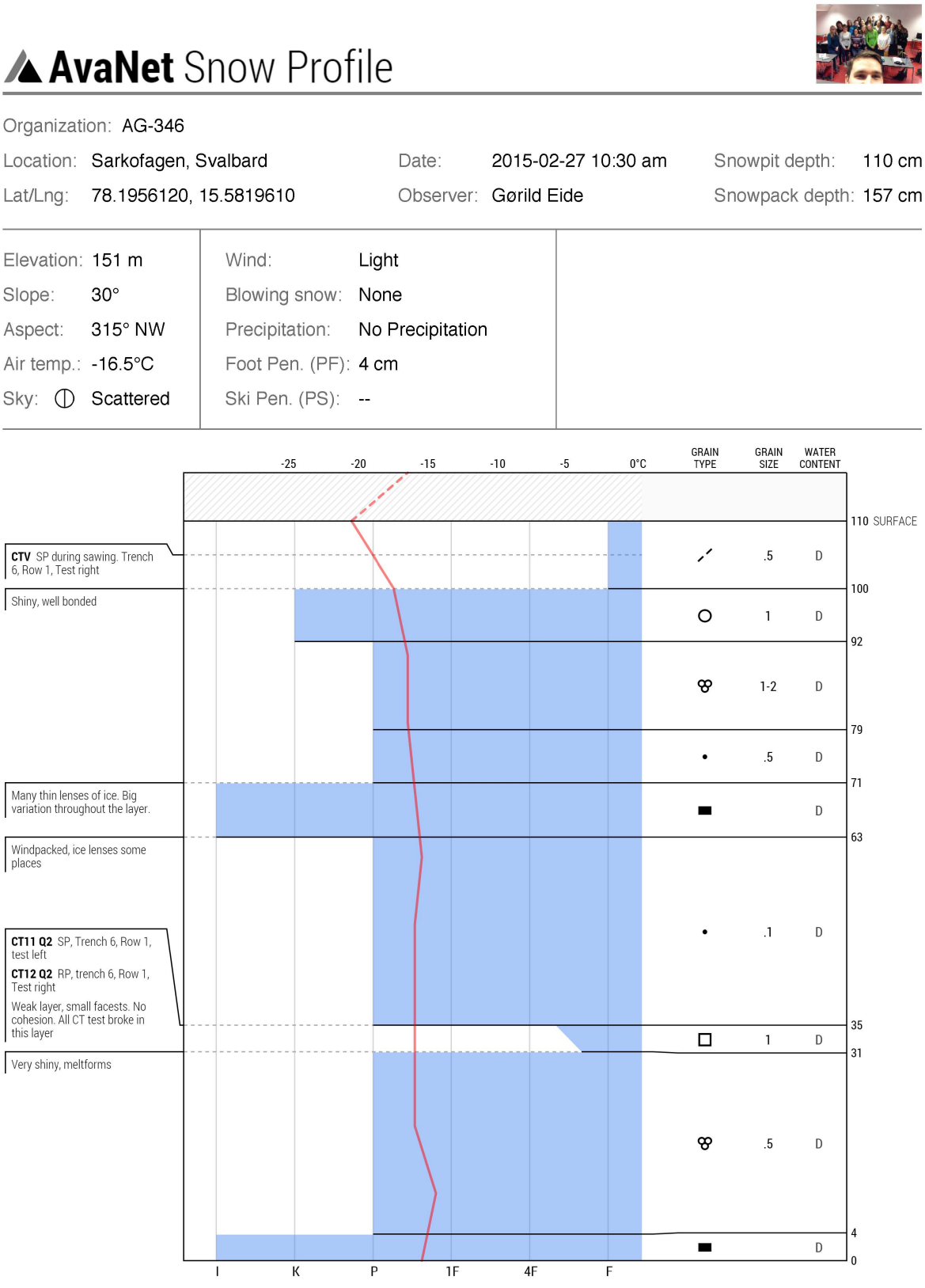

Figure 5.5: Snow profile #2 from February 27^{th}, 2015 at Sarkofagen on Svalbard, created using AvaNet. The red line indicates temperature within snowpack.

Chapter 6

Avalanches detected in fine RADARSAT-2 SAR images

This chapter presents the results and discussion of the designed framework applied to the RADARSAT-2 images. The Synthetic Aperture Radar (SAR) images are obtained by the satellite in different beam modes and as such have varying pixel spacings. The available RADARSAT-2 data was acquired in the spring and summer of 2013. Section 6.1 will go into detail on detecting and analysing debris fields in these images. As they have a pixel spacing of $3m$ it is expected that the manual detection can be done fairly easy. Due to this high resolution the automatic detection will probably distinguish tongue-shaped features characterising avalanches. First the outcome of the manual detection is given, followed by a quantitative analysis. This analysis is used as input for the automatic detection, which is assessed in Section 6.2 and validated in Section 6.3. Finally, the main findings are listed in Section 6.4.

6.1 Results of detection

The influence of using different pixel spacings for avalanche detection is analysed by comparing three RADARSAT-2 image pairs obtained in different beam modes. This is described in Subsection 6.1.1. The ScanSAR Narrow (SCNA) and ScanSAR Wide (SCWA) mode images are cropped to cover an area of 40x50km around Longyearbyen and are acquired in 'HV'-polarisation, while the Ultra Fine (UF) mode image covers an area of 20x20km and is 'VV'-polarised. They are acquired with a time difference of two days; the UF mode images on 2013.06.10 and 2013.09.14, and the other beam modes images on 2013.06.08 and 2013.09.12. As explained in Section 3.3.2 the avalanche debris fields can be made easier recognisable by creating RGB images contrary to using a single SAR image. The RGB images shown in Figure 6.1 are constructed by *[RGB]= [20130914, 20130610, 20130914]* and by *[RGB]= [20130912, 20130608, 20130912]*. Both the UF and SCNA images are ascending, while SCWA is descending, which might have an influence on detecting avalanches due to geometric distortions, i.e. foreshortening, layover and shadow - see Subsection 3.1.1.

After evaluation of the different beam modes, Subsection 6.1.2 describes the manual detection performed on the most suited beam mode for avalanche detection and a quantitative analysis on the manually detected avalanches. The outcome of this analysis will be the input for the design of the automatic detection method described in Subsection 6.1.3.

6.1.1 Evaluation of different beam modes

The available UF, SCNA and SCWA beam mode images are geocoded with a respectively pixel spacing of $3m$, $50m$ and $100m$ - see Table 5.2. The manual detection is performed on the RGB image in UF mode, as the avalanches are clearly recognisable in these high resolution images. The green tongue-shaped features as observed in Figure 6.1a are consistent with avalanche debris. To compare the different beam modes a shape file is constructed from the manual detection as explained in Section 4.1, which is then overlaid on top of the other RGB images in SCNA and SCWA mode. This is shown in Figure 6.2. The manual detected avalanches are outlined in yellow. For SCNA and SCWA an enhanced backscatter is observed (green areas), but the shape is no longer tongue-shaped due to the coarse image resolution.

Figure 6.3 shows the manually detected avalanches outlined in yellow and placed on top of the RGB image in UF mode. Table 6.1 presents the size of the manually detected avalanche debris fields in this RGB image. Two tongue-shaped features close to each other (on the same slope) are considered as one avalanche debris field. According to the destructive-size scale system presented in Table 2.1, these avalanches would be classified as $D2$-$D3$. This means that they range from being able to bury, injure or kill a person up to burying a car or destroying small buildings. As such they could pose a hazard to humans and infrastructure. The Ys and Ns in the table indicate whether the identified avalanches show an enhanced backscatter SCNA and SCWA mode images. Although for some avalanches an enhanced backscatter is observed, the coarse resolution makes the tongue-shape unrecognisable and the detection not as accurate. Therefore, the detection and analysis is performed using the UF mode image.

6.1.2 Manual detection and analysis

Analysing the RGB image as used for the manual detection and shown in Figure 6.3, the following can be noticed. Areas having a high backscatter in both images show up as white and denote little change between the acquisition dates. These areas are most likely rocks and gullies. Gullies are large ditches or small valleys created by running water and typically occur on hillsides. Noticeable in the RGB images as well are the very pink and green areas. These extended green areas are, however, not consistent with avalanche debris fields as they are not tongue-shaped; they occur in flat terrain not prone to avalanches and are in general much larger than typical avalanches. Wet snow is characterised by low backscatter and is consistent with pink colour if it occurs in the avalanche image and green if it occurs in the reference image. The pink and green areas are thus due to wet snow in respectively the avalanche image *'20130610'* and the reference image *'20130914'*. This is also validated in Section 6.3.

Quantitative analysis and discussion

A mask is created from the shape file containing the manually delineated debris fields to perform a quantitative analysis. Using this mask the backscatter coefficient, slope angle

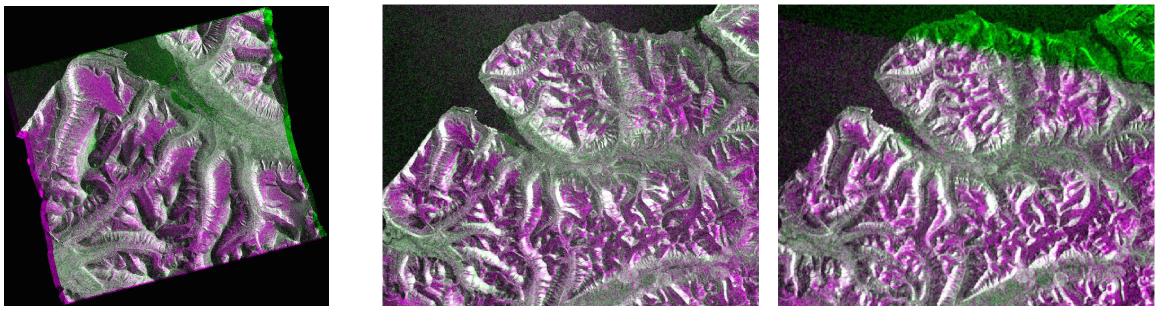

(a) UF
ascending - 20x20km

(b) SCNA
ascending - 40x50km

(c) SCWA
descending - 40x50km

Figure 6.1: RADARSAT-2 RGB images covering Nordenskiöld Land on Svalbard. The RGB image in UF mode is created by an avalanche image from 2013.06.10 and a reference image from 2013.09.14 botin in 'VV'-polarisation, while the SCNA and SCWA mode RGB images are constructed by an image from 2013.06.08 and a reference image from 2013.09.12 both in 'HV'-polarisation. An explanation of constructing RGB images is given in Section 3.3.2.

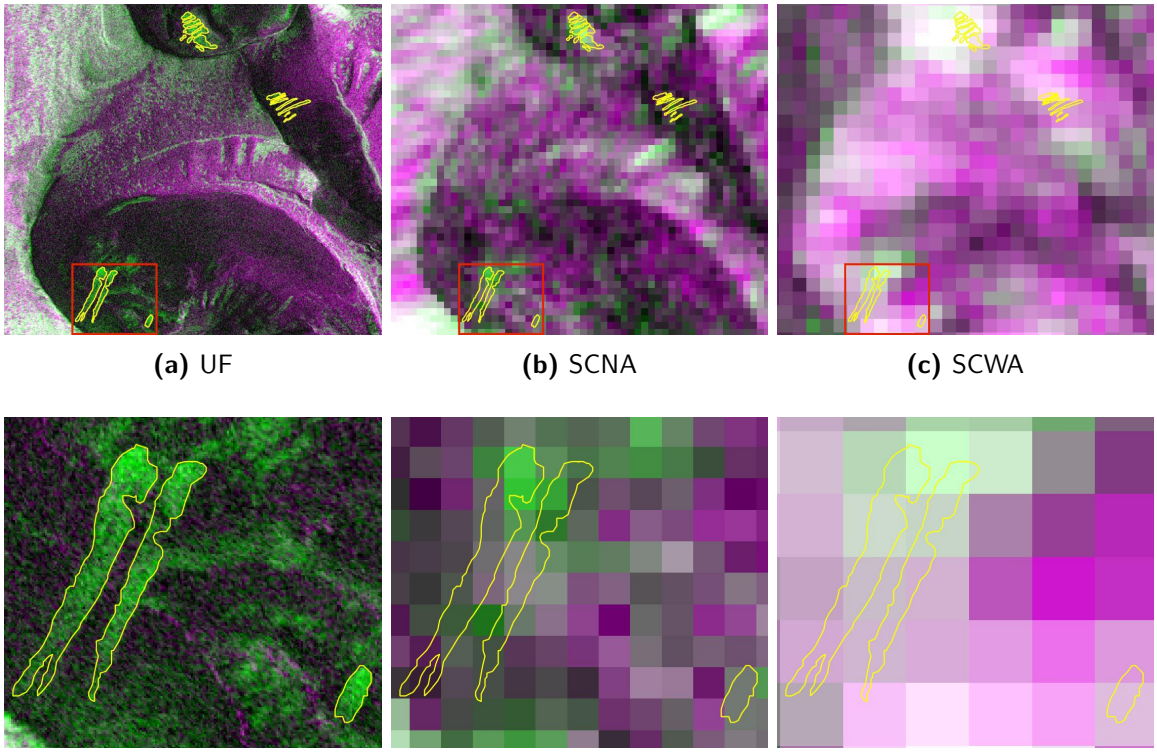

(a) UF

(b) SCNA

(c) SCWA

(d) UF - zoom

(e) SCNA - zoom

(f) SCWA - zoom

Figure 6.2: Zoomed views of RADARSAT-2 RGB images shown in Figure 6.1. Manual detection is performed on UF mode image and overlaid on SCNA and SCWA mode images in yellow. It can be seen that although an enhanced backscatter (bright green pixels) is observed within yellow outlined debris fields in SCNA and SCWA mode images, the tongue-shape is not noticeable due to their coarse resolution. However, the UF mode image does show the tongue-shape and is thus used for both manual and automatic detection.

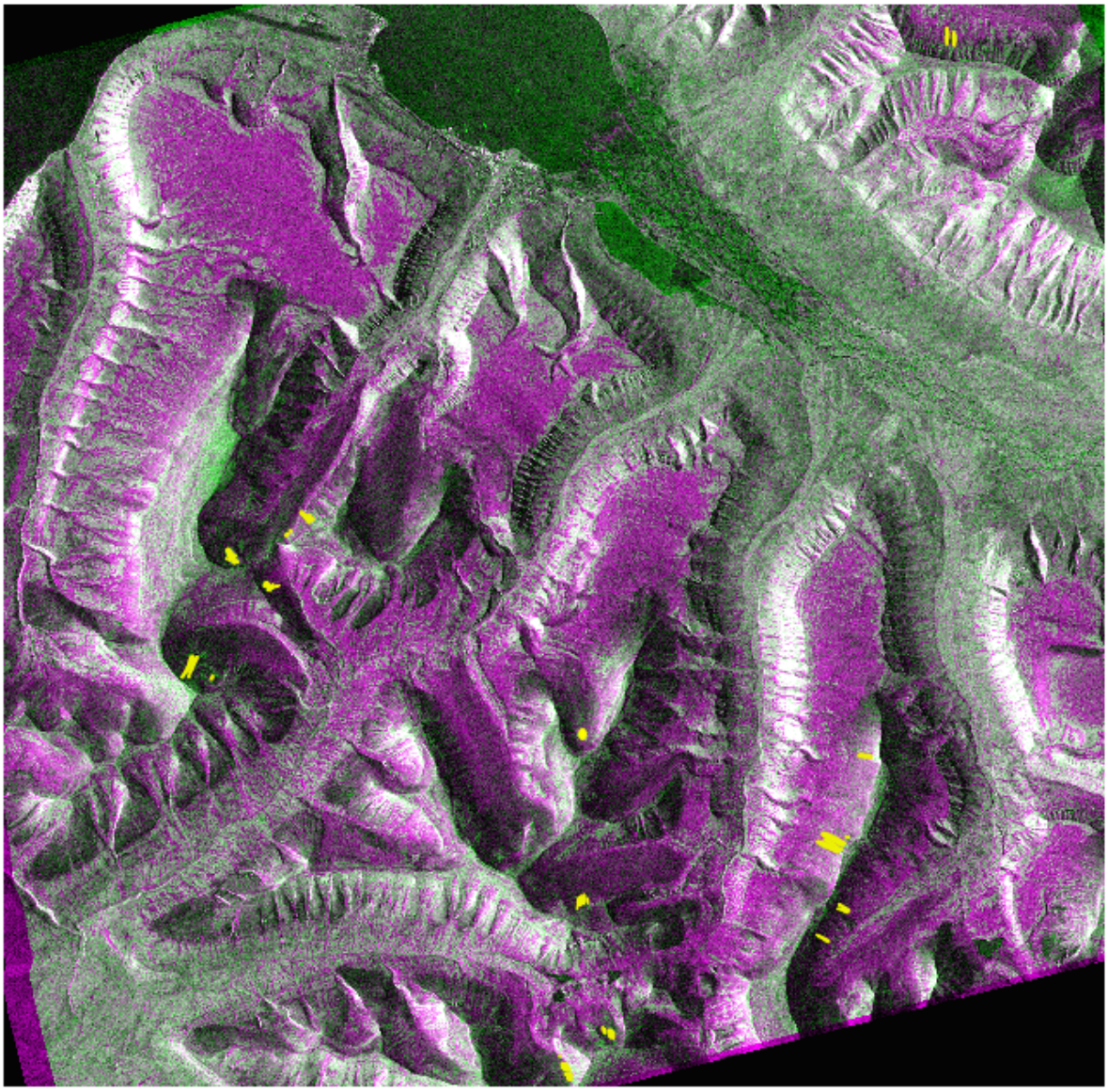

Figure 6.3: Manually detected avalanches outlined in yellow on top of the RADARSAT-2 UF mode image in RGB. The RGB image is created by an avalanche image from 2013.06.10 and a reference image from 2013.09.14. In total 13 debris fields were manually detected. The pink areas are a consequence of low backscatter in the avalanche image, while the green areas are due to low backscatter in the avalanche image. A low backscatter is caused by wet snow.

and local incidence angle within the manually detected avalanches is determined in both *'20130610'* and the reference image *'20130914'*. Figure 6.4 shows the histograms of the backscatter coefficients inside the manually detected avalanches. The blue and red histograms are from *'20130610'* and *'20130914'*, respectively. As explained in Section 3.3, it is expected that the mean backscatter coefficient inside the detected avalanches is higher for *'20130610'* than for *'20130914'* due to the increased surface roughness of the avalanche debris. This figure supports the statement as the histogram of *'20130610'* is located more towards the positive backscatter values.

Table 6.1: Size of manually detected avalanches in RADARSAT-2 UF mode image determined using a Measuring Tool in Envi. Also given is whether an enhanced backscatter is observed in the SCNA and SCWA mode images (Y=Yes, N=No), total number of detections per beam mode and average length and width of detected avalanches.

#	Aspect	Length [m]	Width [m]	UF	SCNA	SCWA
1	NE	400-450	40-50	Y	Y	Y
2	NE	100-120	20-30	Y	Y	N
3	NE	140-250	10	Y	N	N
4	NW	140-270	50-60	Y	Y	Y
5	NW	120-130	50-60	Y	Y	Y
6	NW	100-110	15-30	Y	Y	N
7	NW	100-180	15-40	Y	N	Y
8	S	270	35	Y	N	N
9	S	235-240	25-35	Y	N	N
10	NW	365-445	30-70	Y	Y	Y
11	NW	240-255	55	Y	Y	N
12	NW	320-330	30-50	Y	Y	N
13	NW	120-190	30-50	Y	N	N
Total				13	8	5
Range		100-450	10-70			

Also visible in this image is that both histograms show a double hump in relative frequency. Using the Digital Elevation Model (DEM) both a map showing the aspect of all slopes is created as well as a map showing the slope angles. These maps are shown in Figures 6.6 and 6.7, respectively. The aspect map is used to determine the aspect of the detected avalanches. The detected avalanches can roughly be divided into northeast-, northwest and south(west/east)-facing, respectively NE, NW and S. Most of the detected avalanches occurred on NW-facing slopes - see Table 6.2. The NE-facing debris fields have a mean backscatter value of approximately -12dB for *'20130610'* and -18dB for *'20130914'*, while the NW-facing avalanches have a respectively mean backscatter of approximately -4dB and -10dB. These mean values correspond well to the peaks as seen in the histograms of Figure 6.4. The double hump is thus most probably due to the distribution of slope aspects where the avalanches have occurred. To perform a more profound analysis on the difference in backscatter coefficients between *'20130610'* and *'20130914'* three avalanche debris fields are isolated - see the next paragraph.

The local incidence angle is the angle between the radar and the normal of the object reflecting the beam. Both the aspect of the slope and the slope angle have an influence on the local incidence angle. From Figure 6.5 it can be seen that with increasing local incidence angle the backscatter decreases. For the ascending image lower backscatter values are observed at NE-facing slopes; having a higher local incidence angles. On the other hand higher backscatter coefficients are observed at NW-facing slopes having a lower incidence angle.

The slope angle at the location of the manually detected avalanches is analysed. As stated in Section 2.1 slab avalanches generally occur on slopes between 25^o and 55^o. According to Figure 6.8 values vary between approximately 7^o and 46^o, which corresponds well to theory. The lower slope angles stem from avalanche run-out zones and slush avalanches, which occur on slopes between 5^o and 20^o.

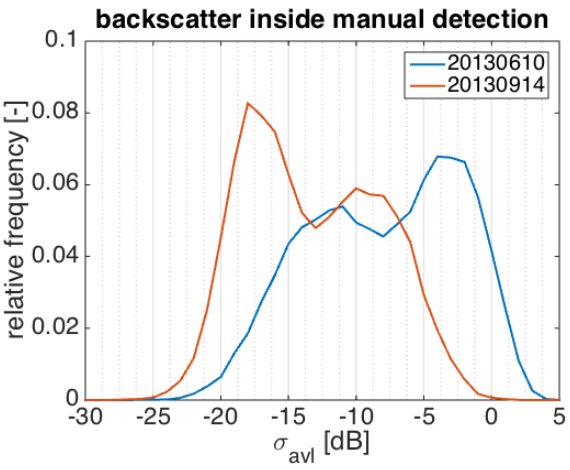

Figure 6.4: Histograms of all backscatter coefficients inside manually detected avalanches of RADARSAT-2 UF mode image *'20130610'* (blue) and reference image *'20130914'* (red). The double hump in both histograms is most probably caused by the distribution of slope aspects where avalanches have occurred. As expected manually detected avalanches (blue) show a higher backscatter value, i.e. shift to the right, compared to reference image (red) due to an increased surface roughness of debris fields.

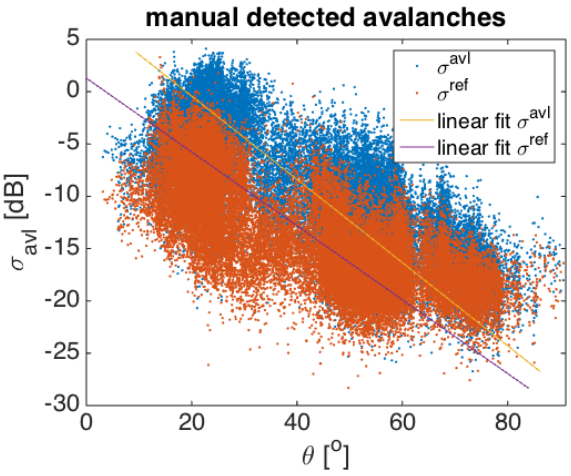

Figure 6.5: Scatter plot of local incidence angles θ versus backscatter coefficients σ_{avl} of manually detected avalanches in RADARSAT-2 UF mode images *'20130610'* (blue) and *'20130914'* (red). The corresponding linear trends are shown in yellow for avalanche image and in purple for reference image. The avalanche image *'20130610'* returns higher backscatter signals for lower local incidence angles causing a steeper trend than in case of reference image *'20130914'*. The three dense regions are caused due to the distribution of debris fields over different slope aspects.

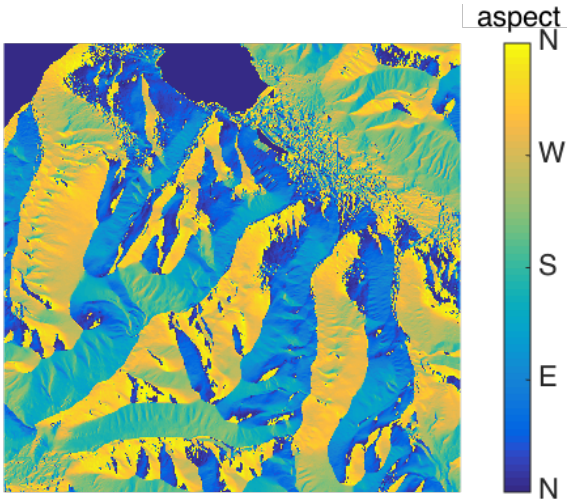

Figure 6.6: Map showing aspect of all mountain slopes within area covered by RADARSAT-2 UF mode images: Nordenkiöld Land on Svalbard. The slop aspect is determined using the DEM presented in Section 5.2 and used to determine slope aspect at location of debris fields.

Table 6.2: Mean backscatter of avalanche debris fields per slope aspect for both *'20130610'* (σ_{avl}) and *'20130914'* (σ_{ref}). Most of manually detected avalanches occurred on northwest (NW)-facing slopes. The debris fields on West-facing slopes have a higher mean backscatter coefficient compared to ones located on East-facing slopes. This is due to differing local incidence angles at both slope aspects.

	NW	SW	SE	NE
Debris fields	8	1	1	3
Mean σ_{avl} [dB]	-4	-8	-15	-12
Mean σ_{ref} [dB]	-10	-11	-17	-17
$\Delta\sigma$ [dB]	6	3	2	5

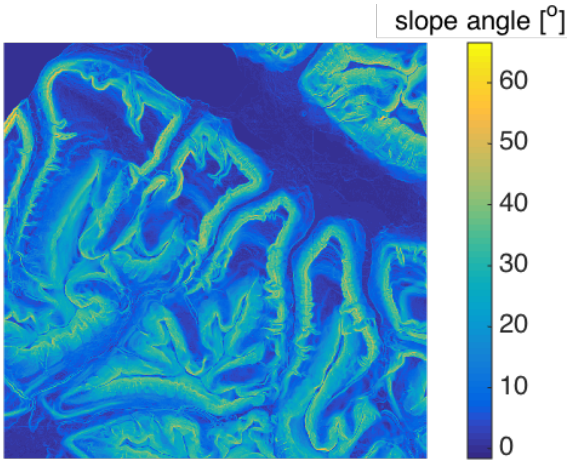

Figure 6.7: Map showing slope angles of mountains within area covered by RADARSAT-2 UF mode images: Nordenkiöld Land on Svalbard. This map is determined using the DEM presented in Section 5.2 and used for analysis of slope angles where debris fields are located.

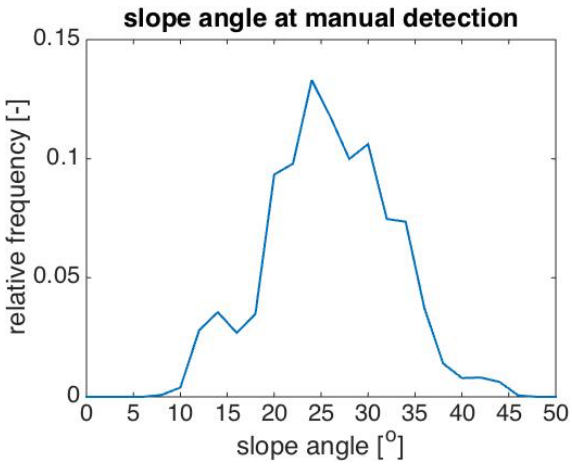

Figure 6.8: Histogram of slope angles at locations of manually detected avalanches in RADARSAT-2 UF mode images. Avalanches are detected on slope angles between 7^o and 46^o. The lower values stem from the avalanche run-out zones and slush avalanches, which occur on slopes between 5^o and 20^o. The found values are consistent with theory (McClung and Schaerer, 2011).

Subwindow selection

Figure 6.2d shows the outlines of the manually delineated avalanches within the three windows. The avalanche debris fields within Window 1 and 2 are located on glaciers, respectively Dyadrebreen and Longyearbreen. The avalanche of Window 3 lies on the way from Longyearbreen to Fardalen. All three avalanche debris fields are found on NE-facing slopes. A shape file created from the manually detected debris fields is used to determine the differences in backscatter coefficient inside and outside the avalanches for *'20130610'* and *'20130914'*. Figure 6.10 shows the histograms corresponding to these difference in backscatter. For all three windows the backscatter within the debris fields is higher than the backscatter coefficient of the surrounding unperturbed snow, i.e. the blue histogram is shifter towards the right relative to the orange histogram. The backscatter coefficient outside of the detected avalanches is comparable. Thus the higher backscatter is caused by the increase in surface roughness and snow density of the debris fields.

The border between assigning too little or too many pixels to the avalanche class lies around the point where the histograms cross. For windows 1 and 2 the crossing point lies around $2 - 3dB$, but for Window 3 it is almost at $0dB$. This lower value could be due to the fact that the avalanche occurred earlier and precipitation and/or wind has covered the debris field causing a decrease in surface roughness. Due to the variation in backscatter difference it is challenging to find a good compromise between the probability of detecting the avalanches and the number of false alarms. Therefore, adaptive threshold values are tested to find the best midway.

(a) Window 1 **(b)** Window 2 **(c)** Window 3

Figure 6.9: Masks created to either clip out σ_{avl} (white) or mask out σ_{out} (black) manually detected avalanches in one of three defined windows within RADARSAT-2 UF mode images.

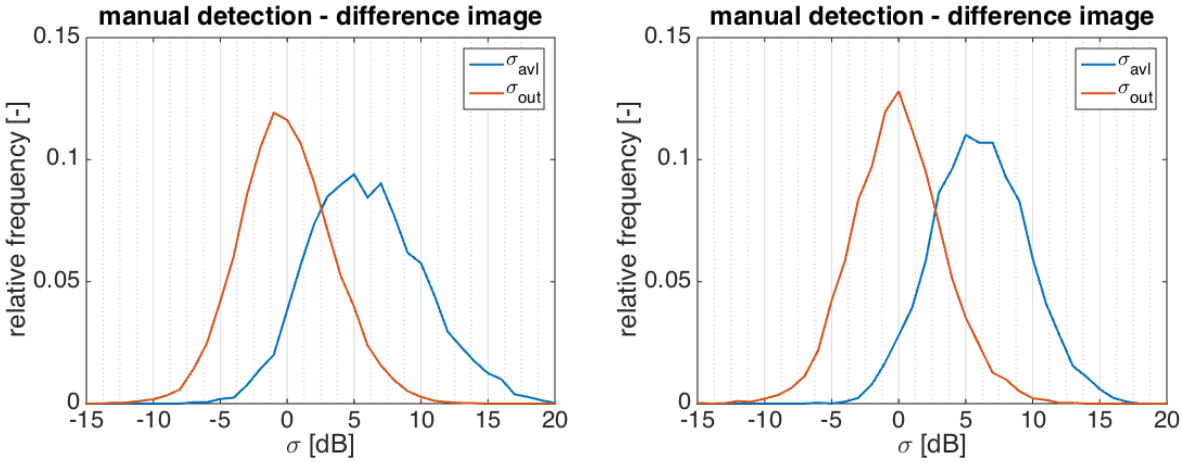

(a) Window 1 **(b)** Window 2

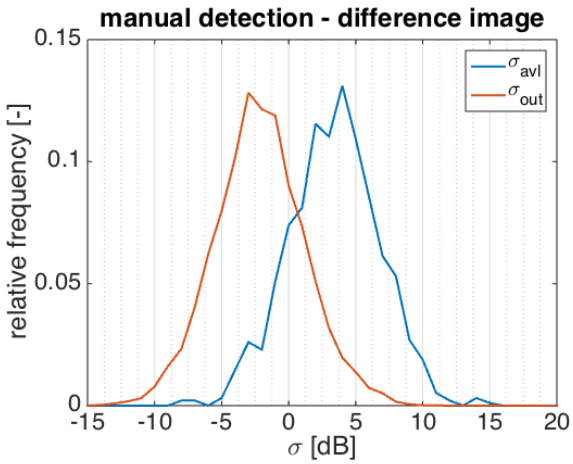

(c) Window 3

Figure 6.10: Histograms of difference in backscatter coefficient between *'20130610'* and *'20130914'*, both inside σ_{avl} and outside σ_{out} three selected manually detected avalanche debris fields from RADARSAT-2 UF mode images. The difference in backscatter coefficient inside manually detected avalanches for all three windows is higher compared due to surrounding unperturbed snow. The histogram of the difference between *'20130610'* and *'20130914'* outside of debris fields lies around zero, i.e. there is little change in backscatter for these areas. The higher backscatter within debris fields is caused by an increase in surface roughness and snow density.

6.1.3 Automatic detection

This section shows the results of the automatic detection applied on the UF mode images. First, a median filter of 5x5 pixels is applied on both *'20130610'* and reference image *'20130914'* separately. This is done to reduce speckle - see Subsection 3.1.2. Following the steps as presented in Section 4.3 a difference image is created from the two images, followed by a slope mask to extract areas prone to avalanches - see step 3 in Section 4.3. Hereafter, the slope angle mask and layover & shadow mask are applied onto the difference image.

The thresholding of the automatic detection is based on the difference in backscatter coefficient between the avalanche and the reference image. Therefore, threshold values between 1.5 and $3dB$ with steps of $0.1dB$ are used. As only applying a threshold leads to many false alarms, a post-classification filter is needed as well. Two types of filters are tested; a median filter and a Remove Small Objects (RSO) filter. Both methods are explained in Section 4.3 and the results are presented hereafter.

To analyse the effect on the detectability of the tongue-shaped features the automatic detection methods are applied on the three isolated windows. The output is given by True Negative (TN), True Positive (TP), False Negative (FN) and False Positive (FP) in respectively grey, blue, red and yellow. Thus the pixels detected as avalanche by both the manual and automatic detection are given in blue. The pixels shown in red are the ones identified as avalanche by only the manual detection. And the pixels incorrectly allocated to the avalanche class by the automatic detection method are visualised in yellow.

Post-classification 1: Median filter

From the filter sizes tested, i.e. 3x3, 5x5 and 7x7, a window size of 5x5 pixels gave the best output; sufficient number of TPs and as little FPs as possible. Figure 6.11 shows the output when applying a threshold of 1.5, 1.9, 2 and $2.5dB$ and the median filter afterwards. The result of all threshold value between $1.5db$ and $3db$ with steps of $0.1dB$ are presented in Appendix A.1. From these images it can be seen that by using a threshold of $1.9dB$ or lower all manually detected avalanches are identified, whereas using a threshold of $2.5dB$, 10 out of 13 debris fields are detected by only few pixels. This causes the tongue-shaped not to be distinguishable anymore. On the other hand, the number of false alarms decreases for higher threshold values. The large black areas on the left- and right-side stem from glaciers located on mountain plateaus. The snow on top of the glacier ice melts away at the end of the summer which causes the large difference in backscatter between the avalanche image and reference image as the reference image captures the bare ice. A more thorough assessment on the probability of detection and the false alarms is found in Section 6.2.

Figure 6.12 shows the results of the automatic detection zoomed in on windows 1, 2 and 3. The threshold values below $2db$ are left out as they gave too many false alarms. It can be seen that the applied threshold values 2, 2.5 and $3dB$ work quite well for windows 1 and 2. However, the tongue-shaped feature of Window 3 is not detected at all, not even for the lower threshold values. As the histograms of *'20130610'* and *'20130914'* corresponding to this window intersected at around $0dB$ it is expected that the debris field is not detected at these high threshold values. However, selecting a lower threshold value leads to many false alarms. From these images it becomes clear that finding a good balance between TPs and FPs is challenging.

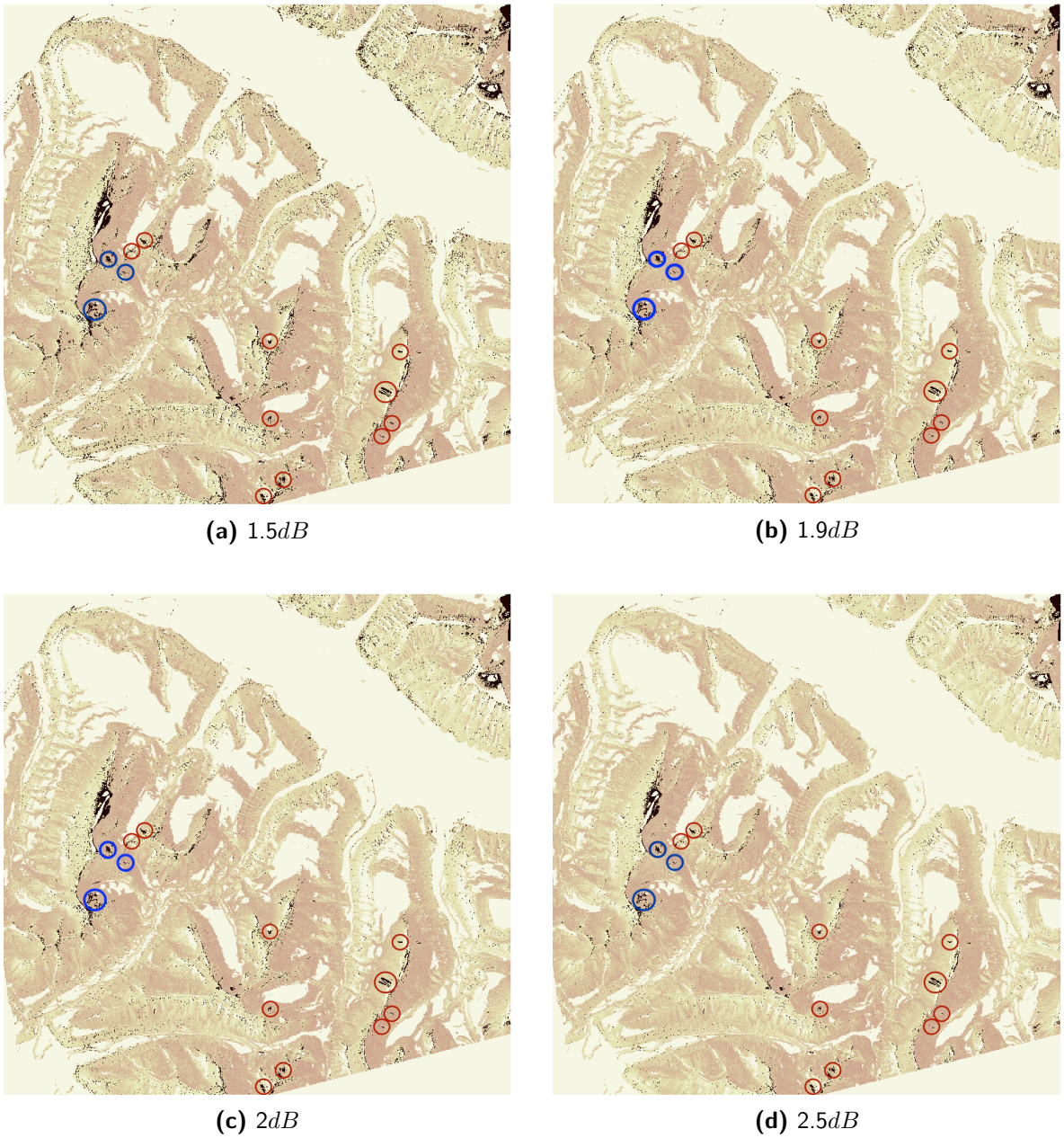

(a) 1.5dB **(b)** 1.9dB

(c) 2dB **(d)** 2.5dB

Figure 6.11: Results of automatic detection method using post-classification filter 1: Median filter and threshold values of 1.5dB, 1.9dB, 2dB and 2.5dB. The method is applied on RADARSAT-2 UF difference image in 'VV'-polarisation from *'20130610'* and *'20130914'* and shown in black. The manually detected debris fields are encircled in red and the debris fields isolated for further analysis are encircled in blue. The black areas outside blue and red circles are false alarms of which some are more obvious falsely identified than others. The large black areas on the left- and right-side stem from glaciers located on mountain plateaus; snow on top of glacier ice melts away at the end of summer, which causes the large difference in backscatter between avalanche and reference image (when bare ice is captured).

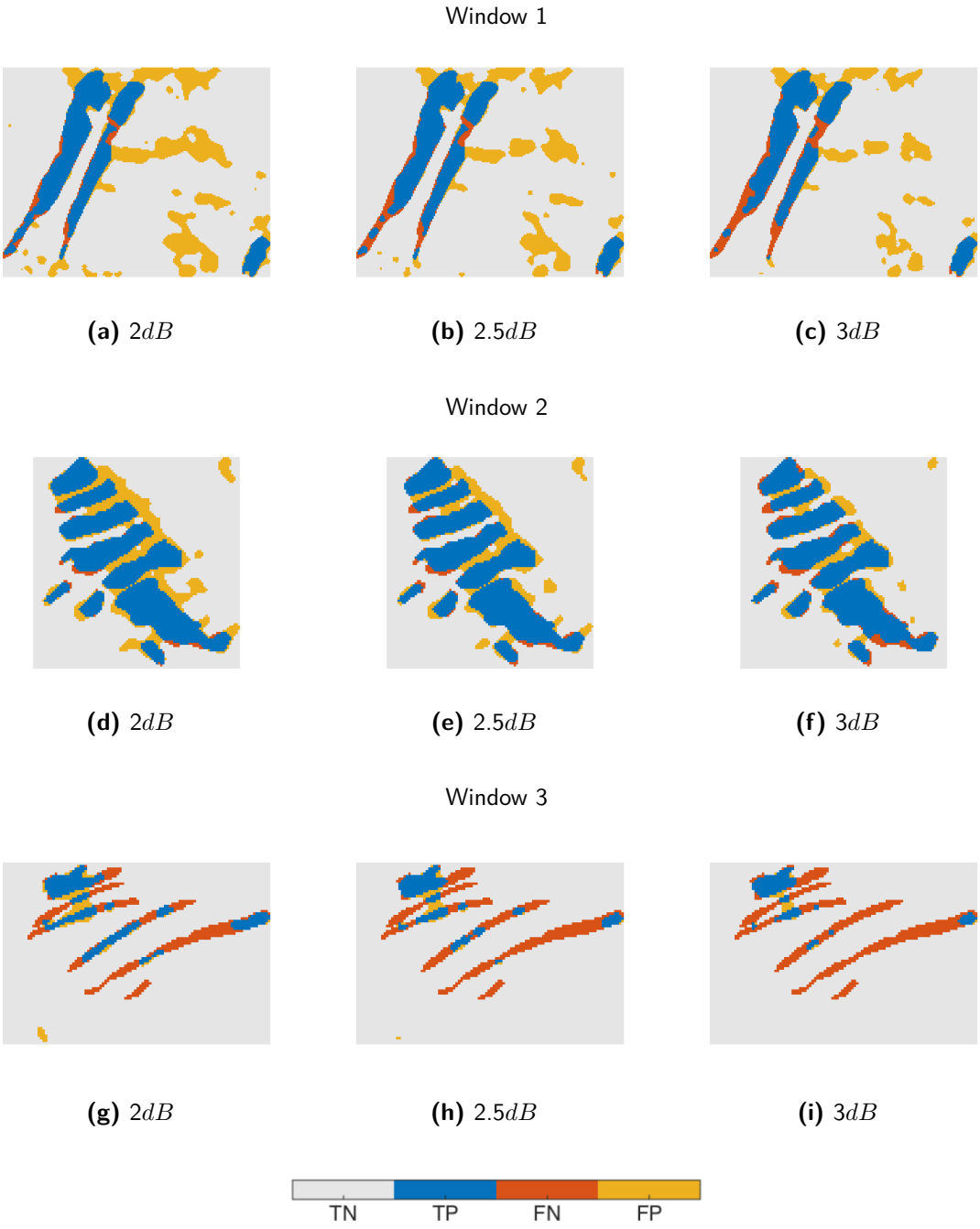

(a) $2dB$ **(b)** $2.5dB$ **(c)** $3dB$

(d) $2dB$ **(e)** $2.5dB$ **(f)** $3dB$

(g) $2dB$ **(h)** $2.5dB$ **(i)** $3dB$

Figure 6.12: Results of automatic detection method using post-classification filter 1: Median filter and threshold values of $2dB$, $2.5dB$ and $3dB$. The method is applied on three defined windows within RADARSAT-2 UF difference image in 'VV'-polarisation from *'20130610'* and *'20130914*. True Negatives (TN), True Positives (TP), False Negatives (FN) and False Positives (FP) are indicated in respectively grey, blue, red and yellow. The tongue-shape consistent with avalanche debris is captured very well in Windows 1 and 2, while for Window 3 the automatic detection does not detect the debris field enough to recognise it as an avalanche. The detectability of the extent of debris fields does not change much with increasing threshold value, thus thresholding has more influence on detecting the location than extent of an avalanche.

Post-classification filter 2: RSO filter

To test whether better results can be obtained, a second post-classification filter was designed. The RSO filter eliminates small groups of pixels, after thresholding, that are not assumed to be belonging to the avalanche class. For a more extend explanation of this filter see Section 4.3. The size of the pixel groups range from 500-5000$pixels$. These numbers are based on the values in Table 6.1 and are corrected for the pixel spacing of $3m$. The output of the detection method for the threshold values between 2 and $3dB$ with steps of $0.1dB$ can be found in Appendix A.2. Figure 6.13 shows the output when using threshold values of 1.5, 2, 2.5 and $3dB$. It can be seen that six out of twelve groups of avalanche debris fields are detected automatically for all selected thresholds. Although the number of avalanches detected does not change with increasing threshold value the number of false alarms does decrease.

Figure 6.14 shows the results of the automatic detection zoomed in on the three earlier defined windows. These zoomed images show even more clear that increasing the threshold lowers the false alarms, but also for the higher thresholds (from $2.8dB$ onwards) large parts of the avalanche debris fields are lost. None of the pixels within Window 3 is assigned to the avalanche class, which is probably due to the fact that the avalanche debris field is too small or at least the number of pixels with an enhanced backscatter is too small and therefore discarded by the RSO filter. To find a suitable threshold value a more quantified analysis is needed. This is done by calculating the probability of detection and false alarms as will be explained in the next section.

6.2 Discussion on results of the automatic detection

The avalanche maps per threshold value show that when increasing the threshold the number of false alarms decreases as well as does the number of correct identified debris fields. Also the difference between the median filter and the RSO filter can be noticed. The RSO filter clearly shows less false alarms - see Figures 6.11 and 6.13. However, the number of detected avalanches is also slightly lower. For the lowest threshold value of $1.5dB$, the RSO filter does not even detect three out of the 13 avalanches as such. These three debris fields are the smaller ones, and probably these are discarded by the filter due to the low number of very enhanced pixels within the debris fields. For the RSO filter there is a transition between $2.7dB$ and $2.8dB$ where tongue-shape is lost of at least one of the avalanches. The amount of noise is low for this filter and the avalanche map looks clear. For the median filter, the detectability of the extent of the debris fields does not change much with increasing threshold value. Thus thresholding has more influence on detecting the location than on the extent of the avalanche - see Figure 6.12.

To check the detectability of the debris fields both automatic detection methods are compared to the results of the manual detection. The number of manually and automatically detected debris fields per threshold value are counted for post-classification filter 1: Median filter and post-classification filter 2: RSO filter and are presented in Tables 6.3a and 6.3b, respectively. Shown in the table are the TPs, the FPs or false alarms and the True Positive Rate (TPR) or probability of detection - see also Section 4.4. The tables include all threshold values from $1.5dB$ up to $3dB$ of which the corresponding avalanche maps are shown in Appendices A.1 and A.2. The TP are counted in such way that it should be clear that the group of pixels denote an avalanche otherwise the group of pixels is not assumed to be an avalanche.

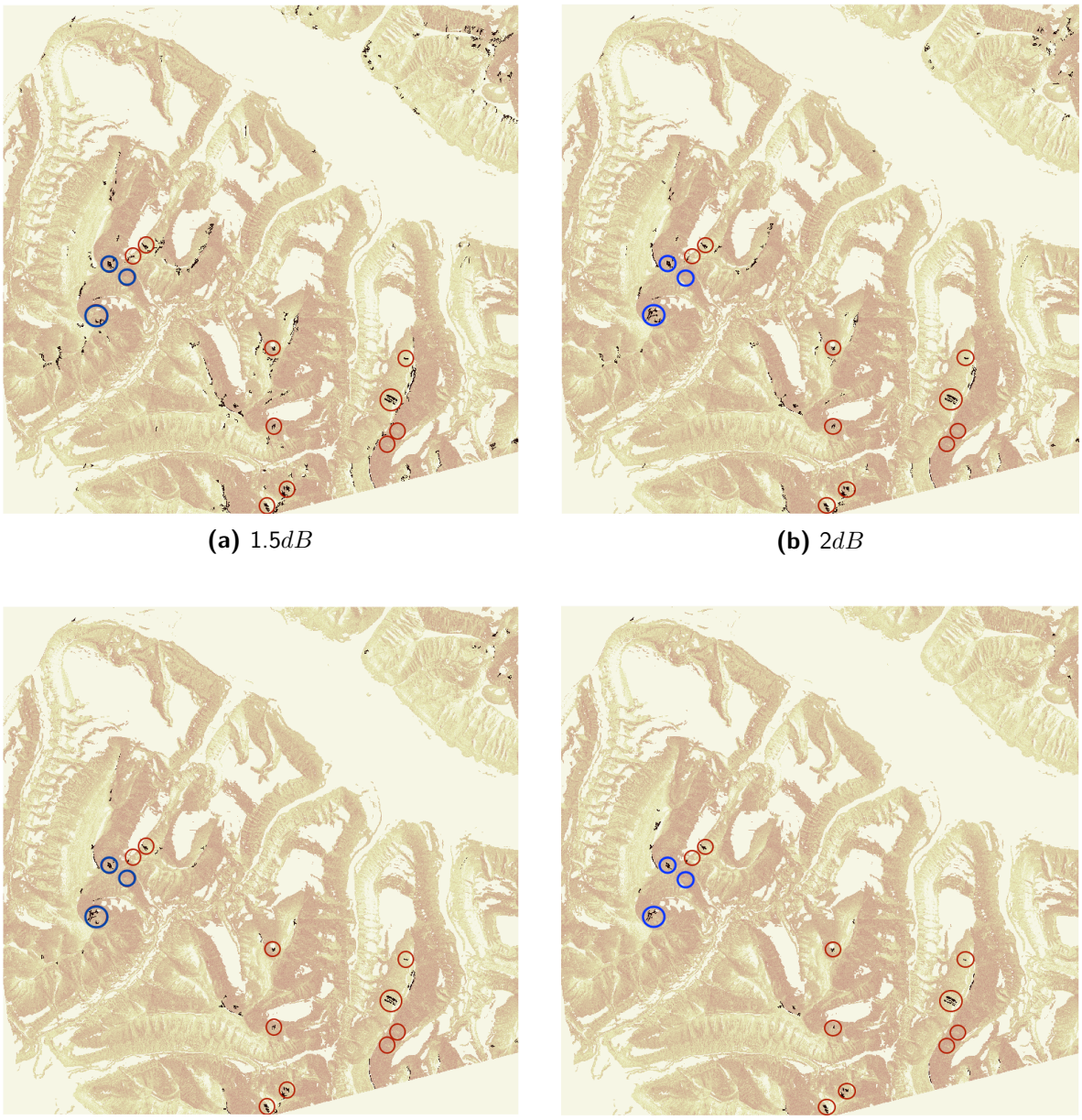

(a) 1.5dB **(b)** 2dB

(c) 2.5dB **(d)** 3dB

Figure 6.13: Results of automatic detection method using post-classification filter 2: RSO filter and threshold values of 1.5dB, 2dB, 2.5dB and 3dB. The method is applied on RADARSAT-2 UF difference image in 'VV'-polarisation from *'20130610'* and *'20130914'* and shown in black. The manually detected debris fields are encircled in red and the debris fields isolated for further analysis are encircled in blue. The black areas outside blue and red circles are false alarms of which some are more obvious falsely identified than others.

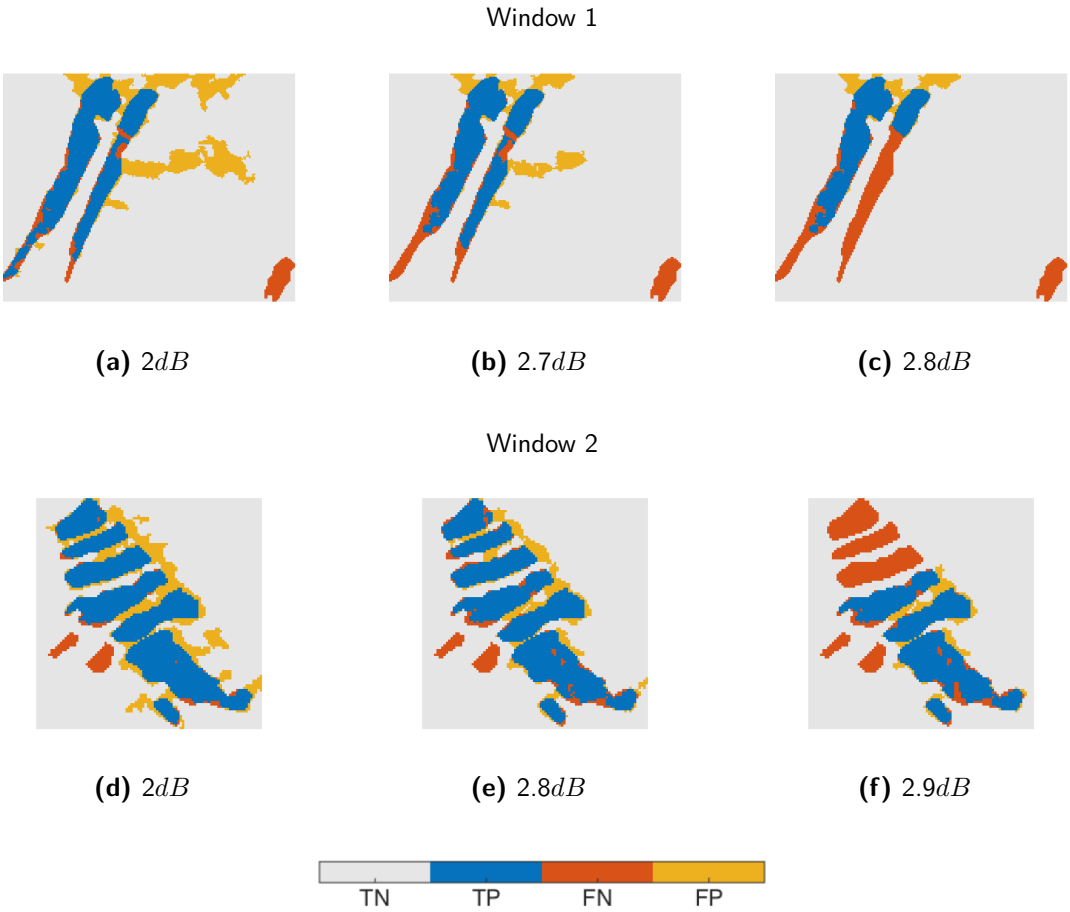

Figure 6.14: Results of automatic detection method using post-classification filter 2: RSO filter and threshold values of $2dB$, $2.7dB$, $2.8dB$ and $2.9dB$. The method is applied on three defined windows within RADARSAT-2 UF difference image in 'VV'-polarisation from *'20130610'* and *'20130914'*. True Negatives (TN), True Positives (TP), False Negatives (FN) and False Positives (FP) are indicated in respectively grey, blue, red and yellow. The tongue-shape consistent with avalanche debris is captured quite well in Windows 1 and 2. For Window 1 the shape is lost for threshold values above $2.7dB$, while for Window 2 this happens from $2.9dB$ onwards. The debris field in Window 3 is not detected at all as it has too little pixels with an enhanced backscatter, i.e. less than boundary set in RSO filter.

Table 6.3: Number of correct and false identified debris fields per threshold value for both post-classification 1 using a median filter and post-classification 2 using a RSO filter applied on RADARSAT-2 UF mode image. In total there are 13 debris fields detected manually. For an increase in threshold value the number of false alarms (FP) decreases as well as the number of correct identified debris fields (TP) and thus the probability of detection (TPR).

Threshold $[dB]$	TP $[-]$	TPR $[\%]$	FP $[-]$
1.5	13	100	>50
1.6	13	100	>50
1.7	13	100	>50
1.8	13	100	>50
1.9	13	100	>50
2	12	92	>50
2.1	12	92	>50
2.2	10	77	>50
2.3	10	77	>50
2.4	9	77	>50
2.5	10	77	>50
2.6	10	77	>50
2.7	10	77	>50
2.8	10	77	>50
2.9	9	69	>50
3	8	62	>50

(a) Median filter

Threshold $[dB]$	TP $[-]$	TPR $[\%]$	FP $[-]$
1.5	10	77	>20
1.6	10	77	>20
1.7	9	69	>20
1.8	9	69	>20
1.9	9	69	>20
2	9	69	>20
2.1	9	69	>20
2.2	9	69	>20
2.3	9	69	>20
2.4	9	69	>20
2.5	9	69	>20
2.6	9	69	>20
2.7	8	62	>20
2.8	7	54	>20
2.9	7	54	18
3	7	54	16

(b) RSO filter

The probability of detection using a median filter drops from 100% to 62% for threshold values $1.5dB$ and $3dB$, respectively - see Table 6.3a. The tipping point where not all debris fields are detected anymore is around 1.9-2dB. The number of false alarms using this filter is very high (>50) for all threshold values between $1.5dB$ and $3dB$. For the RSO filter the number of false alarms was lower, but at the expense of probability of detection - see Table 6.3b. For a threshold of $1.5dB$ the detectability was 77% and >20 false alarms were identified, while for a threshold of $3dB$ the probability was 54% and only 16 groups of pixels were falsely detected. Although the probability of detection is higher for the median filter than when for using the RSO filter, the noise is much higher as well. Due to the many false alarms, especially for the lower threshold values, it is hard to distinguish actual debris fields from false alarms. The reason for not detecting avalanches could be because of wet snow in the reference image. This causes the difference in backscatter between the avalanche and reference image too be lower than the set threshold or the number of pixels with an enhanced backscatter less than the set boundary in the RSO filter.

By analysing the isolated avalanches in the three defined windows it can be seen that the probability of detection depends on both the size of the debris fields as well as on the difference in backscatter coefficient between the avalanche and reference image. That is to say the avalanche in Window 3 is hardly detected by the median filter method and not at all detected using the RSO filter which is due to the fact that the avalanche image does not have as much as an increase in backscatter at the location of the debris fields as for the other two windows. In the case of Window 1, the tongue-shape of the avalanche is better captured using the RSO filter for threshold values up to and including $2.4dB$ - see Appendix A.2 . The number of false identified pixels is also limited, whereas the median filter results in many more false alarms. On the other hand, the debris field in Window 2 is fully detected by the automatic detection using the median filter with only a few false alarms - see Appendix A.1. Whereas the RSO filter 'misses' some areas of the debris field, but does capture most of it up until a threshold of $2.8dB$ with only a few false alarms as well.

6.3 Validation

Although the tongue-shaped features denoting avalanches were not detectable in the SCNA and SCWA images, an enhanced backscatter was noticeable. Thus the avalanches must have occurred before the acquisition date of the ScanSAR mode images which is June 8, 2013. However, the avalanches could have been released any day. To derive the exact release date more information is needed, e.g. satellite images with high temporal resolution or in-situ observations. Additional meteorological data can also be helpful to estimate the release date.

Crowd-sourcing websites, such as regObs.no, were not as much in use at the time of the avalanche cycle and also other papers or news on avalanches at Svalbard in this period do not provide detailed information. Only one slush avalanche map was found (Markus Eckerstorfer, personal communication) and compared to the result of the manual detection. However, due to the high resolution the tongue-shaped features are fairly clear and consistent with avalanche debris fields and thus it can be assumed that they are correctly detected. Although it is not a fully qualified validation technique, the performed manual detection is assessed by letting other avalanche experts manually detect the same RGB image and comparing the results.

Meteorological data

The Norwegian Meteorological Institute provides weather data on their online database eKlima.no, including maximum air temperature and precipitation. The weather conditions at the time of the acquisitions is analysed using the meteorological data and wet snow cover maps obtained from Snow, Ice and Avalanche Applications (SNAPS). Figures 6.15 and 6.17 show the meteorological data from the acquisition dates in respectively June and September at the stations located on top of the mountain near Longyearbyen airport. Increasing air temperature and precipitation (additional loading) could cause an avalanche cycle, which apparently happened in this case. It can be seen that five days before the acquisition of the avalanche image *'20130610'* both the maximum air temperature and precipitation. The wet snow cover maps are shown in Figures 6.16 and 6.18. Due to the increased air temperature already existing dry snow (white areas in Figure 6.16a) turned into wet snow. Comparing the wet snow cover maps to the RGB image in Figure 6.3, it can be seen that the wet snow areas (in red) correspond to the pink areas in the RGB image. These pink areas are thus from wet snow in *'20130610'*.

Figures 6.15 and 6.18 show the meteorological conditions at the time of the acquisition of the reference image *'20130914'* and the wet snow cover maps from a few days before, respectively. It can be seen that little wet snow is present. The wet snow cover maps from June and September are consistent with the RGB image shown in Figure 6.3; the wet snow areas shown in red in the June wet snow cover images correspond with the pink areas in the RGB image. The pink areas are thus due to the low backscatter of the wet snow in the avalanche image. According to Nagler and Rott (2000) the reference image is preferable obtained during dry snow conditions or in the snow-free summer. The wet snow cover maps from September show that the reference image was indeed acquired during dry snow conditions which improves the possibility of detecting avalanches. Obtaining an image in snow-free conditions on Svalbard is hard and so it is also possible to average a large number of scenes ($\sim$ 10-20 scenes) obtained in the period between September and April when likely only dry snow is present.

Field observations

On June 5^{th} in 2013 Markus Eckerstorfer and colleagues identified several slush avalanches in the vicinity of Longyearbyen. From these observations they created a map indicating the location and extent of the observed slush avalanches. This map is shown in Figure 6.19 (Markus Eckerstorfer, personal communication). Although the map has a smaller coverage than the UF mode image it is compared to the avalanche map to analyse any similarities. The orange circles in both images denote the two avalanche debris fields both observed in the field as well as by the satellite. The other slush avalanches are probably not visible in the satellite image as they are too small or have too little difference in backscatter coefficient between the slush avalanche and the reference image.

Manual detection by other operators

The manual detection as discussed in Subsection 6.1.2 is also performed by two other avalanche experts. Figures 6.21 and 6.22 show the manual detection by Markus Eckerstorfer and Hannah Vickers, respectively. They have indicated the enhanced backscatter areas they assume to be debris fields by green circles. The yellow arrow denote the manually detected debris field in this thesis and by Hannah Vickers, but not by Markus Eckerstorfer. On the other hand, the orange arrows indicate debris fields by the other operators, but not the ones identified earlier.

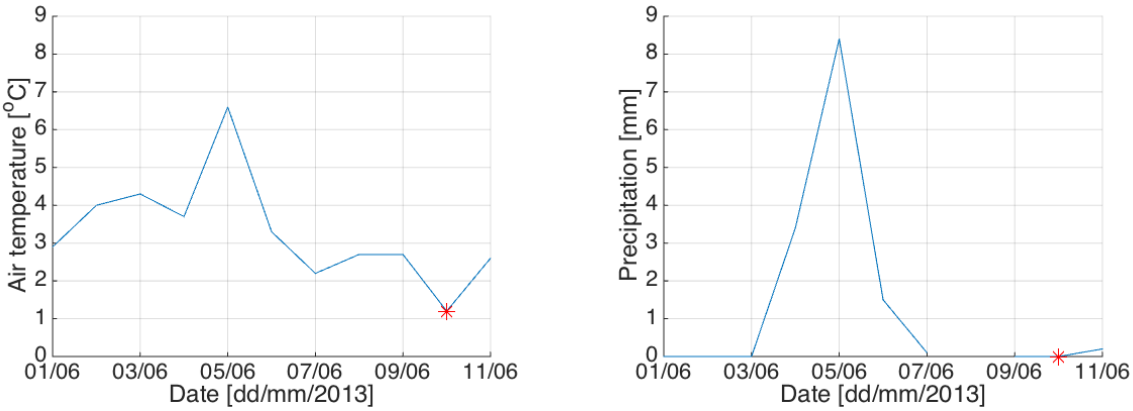

(a) Maximum air temperature **(b)** Precipitation

Figure 6.15: Meteorological data from June 2013 at Longyearbyen airport on Svalbard. The red asterisks denote the acquisition date of RADARSAT-2 avalanche image in UF mode: 2013.06.10. The increase in air temperature and precipitation event has caused the avalanche cycles as observed in the UF mode image. Data is obtained from eKlima.no (Norwegian Meteorological Institute).

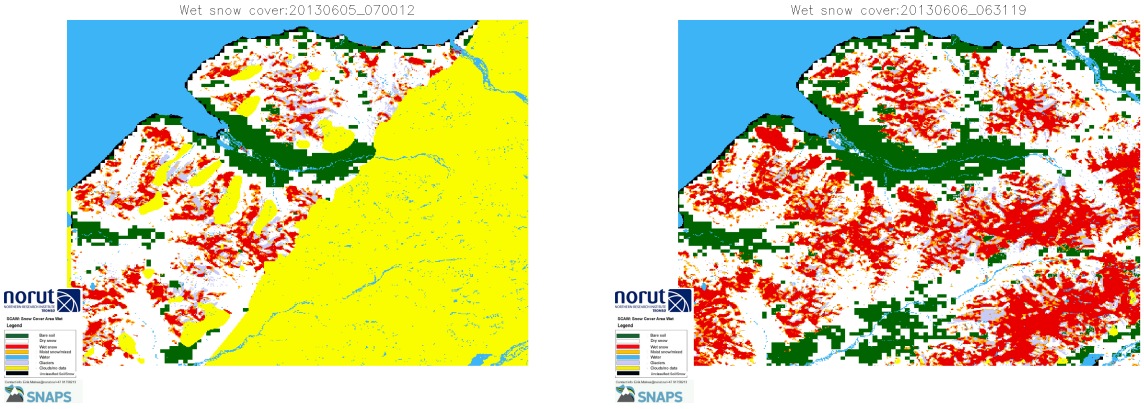

(a) 2013.06.05 **(b)** 2013.06.06

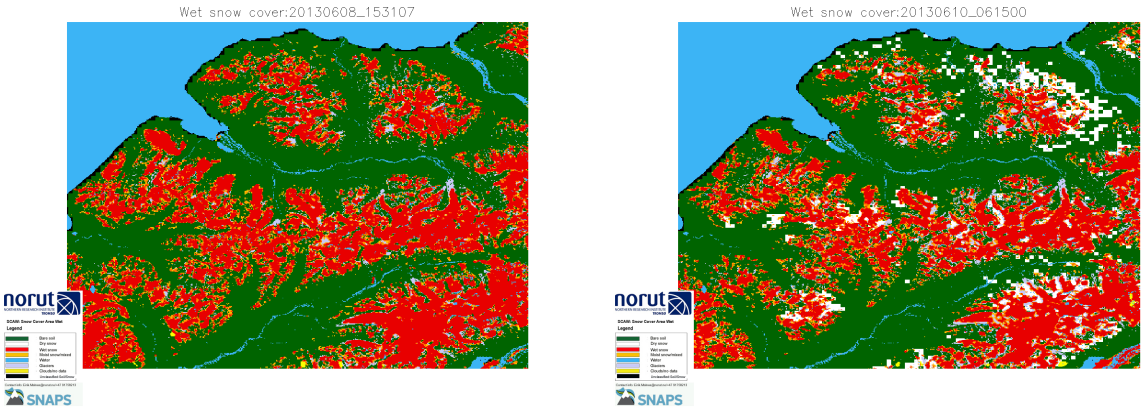

(c) 2013.06.08 **(d)** 2013.06.10

Figure 6.16: Wet snow cover maps from June 5^{th}, 6^{th}, 8^{th} and 10^{th}, 2013 covering Nordenskiöld Land on Svalbard. Bare soil is shown in green, dry snow in white, wet snow in red and no data areas, including regions covered by clouds, in yellow. As mostly wet snow is observed in the area, debris fields observed in RADARSAT-2 UF mode images stem most probably from wet snow avalanches. Maps are provided by SNAPS.

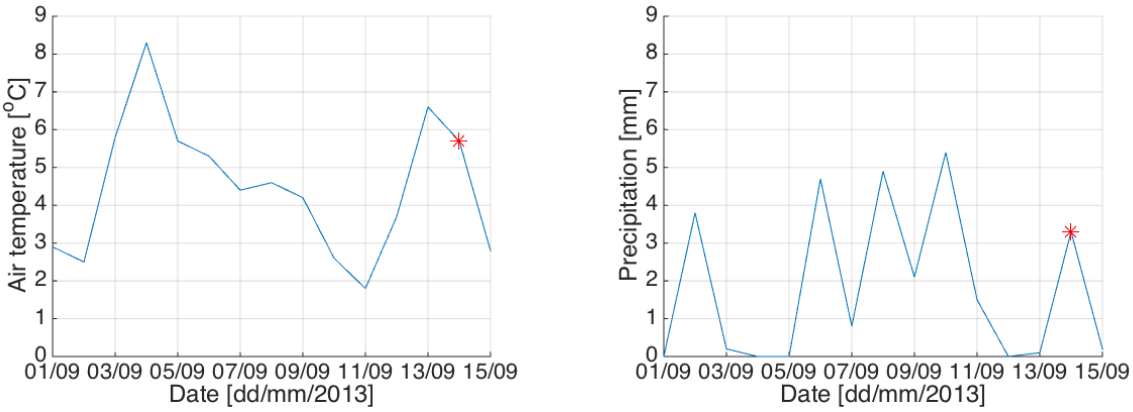

(a) Maximum air temperature **(b)** Precipitation

Figure 6.17: Meteorological data from September 2013 at Longyearbyen airport on Svalbard. The red asterisks denote the acquisition date of the RADARSAT-2 reference image in UF mode: 2013.09.14. The data is obtained from eKlima.no (Norwegian Meteorological Institute).

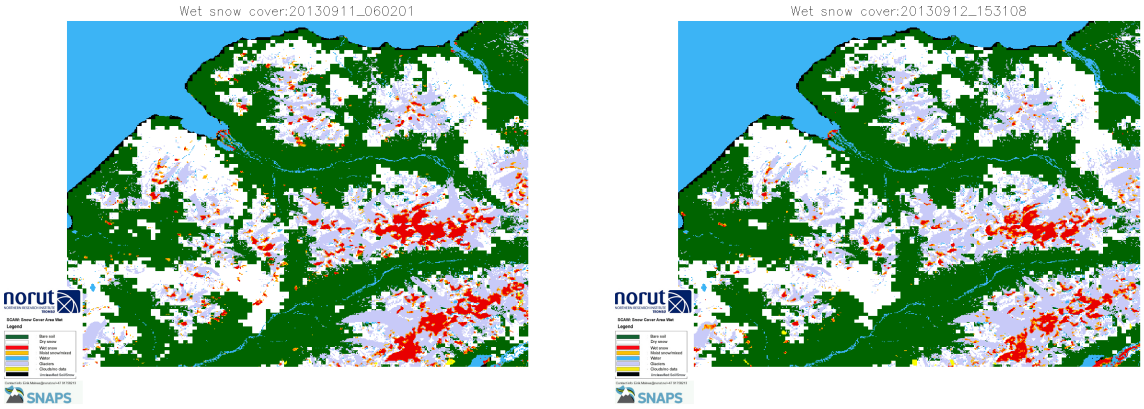

(a) 2013.09.11 **(b)** 2013.09.12

Figure 6.18: Wet snow cover maps from September 11^{th} and 12^{th}, 2013 covering Nordenskiöld Land on Svalbard. Bare soil is shown in green, dry snow in white, wet snow in red and no data areas, including regions covered by clouds, in yellow. The reference image *'20130914'* is thus acquired during dry snow and partially snow-free conditions. Maps are provided by SNAPS.

From the figures it can be seen that the manual detection performed in this thesis slightly underestimated the number of debris fields. Hannah Vickers identified two more debris fields, while Markus Eckerstorfer even detected five more avalanches. In case these identified areas are truly avalanches, the TP and False Positive Rate (FPR) would be higher and the FP lower as some of these enhanced backscatter are captured by both automatic detection methods.

6.4 Main findings

Several conclusions can be drawn from the avalanche detection methods, the quantitative analysis and assessment and the validation. Listed in the first paragraph are the main findings of the comparison of the beam modes and the analysis of the manual and automatic detection. The second paragraph gives the key findings of the validation of the detected avalanches.

Detected debris fields

- Images in UF mode are needed for both manual and automatic detection as the spatial resolution of SCNA and SCWA mode images is too coarse.
- The destructive-size of the manually detected avalanches can be categorised as D2 to D3. This means they vary between able to bury, injure or kill a person to being able to bury a car or destroy buildings - see also Table 2.1.
- The slope angles at the location of the avalanche debris fields are consistent with what is expected from theory. The angles varied between 10^o-45^o, while slab avalanches occur on slopes between 25^o-55^o (McClung and Schaerer, 2011). The lower angles are either located at the run-out zones of the avalanches or stem from slush avalanches, which occur on slopes between 5^o-20^o.
- NE-facing avalanches return a lower backscatter than NW-facing avalanches as the local incidence angle is higher for these avalanches.
- Most of the avalanches are located on NW-facing slopes (almost 2 out of 3). This could be due to the prevailing wind direction from the SE as a consequence from the semi-permanent Siberian high pressure and Icelandic low pressure system as experienced on Svalbard. The prevailing wind direction causes cornice formation overhanging on the NW-facing slopes. When these cornices fall they trigger slab avalanches on these slopes.
- When using a median filter with a window size of 5x5 pixels as post-classification filter, 100% probability of detection is achieved for threshold values of $1.9dB$ or lower. However, the number of false alarms is high (>50). However, some of these false alarms can be confirmed by eye as false positives as the high resolution captures the tongue-shape and so random pixels assigned to the avalanche class are easily discarded. Some of the false alarms are located on mountain ridges where there are no avalanches expected.
- When a RSO filter is used as post-classification filter at least 3 of 13 debris fields for threshold values of $1.5dB$ and higher are discarded. This could be due to too little detected pixels with an enhanced backscatter within the debris field and are therefore discarded by the filter. However, the number of false alarms is lower than when using a median filter; >20 for a threshold value of $2.8dB$ or lower and 18 and 16 for threshold values of $2.9dB$ and $3dB$, respectively.

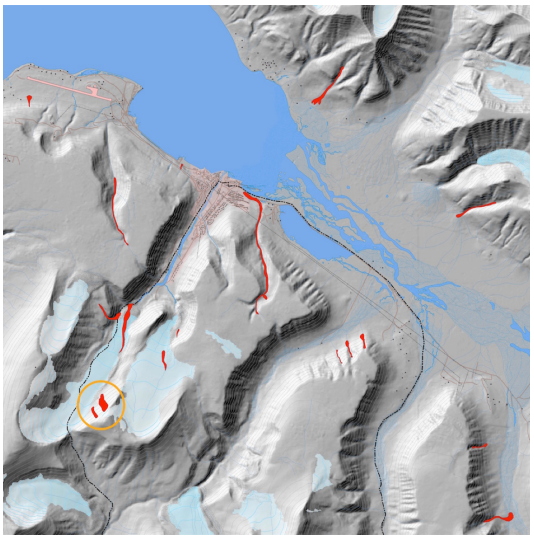

Figure 6.19: Map of area around Longyearbyen on Svalbard, where slush avalanches as noticed on 2013.06.05 by field observations are indicated in red. The slush avalanche also detected by RADARSAT-2 UF mode images is encircled in orange. © *Markus Eckerstorfer*.

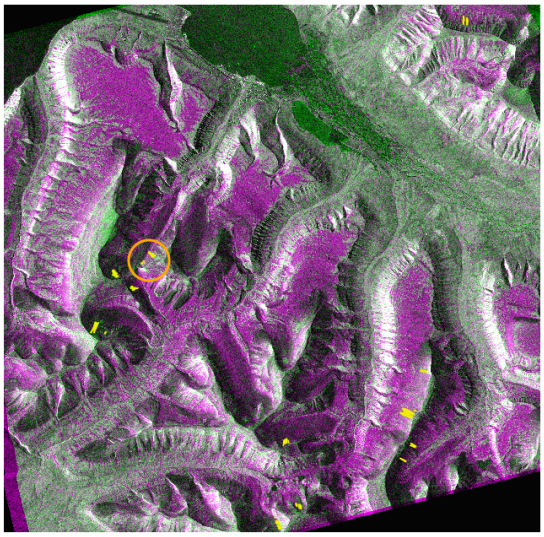

Figure 6.20: RADARSAT-2 UF mode image in RGB with on top in yellow outlined manually detected debris fields. The slush avalanche also detected by Markus Eckerstorfer during field observations on 2013.06.05 is encircled in orange.

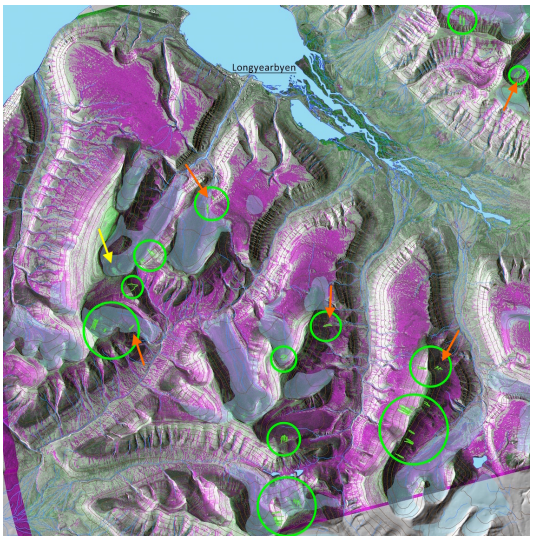

Figure 6.21: RADARSAT-2 UF mode image in RGB in green encircled manually detected avalanches by Markus Eckerstorfer. The orange arrows denote manually detected avalanches detected by Markus Eckerstorfer, but not by manual detection performed in this thesis. The yellow arrow stands for manually detected debris fields detected by manual detection performed during this research project, but not by Markus Eckerstorfer.

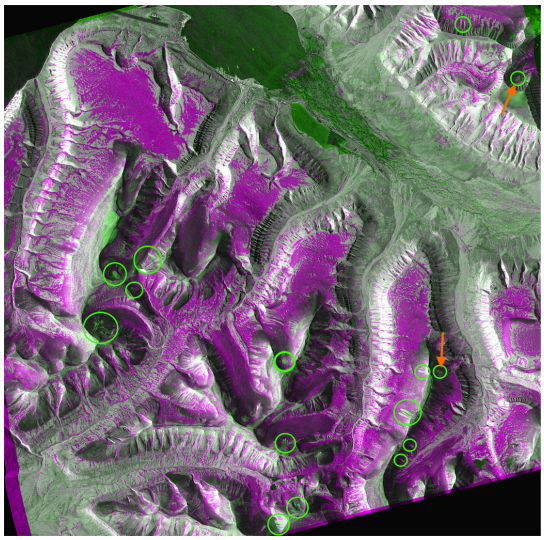

Figure 6.22: RADARSAT-2 UF mode image in RGB with in green encircled manually detected avalanches by Hannah Vickers. The orange arrows denote manually detected avalanches detected by Hannah Vickers, but not by manual detection performed in this thesis. No debris fields were identified by the manual detection performed during this research project and not by Hannah Vickers.

Validation

- The avalanche activity in June is caused by the increased air temperature and precipitation on 2013.06.05.
- The wet snow areas as indicated in the wet snow cover maps from SNAPS around the acquisition date of the avalanche image correspond to the pink areas in the RGB image. Due to the low backscatter of wet snow, it causes pink areas when observed during acquisition of the avalanche image and green areas when observed during acquisition of the reference image.
- Two of the manually detected avalanche debris fields were also noticed during field observations by Markus Eckerstorfer. These were identified as slush avalanches.
- The manual detection performed in this thesis slightly underestimated the number of debris fields compared to the manual detection performed by other avalanche experts. Hannah Vickers identified two more debris fields, while Markus Eckerstorfer even detected five more avalanches.

The avalanche map created from the output of the designed automatic detections methods show the location and extent of avalanche events. Different settings were tested and the results validated. The final designed automatic detection method is specified to the RADARSAT-2 UF mode image in 'VV'-polarisation from 2013.06.10 and 2013.09.14. The optimum configuration for detecting avalanches in these images is using a median filter of 5x5 pixels as post-classification filter after applying a threshold of $1.9dB$. This leads to 100% probability of detection, but also to many false alarms. Some of these false alarms can be eliminated by eye as they are clearly no avalanches due to group size or location. The two designed automatic detection methods are also tested on the Sentinel-1A images to test the usefulness on images with a coarser resolution than the UF images. This will be further explained in the next chapter.

Chapter 7

Avalanches detected in coarse Sentinel-1A SAR images

In this chapter the results and discussion of the designed framework applied to Sentinel-1A images is presented. The outcome of the manual detection together with a quantitative analysis is given in Section 7.1. This analysis is used as input for the automatic detection, which is assessed and validated in Sections 7.2 and 7.3, respectively. Finally, the main findings are listed in Section 7.4.

Although Sentinel-1A Extra Wide swath (EW) mode data is available starting from October 7^{th}, 2014 only a few images are selected that were acquired around the time avalanche activity is expected. The University Centre in Svalbard provides weather data from locations all over Svalbard. One of the meteorological stations is situated on Gruvefjellet nearby Longyearbyen. The air temperature and wind speed from March 2015 at this station are shown in Figure 7.1. Air temperature fluctuations and increased wind speeds cause an increase in avalanche releases. As the air temperature increased to almost 0^oC and the wind speed reached a peak as well, avalanches are expected after March 15^{th}. By analysing the EW mode images - as shown in Appendix B.1 - the starting date of the avalanche cycle can be deduced. All green tongue-shaped features visible in the descending RGB images for which the avalanche image is acquired on March 16^{th} or later are encircled in red. Due to geometric distortions caused by the side looking view of the radar ascending and descending images might capture different avalanche debris fields; as the avalanches are facing different aspects they can be observed in either both the ascending and descending track or in only one of them. Although Sentinel-1A has a beneficial repeat pass of 12 days and acquires images twice per day on Svalbard (an ascending and a descending), the pixel spacing of $40m$ might be challenging for avalanche detection.

7.1 Results of detection

The manual and automatic detections are applied on a descending and an ascending image from the same acquisition date in both 'HH'- and 'HV'-polarisation. The manual and auto-

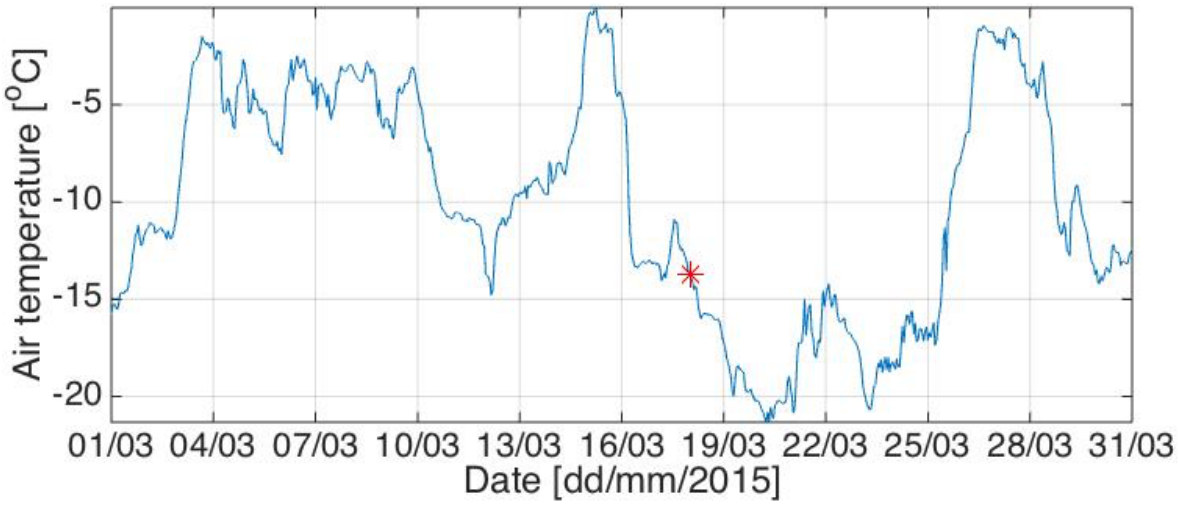

(a) Air temperature

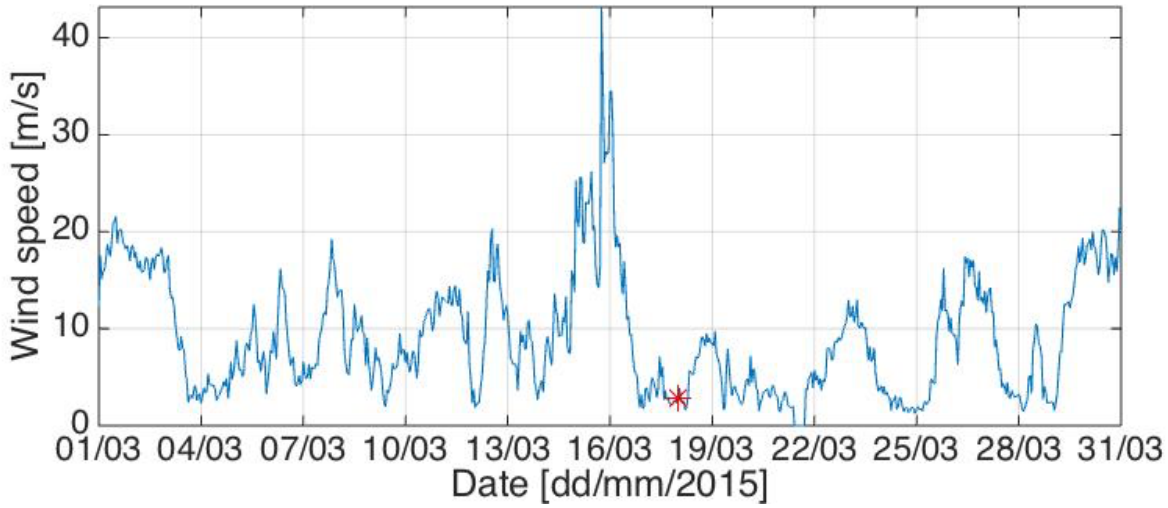

(b) Wind speed

Figure 7.1: Meteorological data from March 2015 at Gruvefjellet on Svalbard. The red asterisk denotes the acquisition date of Sentinel-1A EW mode image from 2015.03.18. Air temperature fluctuations and increased wind speeds cause avalanche events. The debris fields visible in EW mode image *'20150318'* are thus due to weather conditions on March 15^{th}. Data is provided by University Centre in Svalbard.

matic detection is described in Subsections 7.1.1 and 7.1.2, respectively. Also the combination of an avalanche image in 'HH' and 'HV' polarisation is tested. The selected avalanche images are from 2015.03.18 and the reference images are from 2015.03.06. Thus, the RGB images are created as follows: *[RGB]=[20150306, 20150318, 20150306]*. The reason for choosing these images is that they are two repeat passes and avalanche activity is clearly visible. Also these images show a contrast between the green tongue-shaped features and the surrounding (unperturbed) snow.

Table 7.1: Size of manually detected avalanches as identified in Sentinel-1A EW mode images in RGB created from *'20150318'* and reference image *'20150306'*. Also given is total number of detections per beam mode and the average length and width of the detected avalanches and whether the debris fields are visible in the descending (Desc.) and ascending (Asc.) image in either 'HV'- and 'HH'-polarisation.

#	Aspect	Length [m]	Width [m]	Desc. 'HV'	Desc. 'HH'	Asc. 'HV'	Asc. 'HH'
1	W	270	240	Y	N	N	N
2	NW	300-570	180-190	Y	Y	Y	Y
3	W	670	180	Y	Y	Y	Y
4	E	390	200	Y	N	Y	Y
5	NW	650	120	Y	Y	N	N
6	SE	200-500	200-250	Y	N	N	N
7	N	290-480	120-230	Y	Y	Y	Y
Total				7	4	4	4
Range		200-670	120-250				

7.1.1 Manual detection

The results of the manual detection applied on the descending image pair in 'HV' polarisation is shown in Figure 7.2. The bright areas in this image are most likely gullies as they show little change between avalanche *'20150318'* and reference image *'20150306'*. The manually detected avalanches are outlined in yellow on top of this image. The reason for only presenting the 'HV'-polarised images here is that more avalanche debris fields are manually detected using this polarisation. This could be due to the fact that 'HV'-polarisation is more sensitive to surfaces with multiple scatterers as stated in Subsection 3.1.4. However, to compare the difference in the use of polarisation mode the automatic detection is also applied on the 'HH'-polarised images and the results corresponding are presented in this Subsection. The manual detection of the ascending image is presented in Appendix B.2. It can be seen that less debris fields are identified in the ascending image than in the descending image. This is also discussed in the next paragraph.

Evaluation of the descending/ascending track in 'HV'/'HH'-polarisation

To compare the descending and the ascending images in both 'HV'- and 'HH'-polarisation an overview is created with all manually detected avalanches - see Table 7.1. The map of the slope aspects within Nordenskiöld Land is shown in Figure 7.3, which is created using the Digital Elevation Model (DEM). In this table the aspect of the detected avalanches, the size and in which image the debris fields are visible for the eye are shown. It can be seen that the descending image in 'HV'-polarisation captured the most debris fields. However, the automatic detection is applied on all images to analyse the effect of imaging geometry and the polarisation mode. Most of the avalanches occurred on N-/NW-/W-facing slopes, which will be validated in Section 7.3.

Quantitative analysis and discussion

To perform a quantitative analysis on the manually detected avalanches in the images, a mask

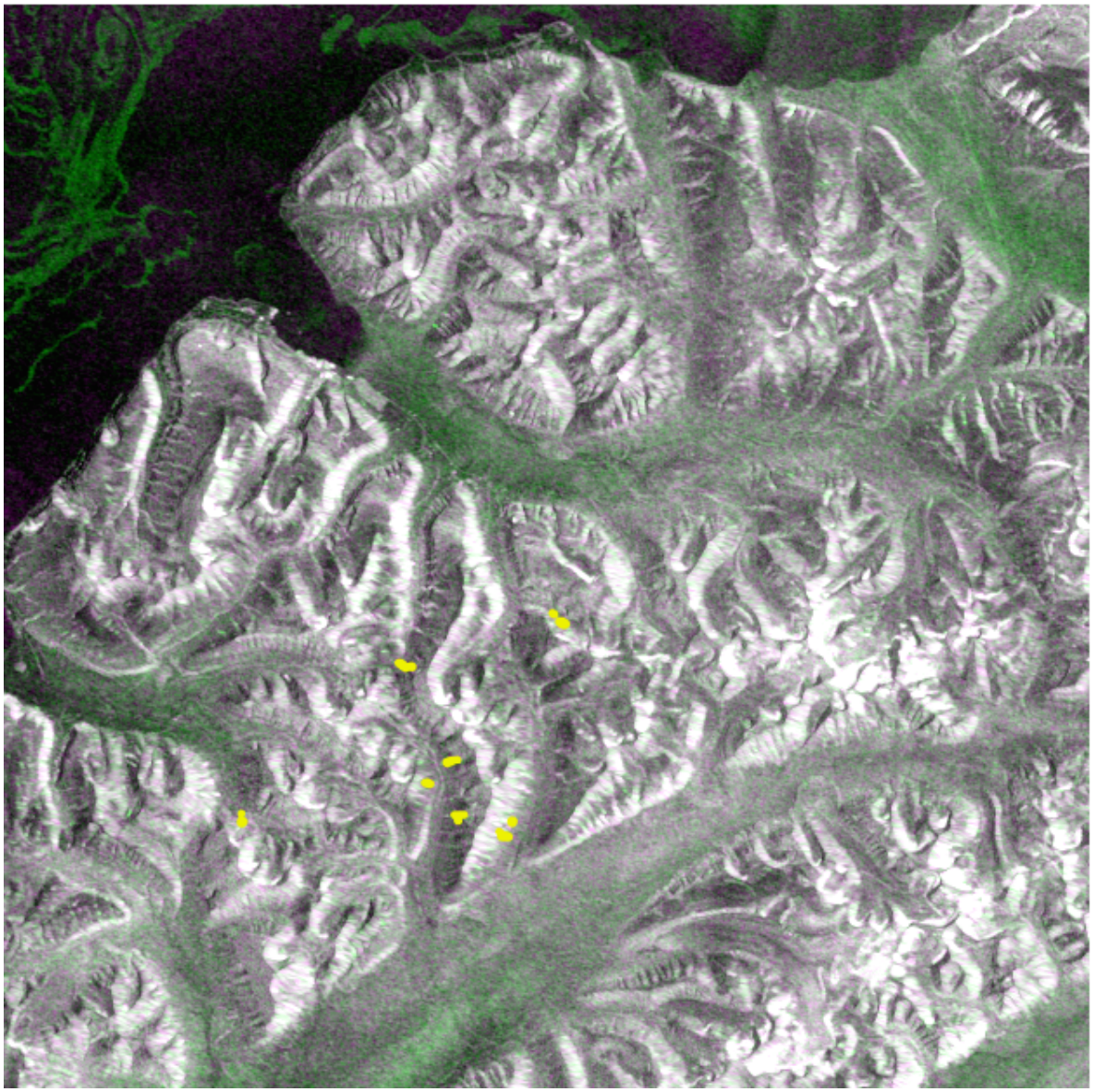

Figure 7.2: Descending Sentinel-1A EW mode images in RGB created by an avalanche image from 2015.03.18 and a reference image from 2015.03.06, both in 'HV'-polarisation. The manually detected debris fields are outlined in yellow.

is created to either clip out or mask out the detected avalanches. As explained in Chapter 4, these masks can then be used to obtain statistics on the difference in backscatter coefficient inside and outside of the manually detected avalanches. Histograms of all six combinations (using the ascending and descending track in both 'HH'- and 'HV'-polarisation) are computed and shown in Figure 7.6. The cross-sections between the two histograms for the 'HV'-polarised images lies between $3dB$ and $4dB$, while for the 'HH'-polarised images they cross around $2dB$. Thus, cross-polarisation captures a higher backscatter of debris fields compared to the co-polarisation mode. Different polarisation modes require different threshold values. This is also tested during automatic detection of the images - see Subsection 7.1.2. When only

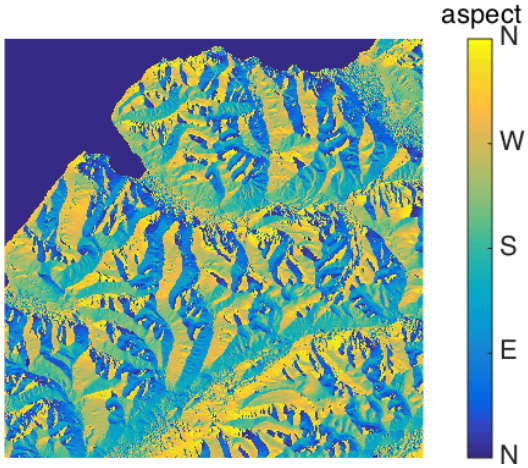

Figure 7.3: Map showing aspect of all mountain slopes within area covered by Sentinel-1A EW mode images: Nordenskiöld Land on Svalbard. The slop aspect is determined using the DEM presented in Section 5.2 and used to determine slope aspect at location of debris fields.

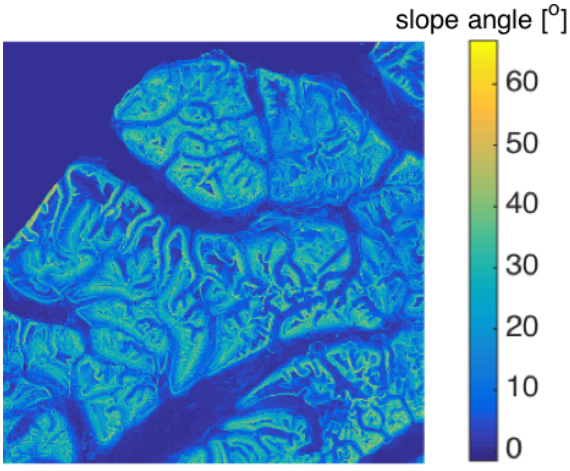

Figure 7.4: Map showing slope angle of mountains within area covered by Sentinel-1A EW mode images: Nordenskiöld Land on Svalbard. This map is determined using the DEM presented in Section 5.2 and used for analysis of slope angles where debris fields are located.

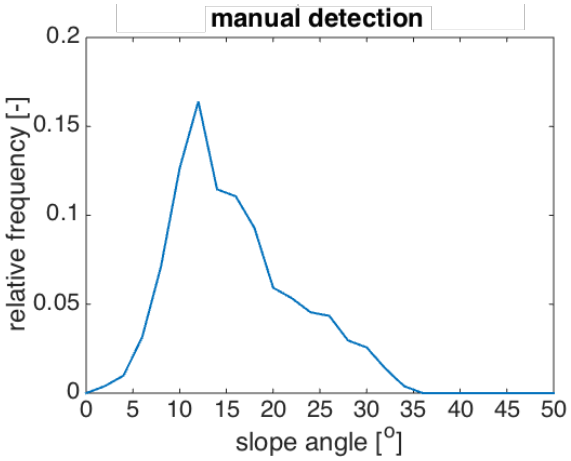

Figure 7.5: Histogram of slope angles at locations of manually detected avalanches in Sentinel-1A EW mode images. The debris fields are detected on slope angles between 10^o and 45^o. These values are consistent with theory (McClung and Schaerer, 2011). The lower values are probably from the run-out zone of the avalanches.

the avalanche image *'20150318'* is taken and a RGB image is created using the different polarisations in the channels, change detection by thresholding will not be very suitable as the histograms overlap too much.

Figure 7.4 shows the slope angle map of the area covered by the EW mode images. The slope angles at the location of the manually detected debris fields are determined using this map. The histogram in Figure 7.5 shows that the slope angles where avalanches are located varies between 0^o and 35^o. This is according to what is expected as stated in Section 2.1. The slope angle below 25^o are probably in the run-out zones of the avalanches as slab avalanches are generally triggered on slopes with an angle between 25^o and 55^o.

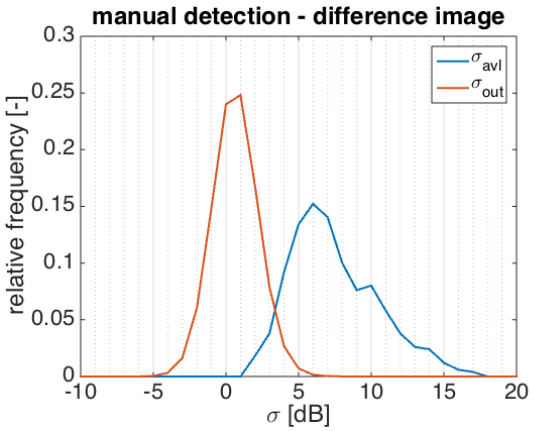

(a) descending - 'HV'

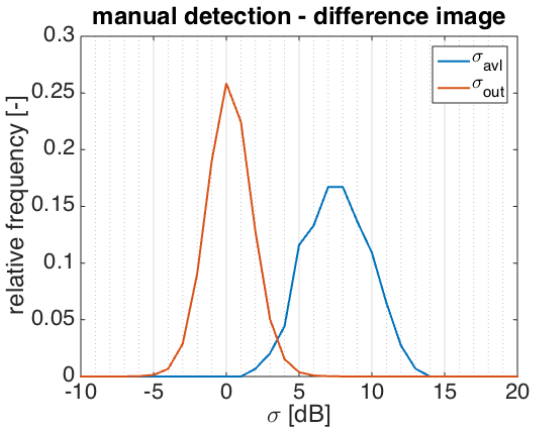

(b) ascending - 'HV'

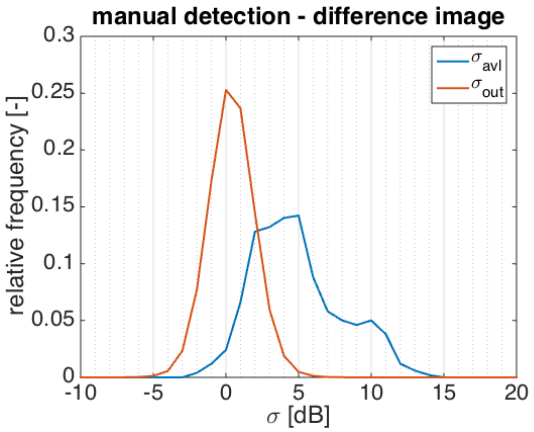

(c) descending - 'HH'

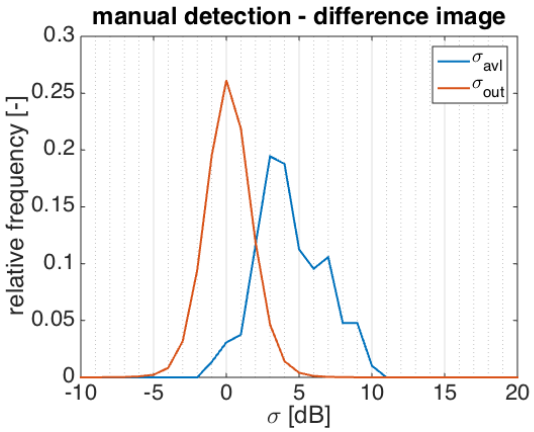

(d) ascending - 'HH'

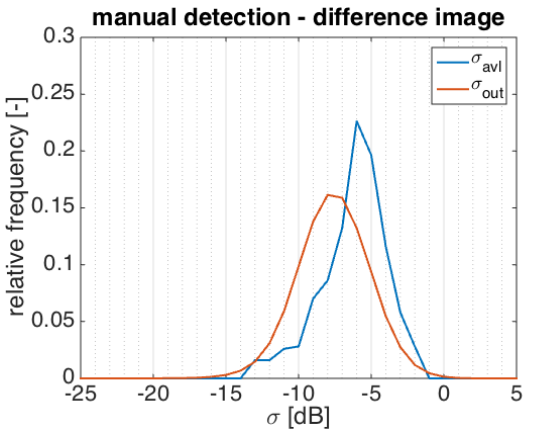

(e) descending - 'HV'-'HH'

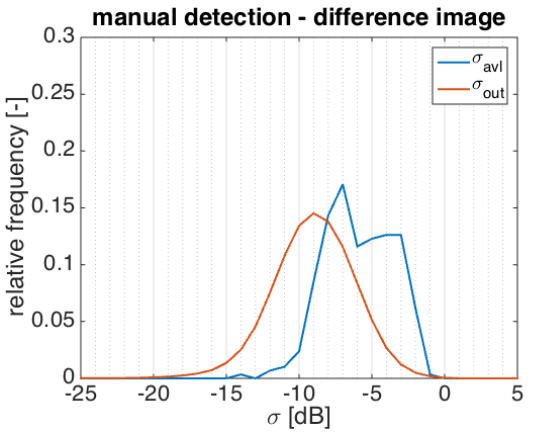

(f) ascending - 'HV'-'HH'

Figure 7.6: Histograms of backscatter coefficients inside σ_{avl} and outside σ_{out} of manually detected avalanches in descending and ascending Sentinel-1A EW mode images *'20150318'* and *'20150306'* in 'HH'- or 'HV'-polarisation. The lower two histograms represent the difference between 'HV'- and 'HH'-polarisation of same descending (left) and ascending (right) image. For all histogram the backscatter coefficient within manually detected avalanches of the avalanche image is higher compared to the reference image. For the 'HV'-polarised images the crossing point between the two histograms lies around 3-4dB, while for 'HH'-polarised images the crossing point lies around 2dB. When using a combination of 'HV'- and 'HH'-polarised images the histograms overlap too much to be able to apply thresholding.

7.1.2 Automatic detection

Following the automatic detection steps as presented in Chapter 4, first a median filter of 5x5 pixels is applied on *20150318* and reference image *20150306* for speckle reduction. Hereafter, areas not prone to avalanches are masked out as well as layover and shadow areas. The thresholding of the automatic detection is based on analysing the histograms of the difference image as shown in Figure 7.6. For the 'HV'-polarisation images threshold values between 3 and 4dB with steps of 0.1dB are applied on the difference image, while for the 'HH'-polarised images a threshold between 2 and 3dB is used. As applying a median filter as post-classification filter led to too many false alarms, only the classification by a Remove Small Objects (RSO) filter is used and presented here.

Post-classification method 2: RSO filter

The size of the RSO filter is based on the smallest single debris field manually detected; taking the pixel spacing into account as well, all pixel groups smaller than 50 are eliminated. The outcome of the automatic detection by thresholding and RSO filter are presented on top of the avalanche image *'20150318'*. For the results of the complete range of applied threshold values see Appendices B.3 and B.5 for cross-polarisation and Appendices B.4 and B.6 for co-polarisation. For the 'HV'-polarisation images a threshold value of 3.4-3.5dB is the transition range where some of the manually detected avalanches are failed to be detected by the automatic detection. Therefore these are also shown here, together with the outcome of using a threshold value of 3 and 4dB. Figures 7.7 and 7.8 present the avalanche maps for respectively the descending and ascending image. The debris fields that are also detected manually are encircled in red. The reason for using the 'HV'-polarised images instead of the 'HH'-polarised images is that the latter one resulted in more false alarms and a lower probability of detection of the debris fields. This is further analysed in the next Subsection.

7.2 Discussion on results of the automatic detection

Table 7.2 gives an overview of the number of correct and false identified avalanche debris fields by the automatic detection compared to the manual detection. This table is deduced from the figures in Appendices B.3 to B.6. The manual detection identified seven debris fields in the descending image and four in the ascending image. It can be seen that increasing the threshold lowers the false alarms, but also lowers the number of correct identified avalanches. Since the Synthetic Aperture Radar (SAR) system is right-looking, the descending and ascending tracks have a different view on the mountains and thus on the avalanche activity. In this case the ascending image captured less avalanches compared to the descending image, and all four visible in the former image are also visible in the latter image.

By analysing the results between the use of the different thresholds it can be seen that when using a threshold value of 3.4dB on the descending image in 'HV'-polarisation all seven identified debris fields are captured, together with 13 false alarms. Increasing the threshold value leads to failed detection of some avalanches. The table also shows that when using the 'HH'-polarisation image, especially in descending track, less avalanches are identified compared to the manual detection.

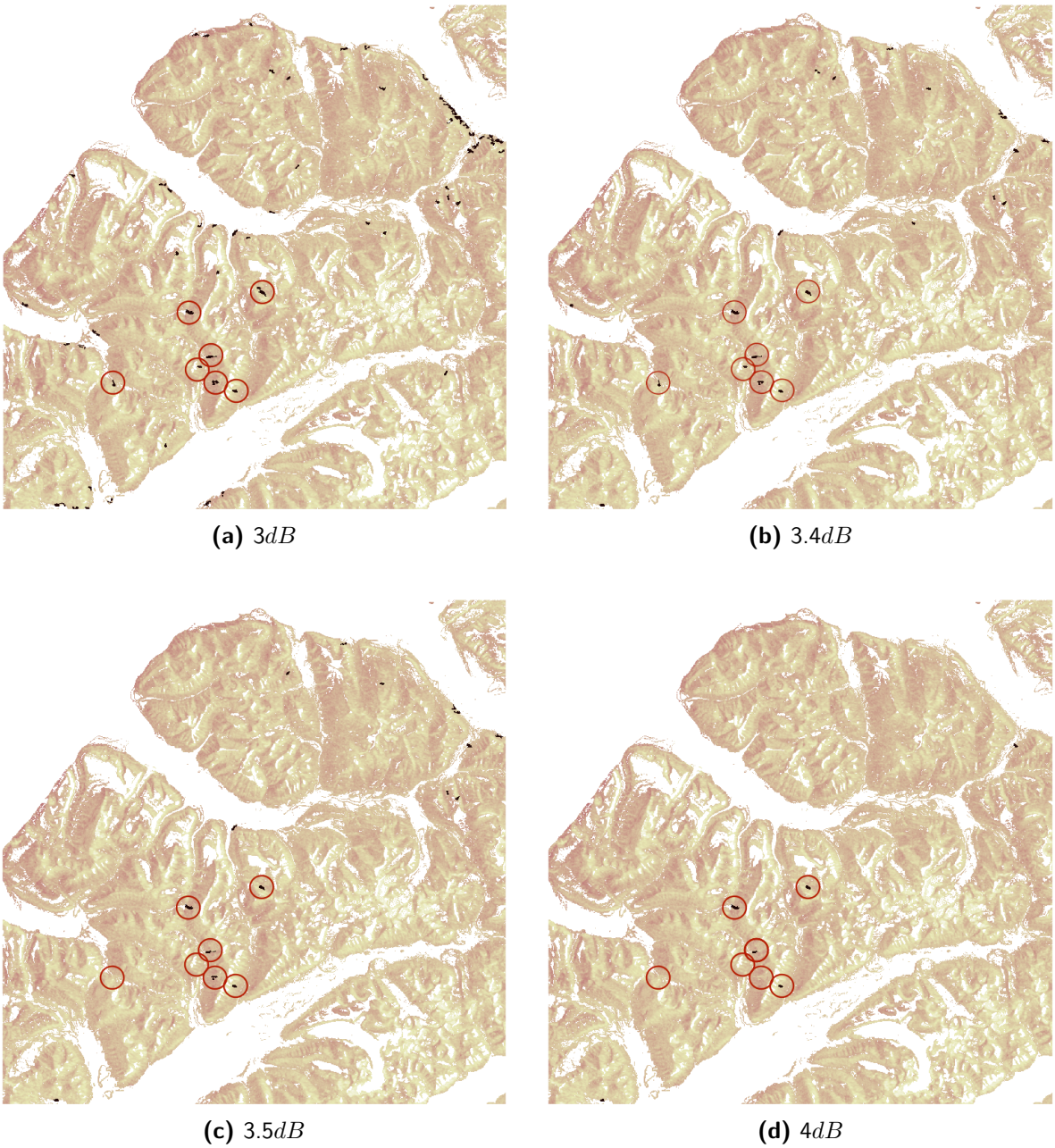

(a) $3dB$ **(b)** $3.4dB$

(c) $3.5dB$ **(d)** $4dB$

Figure 7.7: Results of automatic detection method using post-classification filter 2: RSO filter and threshold values $3dB$, $3.4dB$, $3.5dB$ and $4dB$. The method is applied on descending Sentinel-1A EW difference image from *'20150318'* and *'20150306'* in 'HV'-polarisation. Manually detected debris fields are encircled in red. The black areas outside the blue and red circles are false alarms. Increasing the threshold value leads to less false alarms, but also to a decrease of probability of detection, i.e. the number of black areas decreases both inside and outside of red circles.

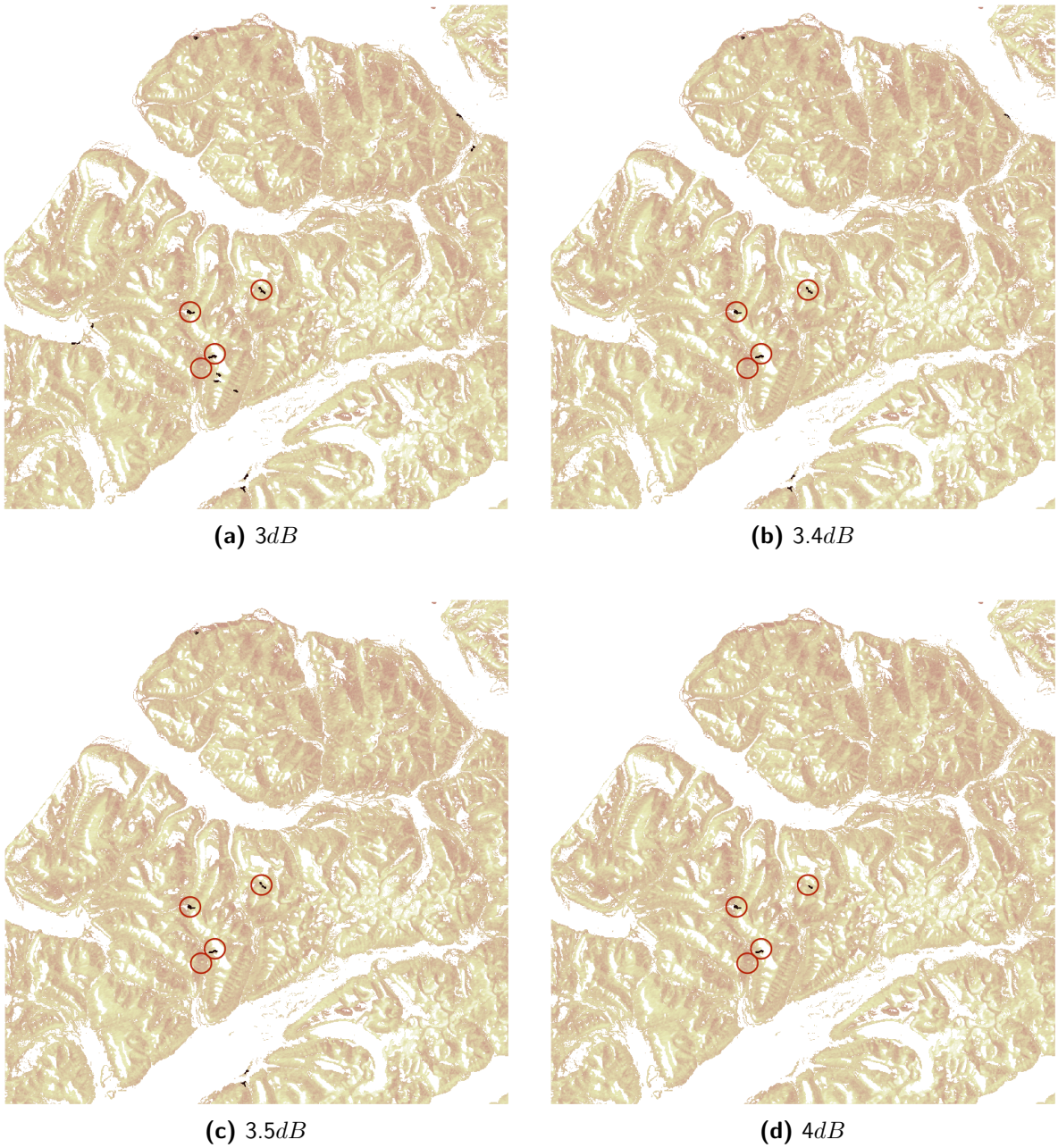

(a) $3dB$ **(b)** $3.4dB$

(c) $3.5dB$ **(d)** $4dB$

Figure 7.8: Results of automatic detection method using post-classification filter 2: RSO filter and threshold values $3dB$, $3.4dB$, $3.5dB$ and $4dB$. The method is applied on ascending Sentinel-1A EW difference image from *'20150318'* and *'20150306'* in 'HV'-polarisation. Manually detected debris fields are encircled in red. The black areas outside the blue and red circles are false alarms. Increasing the threshold value leads to less false alarms, but also a decrease of probability of detection, i.e. the number of black areas decreases both inside and outside of red circles.

Table 7.2: Number of correct and false identified debris fields per threshold value for post-classification 2: RSO filter applied on Sentinel-1A EW mode images. In the descending image a total of seven debris fields were detected manually and in the ascending image only four. For all images an increase in threshold value cause a decrease in number of false alarms (FP) along with a decrease in number of correct identified debris fields (TP) and thus the probability of detection (TPR). Detection of descending 'HV'-polarised images result in a TPR of 100% when using threshold values of 2.4dB or lower. This is the only image for which all manually detected debris fields are automatically detected as well and still gives an acceptable amount of false alarms.

Threshold $[dB]$	TP $[-]$	TPR $[\%]$	FP $[-]$
3	7	100	>20
3.1	7	100	>20
3.2	7	100	>20
3.3	7	100	>20
3.4	7	100	13
3.5	5	71	10
3.6	5	71	8
3.7	5	71	6
3.8	5	71	4
3.9	5	71	3
4	4	57	2

(a) descending - 'HV'

Threshold $[dB]$	TP $[-]$	TPR $[\%]$	FP $[-]$
3	3	75	10
3.1	3	75	9
3.2	3	75	6
3.3	3	75	5
3.4	3	75	4
3.5	3	75	3
3.6	3	75	2
3.7	3	75	1
3.8	3	75	1
3.9	3	75	-
4	3	75	-

(b) ascending - 'HV'

Threshold $[dB]$	TP $[-]$	TPR $[\%]$	FP $[-]$
2	6	86	>20
2.1	6	86	>20
2.2	6	86	>20
2.3	6	86	>20
2.4	4	57	>20
2.5	4	57	>20
2.6	4	57	>20
2.7	4	57	>20
2.8	4	57	>20
2.9	3	43	>20
3	3	43	>10

(c) descending - 'HH'

Threshold $[dB]$	TP $[-]$	TPR $[\%]$	FP $[-]$
2	3	75	>20
2.1	3	75	>20
2.2	3	75	>20
2.3	3	75	>20
2.4	3	75	>20
2.5	3	75	>20
2.6	3	75	>20
2.7	3	75	>20
2.8	3	75	17
2.9	3	75	13
3	2	50	9

(d) ascending - 'HH'

7.3 Validation

As the images are obtained in March 2015 it is expected that the detected debris fields originate from wet snow avalanches due to the higher air temperatures in this season causing melt. Figure 7.9 shows a descending and an ascending image obtained on March 14^{th} in the morning (*'20150314'*) and March 16^{th} in the afternoon (*'20150316'*), respectively. The avalanche cycle started between the acquisition time of these two images as the latter one shows debris fields not visible in the former image. For clarity, the debris fields identified in the image *'20150316'* are encircled in green and laid over *'20150314'*. However, it is hard to say with confidence that the manual detection is correctly performed. Due to the coarse resolution of the images, the avalanches do not appear in a tongue-shape but just as enhanced pixels. Thus validation of these detected debris fields is important. Meteorological data, field observations and multispectral images are used for the validation.

Meteorological data

The air temperature and wind speed presented in Figure 7.1 are obtained at Gruvefjellet, which is located between Sukkertoppen and Sarkofagen - see Figure 5.3. Both the air temperature and wind speed show an increase around March 15^{th}. These conditions caused the avalanche cycles as observed in the Sentinel-1A images. As stated in the Chapter 2 prevailing wind direction and strong winds can trigger cornices to fall releasing slab avalanches. Table 7.1 showed that most debris fields are located on North- to West-facing slopes, which is consistent with the strong winds mainly coming from the SE - see Figure 7.10.

Multispectral optical images

Landsat-8 images acquired on March 17^{th} and 18^{th} are downloaded from earthexplorer.usgs.gov. As explained in Subsection 5.4.1 this website provides 'Natural Color' images and 'Thermal' images, obtained by Operational Land Imager (OLI) and Thermal Infrared Sensor (TIRS). These images have a spatial resolution of $30m$ and $100m$ respectively. This low spatial resolution in combination with the low contrast between the avalanche and surrounding unperturbed snow makes it hard to distinguish the debris fields. Therefore unfortunately none of the avalanches is visible in these optical images.

Field observations

As explained in Chapter 2 a slab avalanche is a cohesive slab on top of a sliding surface or weak layers that gets released. Thus, information on the snow layers and properties is helpful in determining the stability of the snowpack. The snow profiles obtained on February 20^{th} and 21^{th} are given in Figures 5.4 and 5.5. These snow profiles are not representative for the complete area within Nordenskiöld Land as they were obtained close to Longyearbyen where the snowpack is different from more land inwards. They are also obtained a month before the avalanche events. However, the first profile shows a thick depth hoar layer at the bottom that is characteristic for Svalbard. In case the depth hoar layer collapses, avalanches can be released - see Section 2.2. Also found in both profiles are icy layers. Since the ice is smooth these layers act as sliding planes for the cohesive slabs. Although no avalanches were observed at the location of these snow profiles they do confirm that weak layers are present in the snow pack.

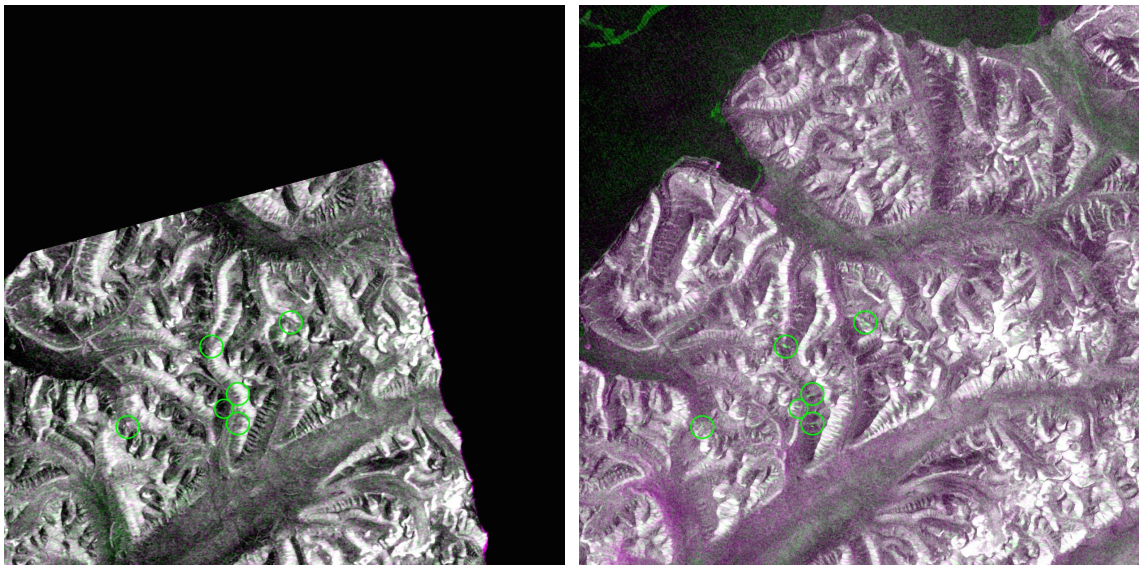

(a) *'20150302'* and *'20150314'* "

(b) *'20150304'* and *'20150316'*

Figure 7.9: Sentinel-1A EW mode RGB images in 'HH'-polarisation covering Nordenskiöld Land on Svalbard from before and after avalanche cycle. The descending images in RGB on the left are acquired on 2015.03.02 and 2015.03.14 in the morning and the ascending image in RGB are obtained two days later on 2015.03.04 and 2015.03.16 in the afternoon.

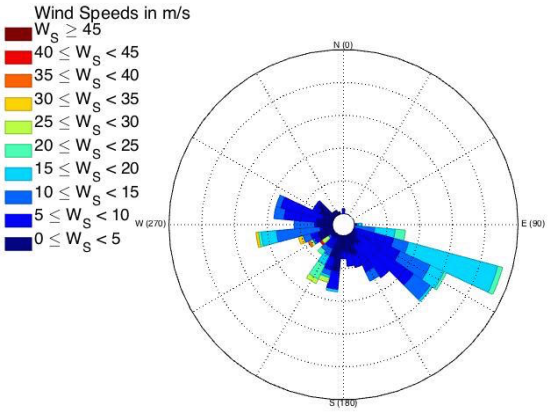

Figure 7.10: Wind- speed and direction observed in March 2015 at Gruvefjellet on Svalbard. It can be seen that Svalbard experiences a prevailing SE wind direction, which results in most avalanches to be located on NW-facing slopes. Data is provided by University Centre in Svalbard.

The black filled rectangles in the snow profiles stand for ice layers. It can be seen both snow profiles contain at least one icy layer. This is in accordance with what is expected from a 'High Arctic Maritime Snow Climate' (Eckerstorfer and Christiansen, 2011b). The red line in the snow profile denotes the temperature throughout the snowpack. As Svalbard is characterised by permafrost, the ground temperature will always be below zero degrees Celsius.

Snow profile #1 shows a depth hoar layer of $24cm$ and could potentially facilitate the occurrence of an avalanche. Note that the second snow pit was not dug until the ground, but to a depth of $110cm$ where an icy layer was found. No depth hoar was noted in this snow profile. However, this could be existent deeper in the snowpack beneath the icy layer.

Figure 7.11: Photograph of a slab avalanche at Gangskaret on Svalbard. This avalanche is also visible in the descending and ascending Sentinel-1A EW mode images from 2015.03.18. 17 March 2015, © *Chris Borstadt*.

One of the bigger avalanches at Gangskaret observed by the satellite has also been reported on the crowd-sourcing website regObs.no. The photograph shown in Figure 7.11 is taken by Chris Borstadt. Unfortunately no other field observations were found for the other six detected debris fields. However, as most of them occurred on NW-facing slopes, which is consistent with the pattern as observed at Svalbard, the outcome of the manual detection seems reasonable. Also the results have been discussed with other avalanche experts via personal communication.

7.4 Main findings

Listed below are the main findings of the comparison of the beam modes and the analysis of the manual and automatic detection.

Detected debris fields

- Svalbard experienced a prevailing wind direction from the SE in March causing cornice formation overhanging the NW-facing slopes. In cornices fall they cause slab avalanches and therefore most of the detected avalanches occurred on NW-facing slopes.
- Slightly different avalanches are detected by the descending and ascending images due to the imaging geometry of both tracks.
- 'HV'-polarisation seems more sensitive to avalanche debris fields than 'HH'-polarisation as it captures a higher backscatter for these areas resulting in a bigger difference between the avalanche image and the reference image. 'HV'-polarisation is more sensitive to

surfaces with multiple scatters, whereas 'HH' is sensitive to objects orientated in the same direction as the incoming radiation.
- Combining 'HV'- and 'HV'-polarisation from the same acquisition date to create an RGB image is not useful as the difference between the two polarisation modes is too small for automatic detection.
- When a RSO filter is used as post-classification filter in combination with a threshold of $3.4dB$, 100% of the debris fields were detected. The number of false alarms was 13 compared to 7 detected avalanches. Due to the coarse resolution of the image the extent is not captured as well as when using the RADARSAT-2 Ultra Fine (UF) mode image. However, Sentinel-1A has a preferred temporal sampling as it acquires images twice per day on Svalbard.

Validation

- Air temperature fluctuations and increased wind speeds caused the avalanche events after March 15^{th}, 2015.
- The detected avalanches are not visible in the Landsat-8 images. This could be due to a low contrast between the debris field and the surrounding unperturbed snow or the low spatial resolution.
- The slab avalanche at Gangskaret is photographed by Chris Borstadt, so this avalanche is validated. To validate the other identified avalanche more ground-truth data is needed.
- All of the manually detected avalanches are also found by the automatic detection. However, the tongue-shape is not distinguishable due to the coarse resolution. On the other side this low spatial resolution also causes little false alarms.

The automatic detection method as defined in this chapter is specified to the Sentinel-1A EW mode images from 2015.03.18 and 2015.03.06. The best result is obtained when using the descending image in 'HV'-polarisation as input, where best means 100% probability of detection and as little false alarms as possible. The output of the designed automatic detection method using a RSO filter is visualised on an avalanche map. When using a threshold of $3.4dB$ all seven manually detected debris fields were detected automatically as well, together with 13 false alarms. The optimum filter and threshold value vary from the automatic detection method for the RADARSAT-2 images in UF mode. This is due to the different characteristics of the satellites and images; they have both a different pixel spacing and polarisation mode. Although the avalanche activity in time can closely be monitored using Sentinel-1A images due to the high temporal resolution, the extent of the debris fields is not captured clearly due to the coarse resolution of the images.

By combining multiple images a tracking system can be designed to check the avalanche activity over time in consecutive SAR images. However, to create a more general automatic detection method, the designed method should be tested on additional images.

Chapter 8

Conclusions and recommendations

Avalanches form a threat to people travelling in mountainous regions as well as for infrastructure and buildings. Avalanche research is needed to get a more profound understanding of the avalanche activity in space and time, which is of great value for avalanche warning services. Just as for other regions, the infrastructure and people living and travelling in and around Svalbard's main settlement area Nordenskiöld Land are directly affected by both naturally and artificially triggered avalanches.

In this thesis a method to automatically detect avalanche debris fields in Synthetic Aperture Radar (SAR) images is designed and tested on both RADARSAT-2 Ultra Fine (UF) mode images and the Sentinel-1A Extra Wide swath (EW) mode images. RADARSAT-2 could obtain images in different geometries daily over Svalbard, but is very costly. The RADARSAT-2 images are acquired with high spatial resolution (3m) and low temporal resolution (repeat period of 24 days), whereas Sentinel-1A obtains images with low spatial resolution (40m) in EW mode, high temporal resolution (twice per day) and a repeat period of 12 days. The main goal of this research project has been to optimise avalanche detection in SAR images and find out to what extent automatic detection is possible.

The key findings obtained during the research project are presented in Section 8.1. First the subquestions are dealt with, followed by the main research question. During execution of the project, the focus has been on achieving the set goals and answering the research question and subquestions as introduced in Chapter 1. However, along the way challenges emerged, followed by more questions. All recommendations are based on these questions and listed in Section 8.2.

8.1 Key findings

To be able to answer the research question, first the subquestions need to be discussed. The questions as presented in Section 1.1.2 are answered per item and listed below per subject.

Available methods to detect avalanches

What kind of methods for mapping and monitoring of avalanches are currently available? And what are their advantages and disadvantages?
Avalanche research, or the monitoring of avalanche activity in space and time, improves the understanding of avalanche formation. The available monitoring techniques can be divided by platforms, i.e. ground-based, airborne or spaceborne, and by imaging technique, i.e. optical or radar. The main disadvantage of using optical sensors is their weather- and light dependency. Radar signals, on the other hand, are able to penetrate through clouds and are not restricted by (day)light. Ground-based radars have the advantage of obtaining images with high temporal resolution and of being portable. They are, however, not convenient to cover larger areas. Sensors placed on airborne or spaceborne platform are able to obtain high resolution images over a large (remote) areas. However, acquiring images by airplanes or Unmanned Airborne Vehicle (UAV)s is often very costly.

Which technique suits best for avalanche detection on Svalbard? And why?
Svalbard experiences almost four months of polar night per year. Most avalanches occur during the dark season and therefore the light independency of the sensor is important. Combining this with the fact that many regions of the mountainous archipelago are quite remote, satellite-borne SAR is the most applicable technique to use in this area.

How would automatic detection of avalanches in SAR images be helpful for avalanche research?
Manual detection of avalanches in SAR images has already been proven to be successful (Eckerstorfer et al., 2014b). However, this can be a time-consuming task when dealing with large avalanche cycles when there are up to even 400 debris fields located in a single image. Sentinel-1A provides data twice per day on Svalbard, i.e. an ascending and a descending image. Therefore the occurrence of avalanches can closely be monitored. The avalanche activity can then be passed to avalanche warning services and the general public.

Automatic detection of debris fields in SAR images

How can avalanches be automatically detected in SAR images?
As avalanche debris has an increased surface roughness and snow density compared to the surrounding unperturbed snow it causes a higher backscatter signal. Therefore the debris fields appear bright in SAR images. The backscatter coefficient of the debris fields can also be compared to the backscatter coefficient from a reference image. This reference image should be obtained during dry snow conditions or during a snow-free summer. The difference in backscatter coefficient between the two images is determined by subtracting the reference image from the avalanche image. By applying a threshold value on the difference image the debris fields are successfully located. However, their also exists areas where the difference between avalanche and reference image is above the threshold value, but are noise instead of debris fields. These pixels are false alarms and need to be eliminated by a filter.

Is it possible to detect avalanches automatically in RADARSAT-2 UF mode images having a pixel spacing of 3m? And in Sentinel-1A EW mode images having a pixel spacing of 40m?
Automatic detection of avalanches is possible using either RADARSAT-2 in UF mode or

Sentinel-1A in EW mode. Not only the location of the avalanches is detected, but their extent is captured as well. However, there is a difference in the detectability of the extent between the satellites because of their different pixel spacing. In the fine RADARSAT-2 images, the detected pixels have a clear tongue-shape which is consistent with the shape of avalanche debris. The Sentinel-1A images, on the other hand, does not show the outline of the debris fields due to the coarse resolution. More details on the detectability is given in the next paragraph.

What are the conditions/limitations of the method(s)?
Due to the signal characteristics of C-band radar and the snow properties mostly wet snow avalanches are detected. In case the reference image is acquired during wet snow conditions the detection is more difficult as the difference in backscatter between the debris field and the reference image is smaller. Dealing with wet snow in either the avalanche or reference image is a complication as identified in this thesis but further analysis is not within the scope of the project. There is also a limit on the size of the detected avalanches. For the RADARSAT-2 images the debris fields had a range in length of 100-450m and in width of 10-70m, while for the Sentinel-1A images they varied between 200-670m in length and 120-250m width. This dissimilarity is due to the difference in pixel spacing. In case of the Sentinel-1A images debris fields close to each other get captured within the same resolution cell resulting in a larger, wrongly measured width. The coarse resolution also causes the minimum size of the detected avalanches to be bigger than for the fine RADARSAT-2 images.

Validation of automatically detected avalanches

What is the probability of detection of avalanche debris fields by the designed automatic detection method(s)? And what is the difference between RADARSAT-2 and Sentinel-1A?
Two different post-classification filters were tested: a median filter and a Remove Small Objects (RSO) filter. The median filter eliminates outliers by calculating for every pixel the median of the neighbouring pixels. The RSO filter removes small groups of pixels which are smaller or larger than the expected size of avalanches. Threshold values between 1.5dB and 3dB with steps of 0.1dB were chosen based on the quantitative analysis of the manual detection. The best output would be when all debris fields are correctly detected and there are no pixels falsely identified as avalanche. Thus the optimum is a trade-off between probability of detection of the avalanches and the number of false alarms.

For the RADARSAT-2 images, the median filter gave an output of 100% and 62% detectability of the 13 debris fields for a threshold of 1.5dB and 3dB respectively. However, due to the fine resolution of the images the detection leads to many false alarms as well. Besides the 13 manually detected avalanches, over 50 pixel groups of fake debris fields were located, which is more than four times the number of manually detected avalanches. For the RSO filter the number of false alarms was lower, but at the expense of probability of detection. For a threshold of 1.5dB the detectability was 77% and >20 false alarms were identified, while for a threshold of 3dB the probability was 54% and only 16 groups of pixels were falsely detected.

The post-classification filter using a median filter resulted in too many false alarms when applied on the Sentinel-1A images. Therefore the method has not been used in further analysis. The RSO filter, on the other hand, gave an output of 100% and %57 detectability of the seven manually detected avalanches for a threshold value of 2dB and 3dB respectively

for the descending image in 'HV'-polarisation. Due to the coarse resolution of the images the number of false alarms is also significantly lower; >20 and only 2 false alarms for $2dB$ and $3dB$, respectively. The transition from 100% detectability to 71% lies between $3.4dB$ and $3.5dB$. The number of false alarms is 13 and 10, respectively. A threshold value of $3.4dB$ in combination with a RSO filter applied on the descending Sentinel-1A images in 'HV'-polarisation results in the highest probability of detection. Also little over twice as many false alarms as correct identified debris fields were detected, which seem an acceptable amount compared to all other results.

How can the results be assessed and validated?
The automatically detected avalanches can be assessed by indicating the manually detected avalanches on the avalanche map created from the automatic detection. Both methods are compared by counting the number of detected debris fields and the number of false alarms. The manual detection is assumed to be true and can be validated by letting other avalanche experts perform a manual detection on the same image as well.

Crowd-sourcing websites become more popular and collect field observations, such as snow profiles, stability test results and photographs of avalanche activity. These websites are of great use for validation of detected avalanches. Photographs can proof avalanche activity and results of stability tests can support the probability of avalanches by stating the instability of the snow pack.

Multispectral optical images could be useful in case of clear sky conditions. However, the low spatial resolution in combination with the low optical contrast between the avalanche and the surrounding unperturbed snow make it hard to distinguish debris fields.

Conclusion on main research question

To what extent is automatic detection of snow avalanches possible from Synthetic Aperture Radar amplitude data?
RADARSAT-2 images in UF mode captured both the location and extent of debris fields, while in ScanSAR Narrow (SCNA) and ScanSAR Wide (SCWA) mode image only an enhanced backscatter was observed. The debris fields were not distinguishable in these latter two imaging modes due to their coarse resolution, i.e. their pixel spacing is $50m$ and $100m$, respectively. The UF mode image has a pixel spacing of $3m$, which is thus sufficient enough for detecting both the extent and location of avalanches. For the automatic detection different filters and threshold values were tested. The automatic detection method using a median filter applied on the ascending 'VV'-polarised images in UF mode led to 100% probability of detection for threshold values of $1.9dB$ or below and over 50 false alarms. The RSO filter resulted in a lower detectability, but also in less false alarms; 69% and over 20 false alarms. Although images could be acquired daily over Svalbard by RADARSAT-2, this is very costly and thus only few images were made available for this project.

For Sentinel-1A there were only images available in EW mode covering Svalbard. Due to the coarse resolution of the EW mode (pixel spacing of $40m$) the extent of debris fields was not clearly outlined, but their location could be detected manually. By applying the automatic detection method using a RSO filter and threshold value of $3.4dB$ on the descending 'HV'-polarised image 100% of the debris fields were detected, but at the expense of 13 false alarms. Besides the high probability of detection and low number of false alarms when using Sentinel-1A images, it also has the advantage of acquiring images twice per day on Svalbard

(a descending and an ascending image) for free.

None of the designed automatic detection methods resulted in a 100% probability of detection and zero false alarms, but they do confirm that automatic detection of avalanches in these SAR images is possible. They also show that the automatic detection method should be adapted to the input data, or at least taking the pixel spacing into account when using a RSO filter. For the RADARSAT-2 UF mode images the best result is obtained by using a median filter and a threshold value of $1.9dB$, while for the Sentinel-1A EW mode images a RSO filter in combination with a threshold value of $3.4dB$ resulted in the optimum detection. In the future the results in this thesis can be used for operational avalanche monitoring and to map frequency and locations where avalanches occur.

8.2 Suggestions for further research

The recommendations listed in this section provide suggestions for further research related to automatic detection of avalanches in SAR images. The designed automatic methods in this thesis have been specified for RADARSAT-2 UF mode images and for Sentinel-1A EW mode images. The first paragraph focuses potential improvements that can be made to the choice of SAR data and/or pre-processing. The second paragraph lists recommendations to improve the designed automatic detection method making it operational and useful also for other SAR images. The third paragraph gives suggestions on other methodologies to optimise mapping and monitoring of avalanches. And finally, the fourth paragraph concludes with some final remarks.

Choice of SAR data and pre-processing

- *Test automatic detection method on more RADARSAT-2 and Sentinel-1A data*
  To further optimise the designed automatic detection method it should be tested on a greater variety of SAR data. The methods are now specified for a few RADARSAT-2 UF mode and Sentinel-1A EW mode images. By testing it on other SAR images a more general automatic detection method can be designed.

  Although this study shows that the Sentinel-1A EW mode can be used to both manual and automatic detection of avalanches, it is not as well suited as the Sentinel-1A Interferometric Wide swath (IW) mode. The EW mode, which is now the preferred mode for Svalbard due to sea-ice monitoring, acquires images with a pixel spacing of $40m$ and therefore does not detect the extent of debris fields. Due to the improved spatial resolution of the IW mode ($10m$), it is expected that both the location and extent are detected. The Sentinel-1A acquisition plan over Svalbard might change in the future, enabling the use of IW mode data.
- *Average multiple images as reference image*
  By averaging multiple reference images into one, the result of the detection will depend less on the quality of a single reference image. In this case, it is advisable to enter a pre-condition based on the wetness of the snow to guide the choice and weight of the reference images.
- *Combine information from descending and ascending images in both cross- and co-polarisation*

Co-polarisation gives more information in the line of direction of the beam, while cross-polarisation is more sensitive to surfaces with multiple scatterers, such as buildings. Descending and ascending have different imaging geometry due to the side-looking radar. Thus by combining data from cross- and co-polarised channels and ascending and descending more information can be obtained useful for research.

- *Use SLC Level-1B products*
  In case Single Look Complex (SLC) is used instead of multi-looked Ground Range Detected (GRD) products, the original spatial resolution is maintained. An high spatial resolution in combination with low speckle noise is favourable for avalanche detection. As multi-looking reduces speckle, SLC products need an advanced speckle reduction filter.

Enhancing processing methodology

- *Apply automatic detection on subwindow of a SAR image*
  First apply a high threshold on smaller windows of the image based on the information gained from spatial profiles. Spatial profiles can be created using for example ENVI, in order to analyse the extent of avalanches and highest backscatter value within debris fields. Hereafter, discard all windows where nothing has been detected. This will hopefully lower the number of false alarms or at least eliminates the false alarms that have a backscatter coefficient lower than the first set threshold value.
- *Include a shape condition in designed automatic detection method*
  The number of false alarms can be lowered by including a shape condition filtering out non tongue-shaped features. This is solely possible for high spatial resolution images ($3m$). However, their could be drawbacks when including such a condition as not all avalanches are clearly tongue-shaped.
- *Analyse time span debris fields are visible in the SAR images*
  By applying the automatic detection on consecutive images the appearance and disappearance of debris fields over time can be analysed. This can then be used as a condition in the automatic detection method, e.g. in case a pixel is classified as avalanche in one image (or at least in less images than set by the condition) but not in the subsequent images it is most probably a false alarm. In order to do this, images with a high acquisition frequency are needed (for example daily), such as obtained by Sentinel-1A.

Other methodologies

- *Combine automatic detection of SAR with other data sources*
  Ground-based radar can be employed to specifically monitor very hazardous slopes, while optical data can be used to validate automatically detected avalanches.
- *Supervised classification*
  Instead of basing the automatic detection on change detection by thresholding, supervised classification can be tested as well. The classification is performed on the difference in backscatter coefficient between an image showing avalanche activity and a reference image, just as for change detection. However, for supervised classification clusters or classes are predefined by the operator.

Concluding remarks

All in all, this study shows that automatic detection of avalanches is possible in RADARSAT-2 UF mode images as well as in Sentinel-1A EW mode images. Due to their varying characteristics, the designed automatic detection method is different for both satellites. By combining a regular detection (twice per day) of the whole of Svalbard by the coarse Sentinel-1A EW mode images and a more specified forecasting using the fine RADARSAT-2 UF mode images avalanche maps can be created indicating both location and extent of debris fields. These maps can be of great value for avalanche warning services, although further research is necessary before automatically generated avalanche maps can be included in daily operations.

Appendix A

RADARSAT-2 UF mode images

A.1 Automatically detected avalanches in ascending RADARSAT-2 UF mode image in 'VV'-polarisation using a median filter

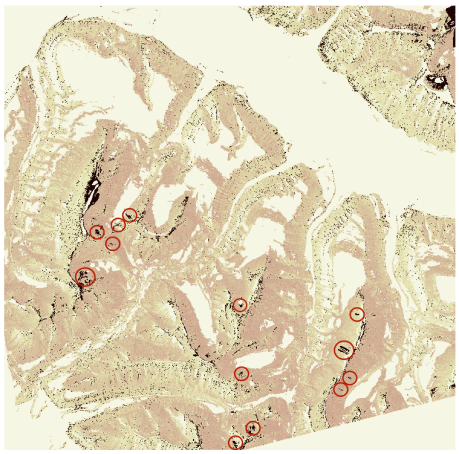

(a) 1.5dB

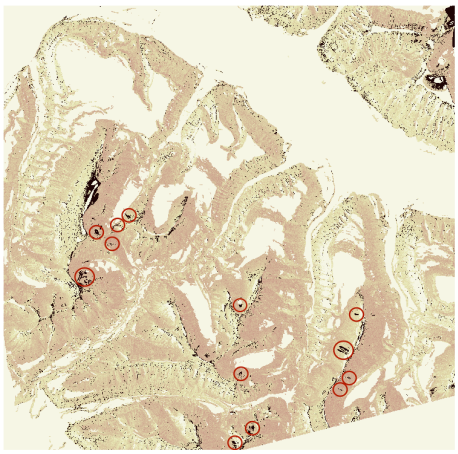

(b) 1.6dB

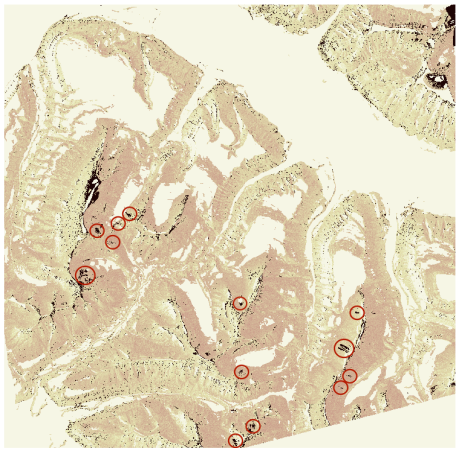

(c) 1.7dB

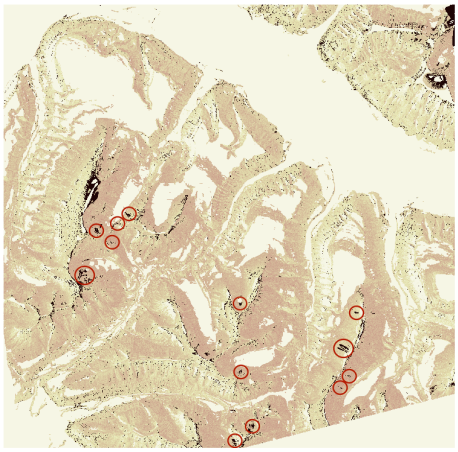

(d) 1.8dB

Figure A.1: Results of automatic detection method using post-classification filter 1: Median filter and threshold values between 1.5dB and 1.8dB with steps of 0.1dB applied on ascending RADARSAT-2 UF difference image from *'20130610'* and *'20130914'* in 'VV'-polarisation.

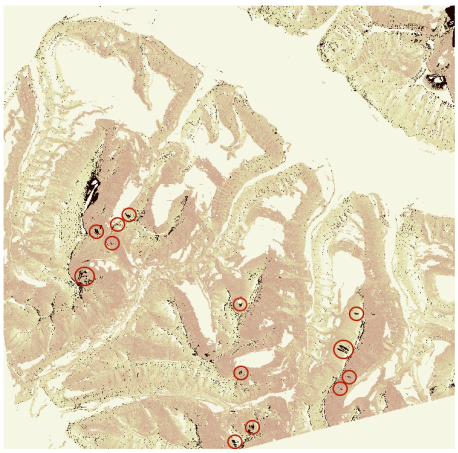

(a) 1.9dB

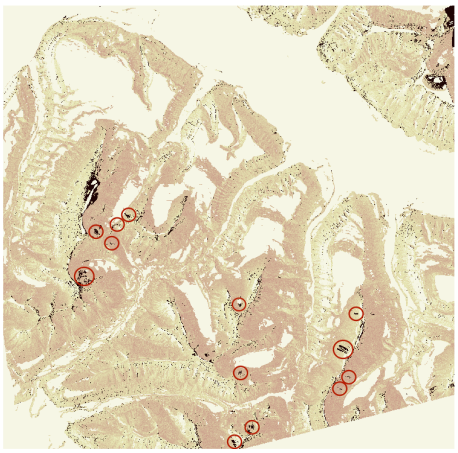

(b) 2dB

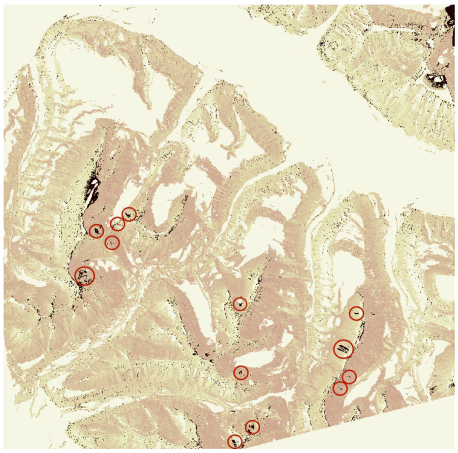

(c) 2.1dB

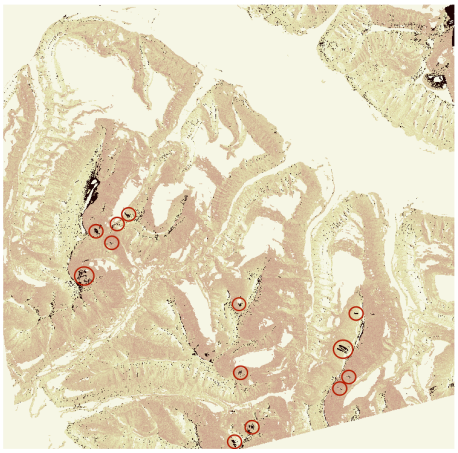

(d) 2.2dB

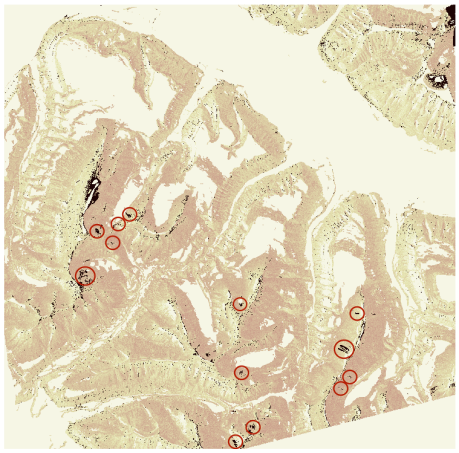

(e) 2.2dB

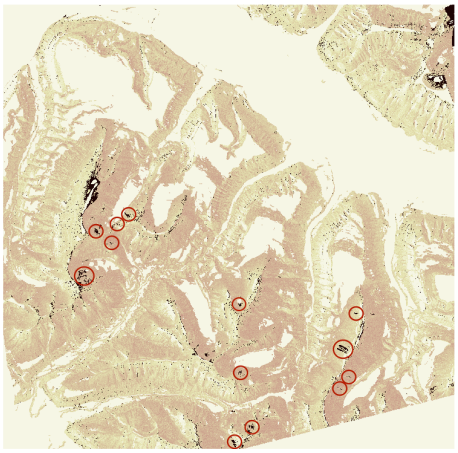

(f) 2.4dB

Figure A.2: Results of automatic detection method using post-classification filter 1: Median filter and threshold values between 1.9dB and 2.4dB with steps of 0.1dB applied on the ascending RADARSAT-2 UF difference image from *'20130610'* and *'20130914'* in 'VV'-polarisation.

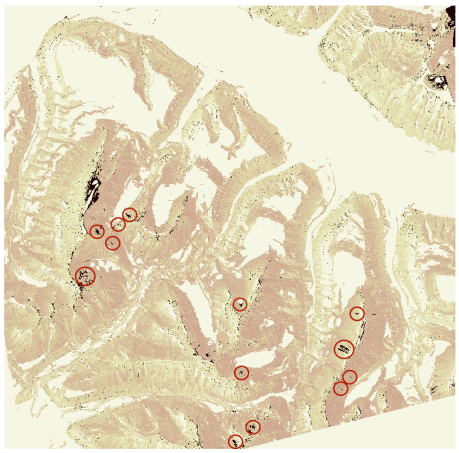

(a) 2.5dB

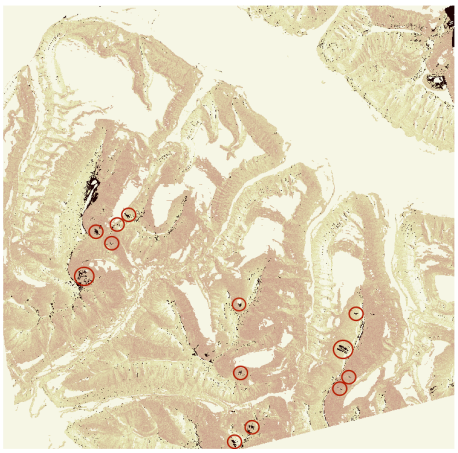

(b) 2.6dB

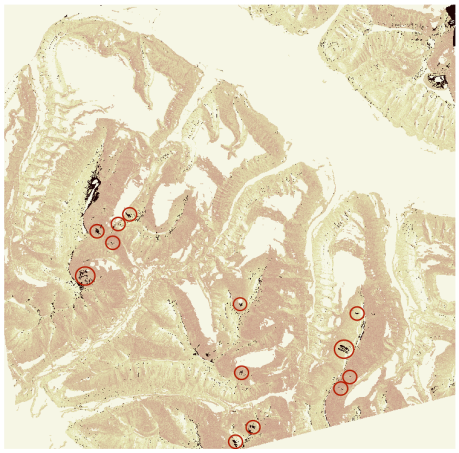

(c) 2.7dB

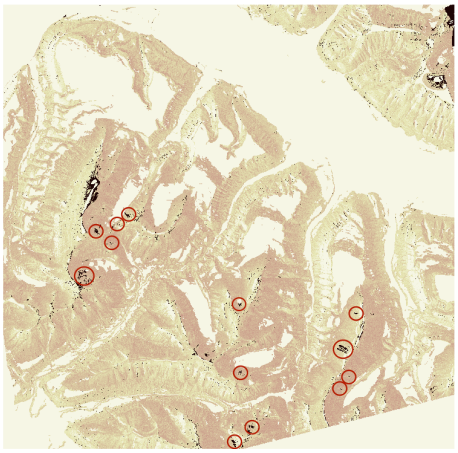

(d) 2.8dB

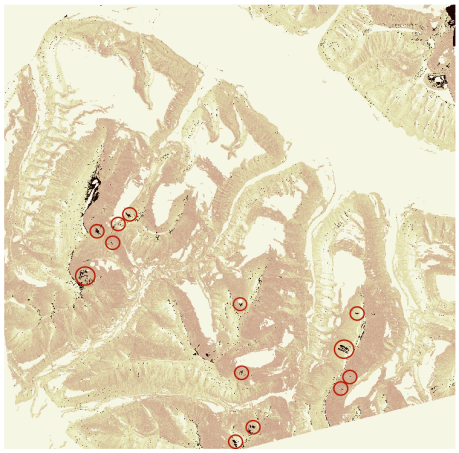

(e) 2.9dB

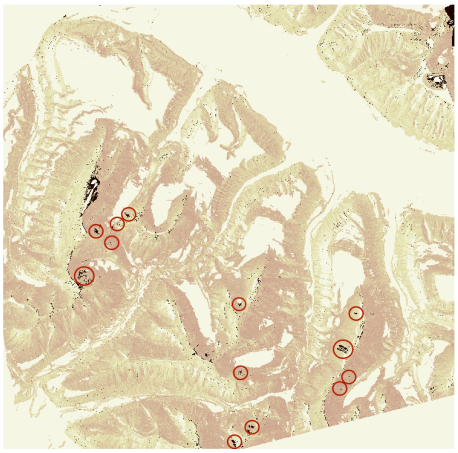

(f) 3dB

Figure A.3: Results of automatic detection method using post-classification filter 1: Median filter and threshold values between 2.5dB and 3dB with steps of 0.1dB applied on ascending RADARSAT-2 UF difference image from *'20130610'* and *'20130914'* in 'VV'-polarisation.

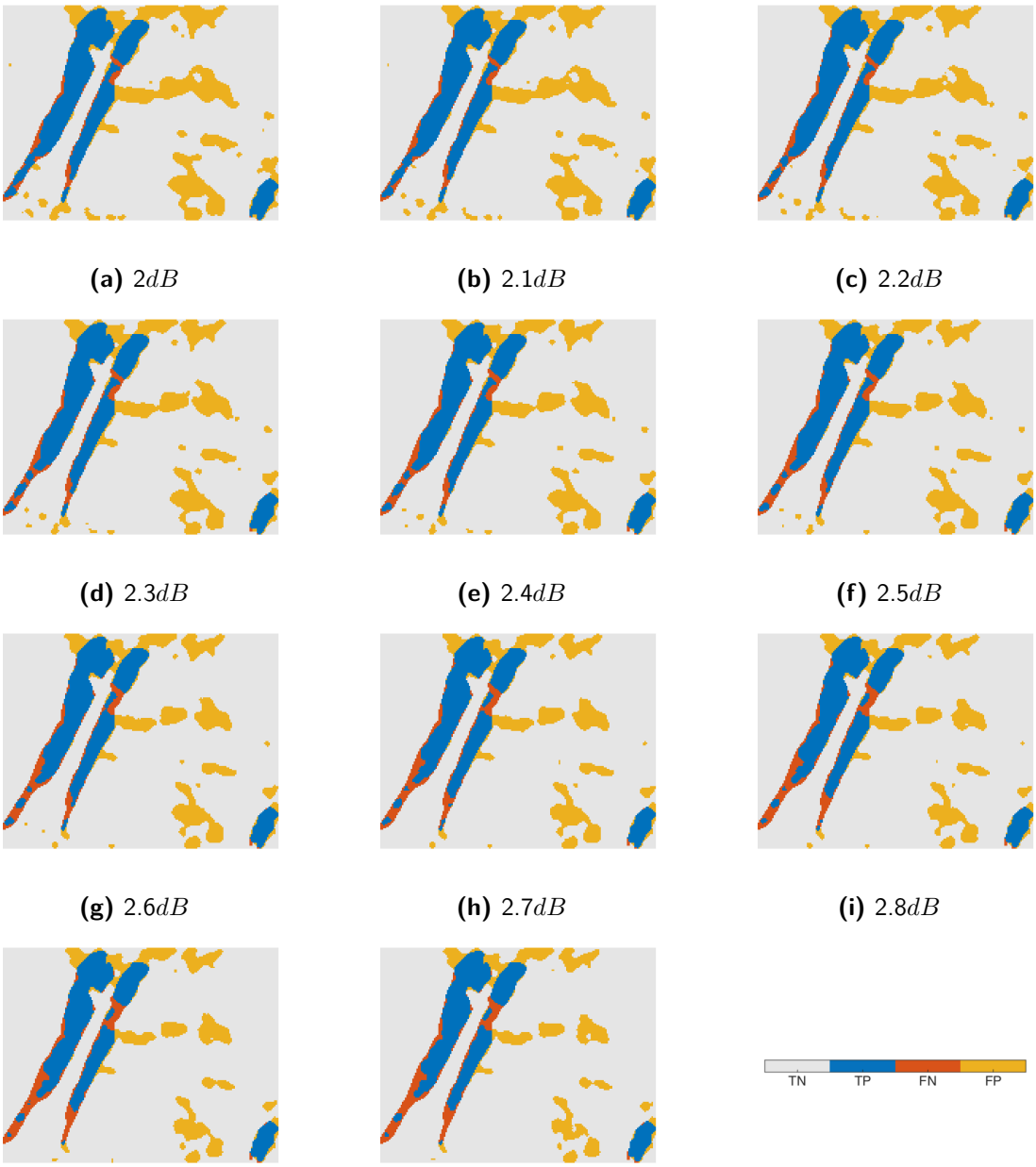

(a) $2dB$ **(b)** $2.1dB$ **(c)** $2.2dB$

(d) $2.3dB$ **(e)** $2.4dB$ **(f)** $2.5dB$

(g) $2.6dB$ **(h)** $2.7dB$ **(i)** $2.8dB$

(j) $2.9dB$ **(k)** $3dB$

Figure A.4: Results of automatic detection method using post-classification filter 1: Median filter and threshold values between $2dB$ and $3dB$ with steps of $0.1dB$ applied on window 1 of ascending RADARSAT-2 UF difference image from *'20130610'* and *'20130914'* in 'VV'-polarisation. True negatives (TN), true positives (TP), false negatives (FN) and false positives (FP) are indicated in grey, blue, red and yellow respectively.

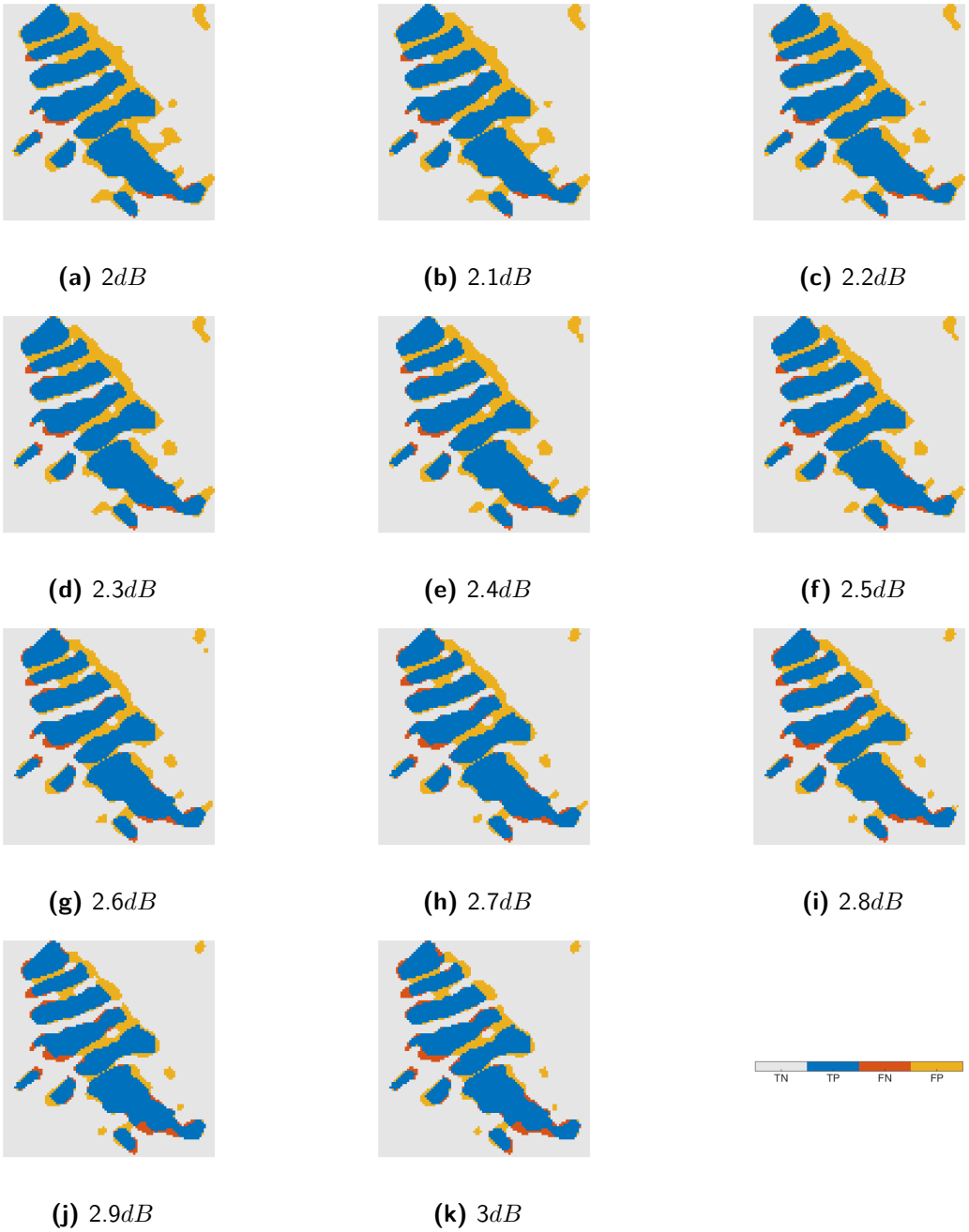

(a) $2dB$ **(b)** $2.1dB$ **(c)** $2.2dB$

(d) $2.3dB$ **(e)** $2.4dB$ **(f)** $2.5dB$

(g) $2.6dB$ **(h)** $2.7dB$ **(i)** $2.8dB$

(j) $2.9dB$ **(k)** $3dB$

Figure A.5: Results of automatic detection method using post-classification filter 1: Median filter and threshold values between $2dB$ and $3dB$ with steps of $0.1dB$ applied on window 2 of ascending RADARSAT-2 UF difference image from *'20130610'* and *'20130914'* in 'VV'-polarisation. True negatives (TN), true positives (TP), false negatives (FN) and false positives (FP) are indicated in grey, blue, red and yellow respectively.

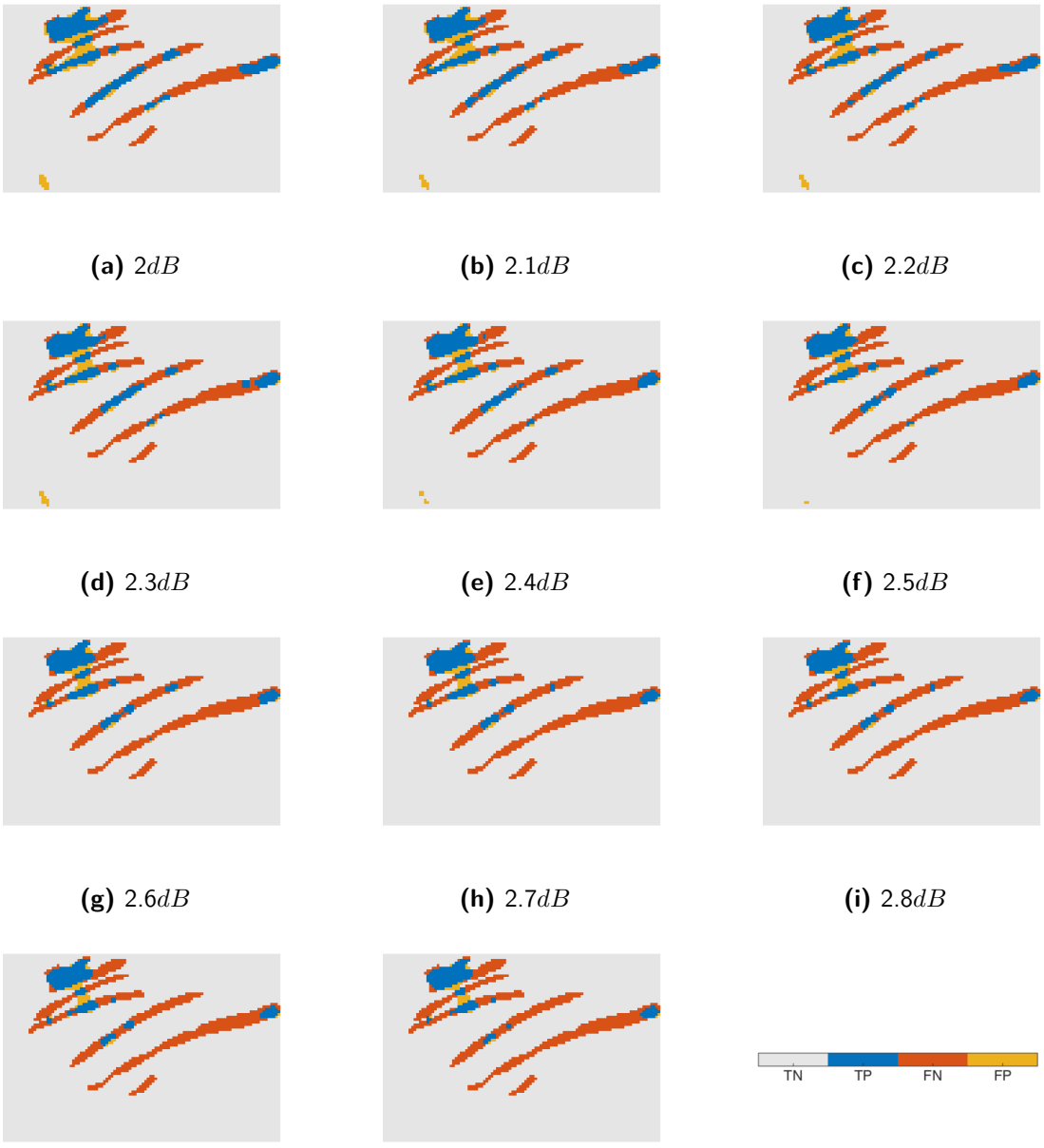

(a) $2dB$ **(b)** $2.1dB$ **(c)** $2.2dB$

(d) $2.3dB$ **(e)** $2.4dB$ **(f)** $2.5dB$

(g) $2.6dB$ **(h)** $2.7dB$ **(i)** $2.8dB$

(j) $2.9dB$ **(k)** $3dB$

Figure A.6: Results of automatic detection method using post-classification filter 1: Median filter and threshold values between $2dB$ and $3dB$ with steps of $0.1dB$ applied on window 3 of ascending RADARSAT-2 UF difference image from *'20130610'* and *'20130914'* in 'VV'-polarisation. True negatives (TN), true positives (TP), false negatives (FN) and false positives (FP) are indicated in grey, blue, red and yellow respectively.

A.2 Automatically detected avalanches in ascending RADARSAT-2 UF mode image in 'VV'-polarisation using a RSO filter

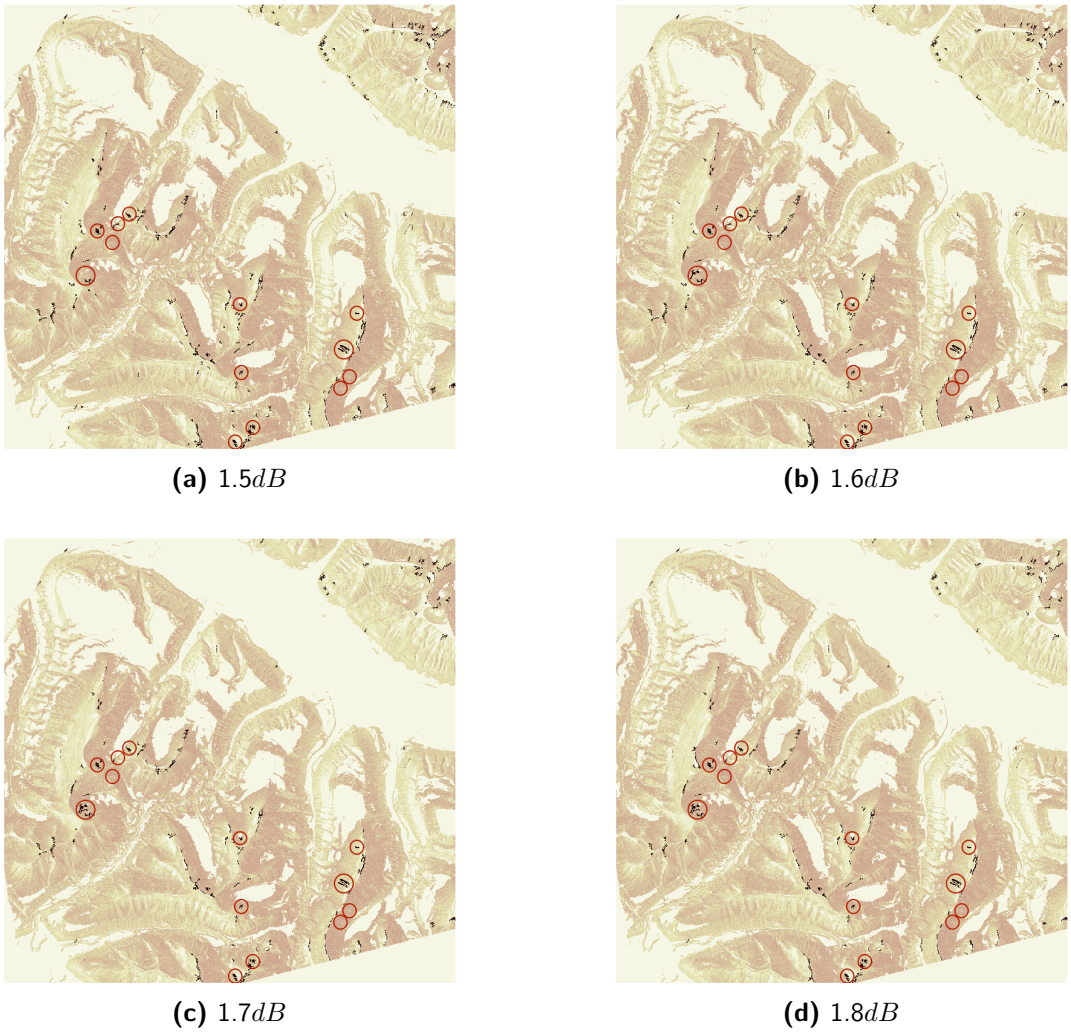

(a) 1.5dB **(b)** 1.6dB

(c) 1.7dB **(d)** 1.8dB

Figure A.7: Results of automatic detection method using post-classification filter 2: RSO filter and threshold values between 1.5dB and 1.8dB with steps of 0.1dB applied on ascending RADARSAT-2 UF difference image from *'20130610'* and *'20130914'* in 'VV'-polarisation.

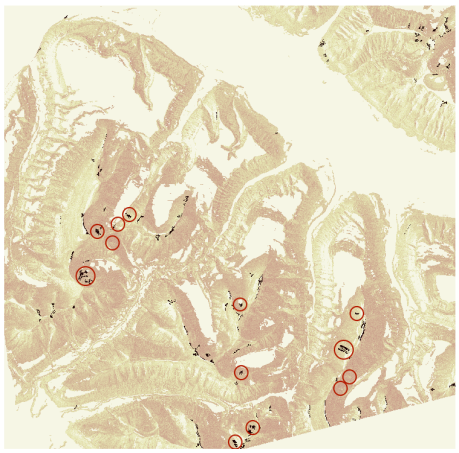

(a) 1.9dB

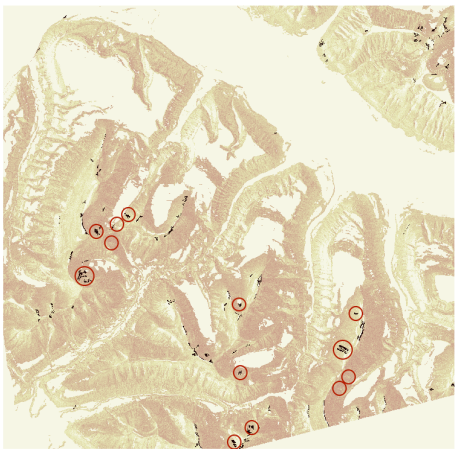

(b) 2dB

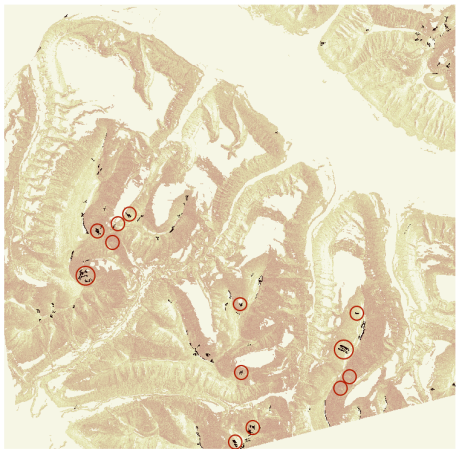

(c) 2.1dB

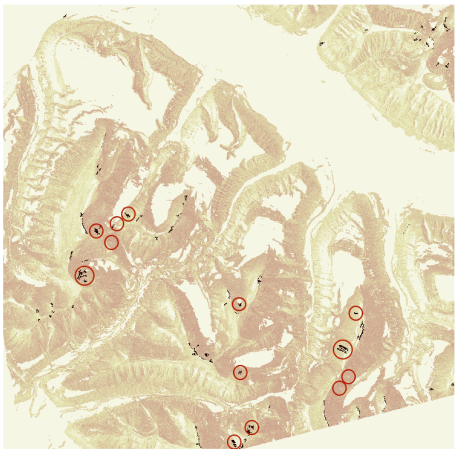

(d) 2.2dB

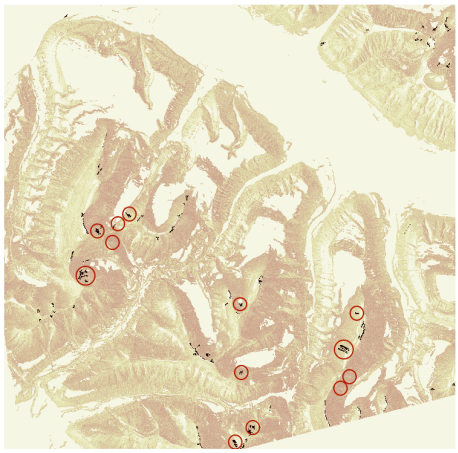

(e) 2.2dB

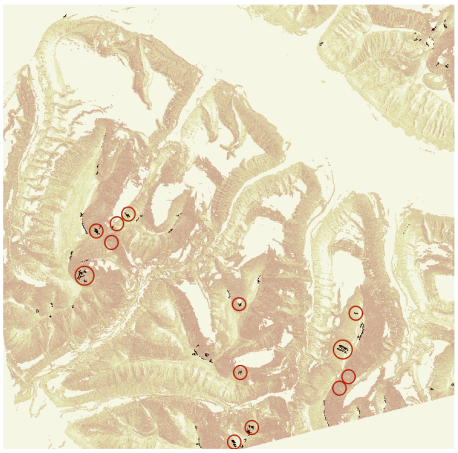

(f) 2.4dB

Figure A.8: Results of automatic detection method using post-classification filter 2: RSO filter and threshold values between 1.9dB and 2.4dB with steps of 0.1dB applied on the ascending RADARSAT-2 UF difference image from *'20130610'* and *'20130914'* in 'VV'-polarisation.

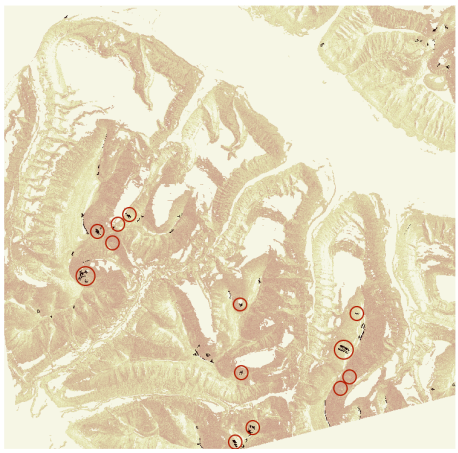

(a) 2.5dB

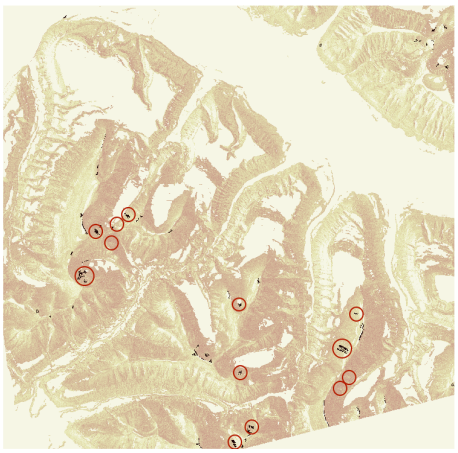

(b) 2.6dB

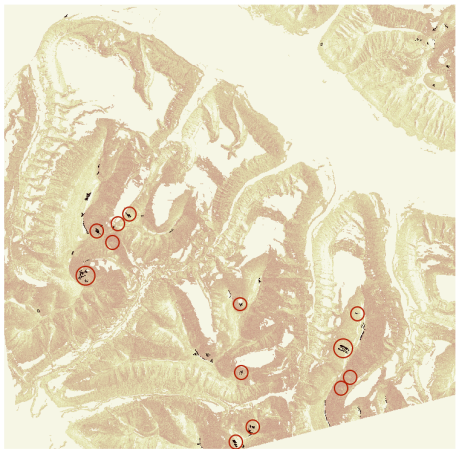

(c) 2.7dB

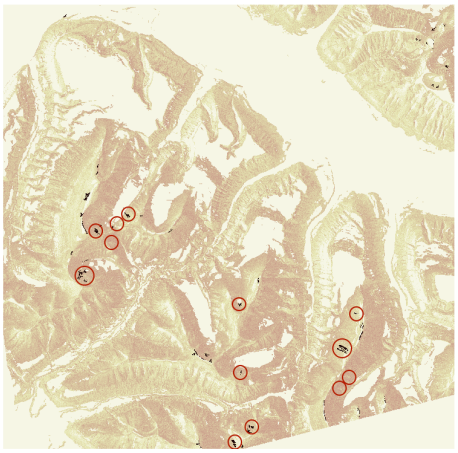

(d) 2.8dB

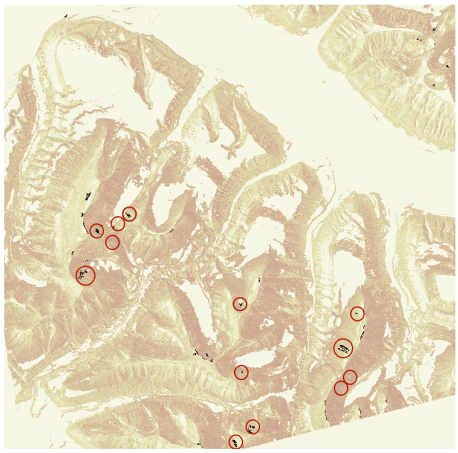

(e) 2.9dB

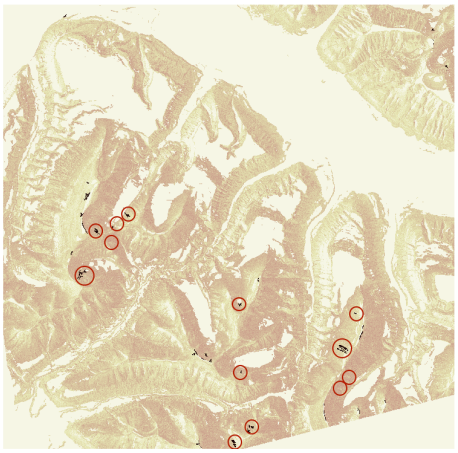

(f) 3dB

Figure A.9: Results of automatic detection method using post-classification filter 2: RSO filter and threshold values between 2.5dB and 3dB with steps of 0.1dB applied on the ascending RADARSAT-2 UF difference image from *'20130610'* and *'20130914'* in 'VV'-polarisation.

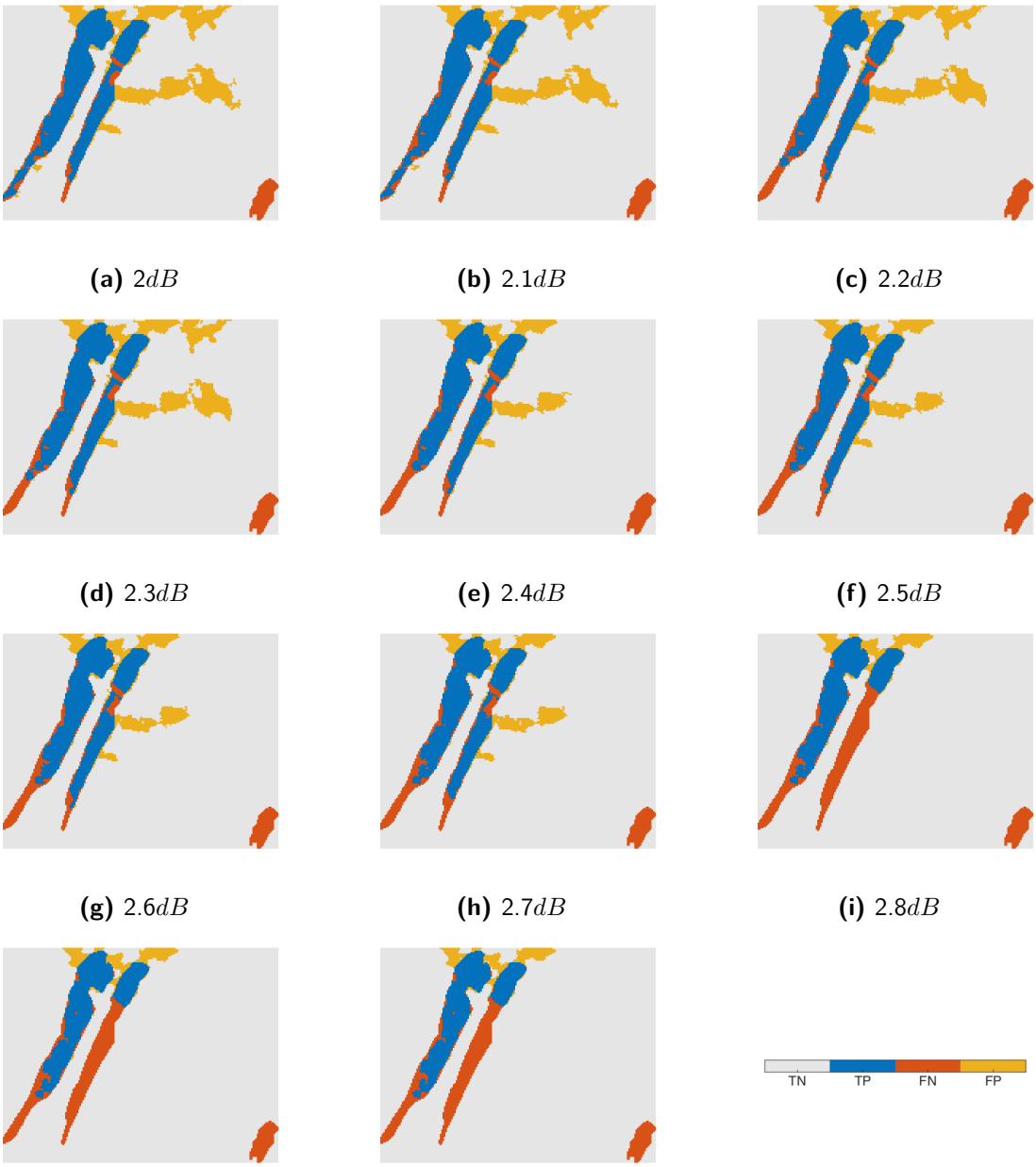

(a) $2dB$ **(b)** $2.1dB$ **(c)** $2.2dB$

(d) $2.3dB$ **(e)** $2.4dB$ **(f)** $2.5dB$

(g) $2.6dB$ **(h)** $2.7dB$ **(i)** $2.8dB$

(j) $2.9dB$ **(k)** $3dB$

Figure A.10: Results of automatic detection method using post-classification filter 2: RSO filter and threshold values between $2dB$ and $3dB$ with steps of $0.1dB$ applied on window 1 of the ascending RADARSAT-2 UF difference image from *'20130610'* and *'20130914'* in 'VV'-polarisation. True negatives (TN), true positives (TP), false negatives (FN) and false positives (FP) are indicated in grey, blue, red and yellow respectively.

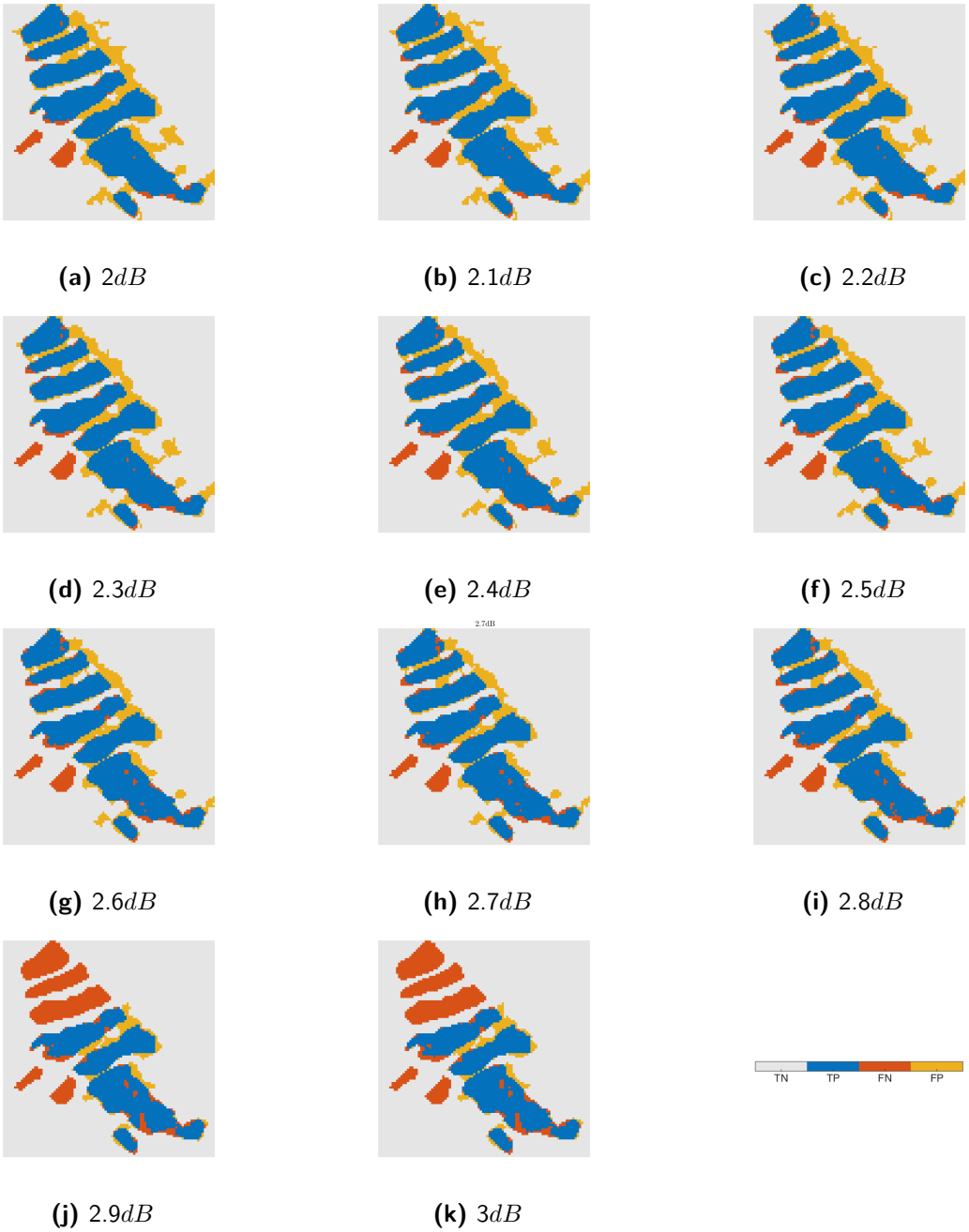

(a) $2dB$ **(b)** $2.1dB$ **(c)** $2.2dB$

(d) $2.3dB$ **(e)** $2.4dB$ **(f)** $2.5dB$

(g) $2.6dB$ **(h)** $2.7dB$ **(i)** $2.8dB$

(j) $2.9dB$ **(k)** $3dB$

Figure A.11: Results of automatic detection method using post-classification filter 2: RSO filter and threshold values between $2dB$ and $3dB$ with steps of $0.1dB$ applied on window 2 of the ascending RADARSAT-2 UF difference image from *'20130610'* and *'20130914'* in 'VV'-polarisation. True negatives (TN), true positives (TP), false negatives (FN) and false positives (FP) are indicated in grey, blue, red and yellow respectively.

Appendix B

Sentinel-1A EW mode images

B.1 Available descending and ascending Sentinel-1A EW mode images in 'HV'-polarisation

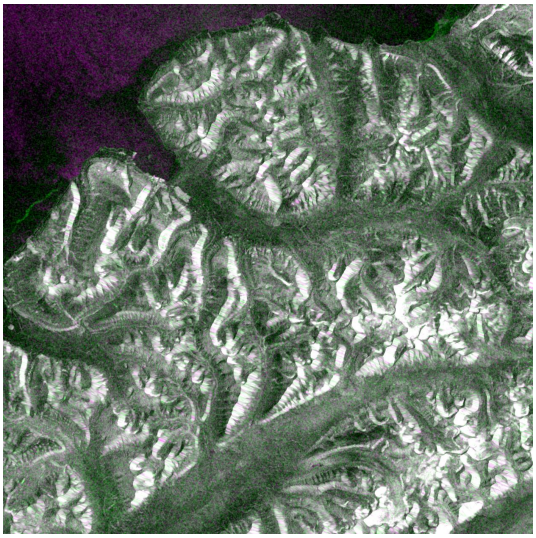

(a) *'20150302'* and *'20150314'*

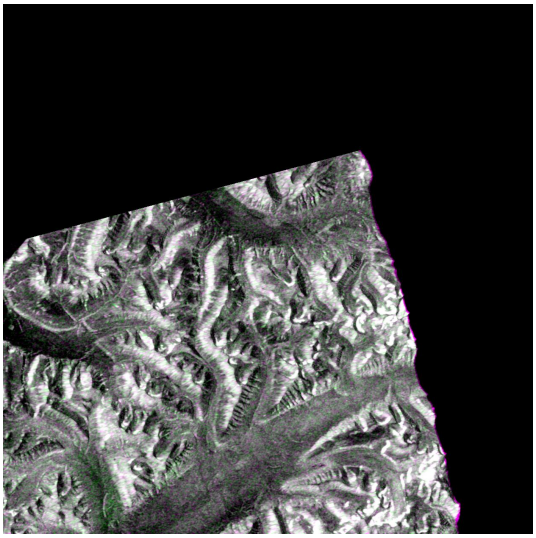

(b) *'20150302'* and *'20150314'*

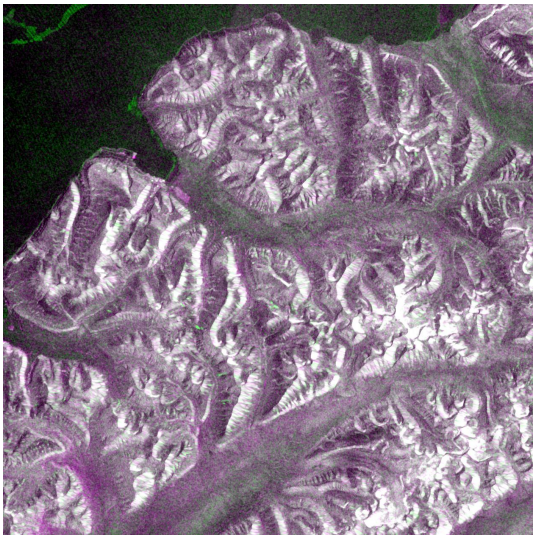

(c) *'20150304'* and *'20150316'*

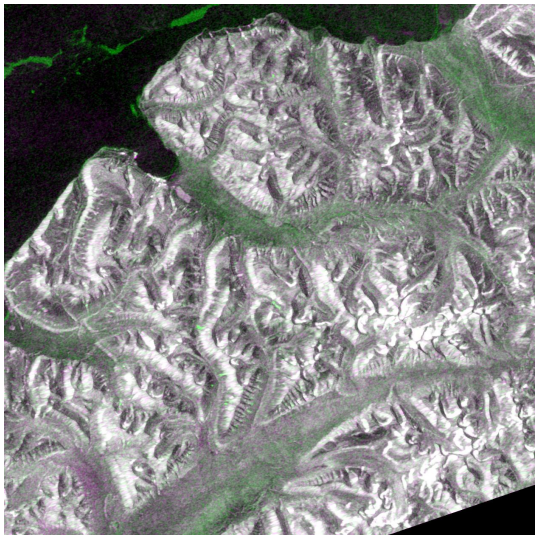

(d) *'20150304'* and *'20150316'*

Figure B.1: Available Sentinel-1A EW mode RGB images in HH'-polarisation covering Nordenskiöld Land on Svalbard, acquired between March 2^{nd} and 18^{th}, 2015. The images on the left are descending and on the right are ascending.

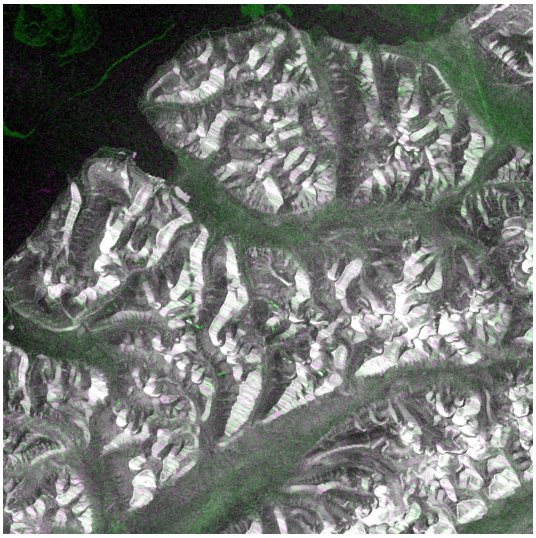

(a) *'20150305'* and *'20150317'*

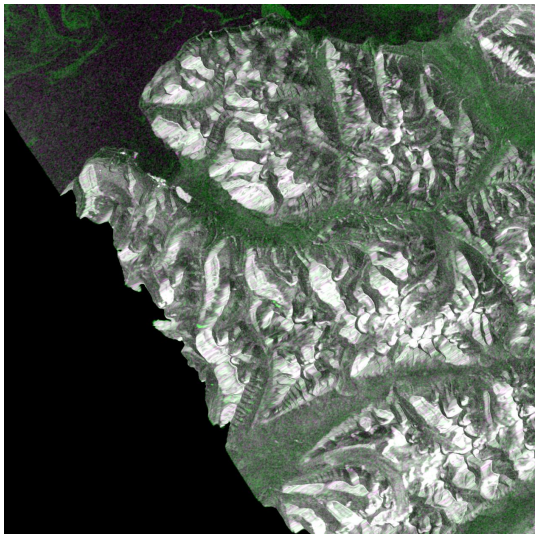

(b) *'20150305'* and *'20150317'*

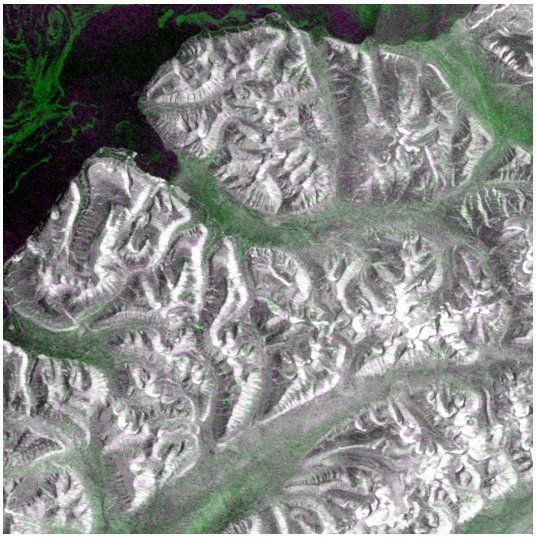

(c) *'20150306'* and *'20150318'*

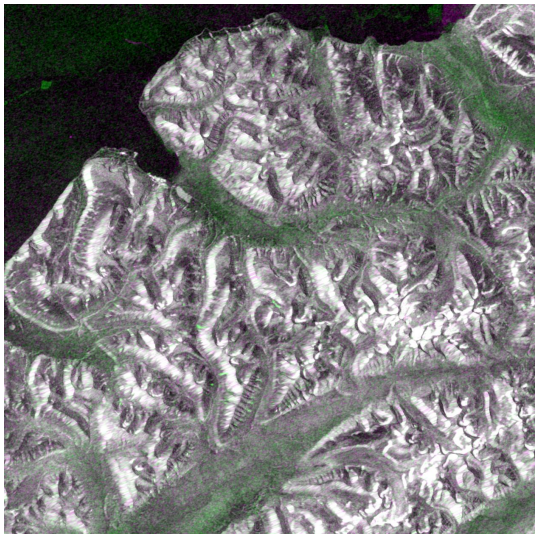

(d) *'20150306'* and *'20150318'*

Figure B.2: Available Sentinel-1A EW mode RGB images in HH'-polarisation covering Nordenskiöld Land on Svalbard, acquired between March 2^{nd} and 18^{th}, 2015. The images on the left are descending and on the right are ascending.

B.2 Manually detected avalanches in ascending Sentinel-1A EW mode image in 'HV'-polarisation

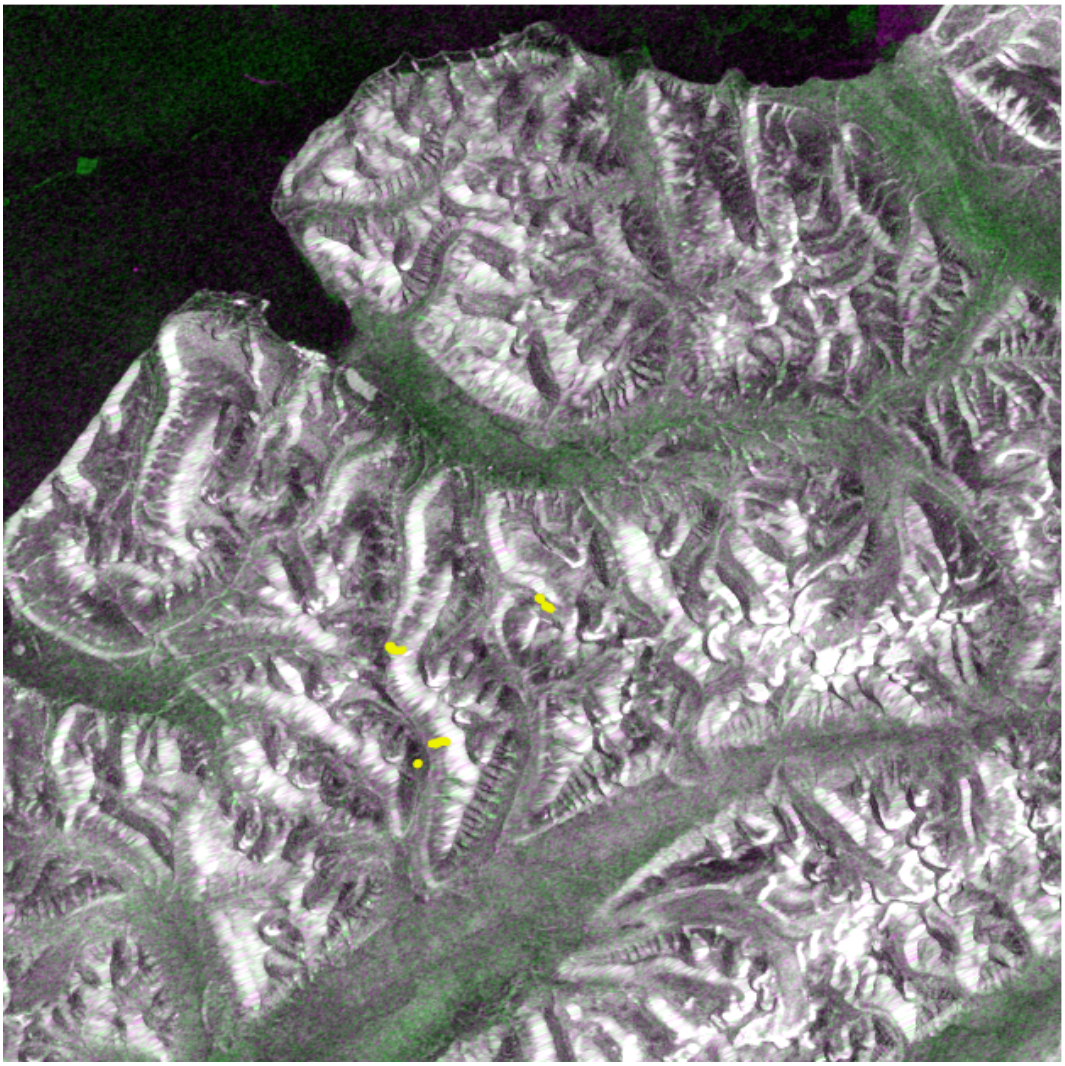

Figure B.3: Ascending Sentinel-1A EW mode RGB image in 'HV'-polarisation. Manually detected debris fields are indicated in yellow.

B.3 Automatically detected avalanches in descending Sentinel-1A EW mode image in 'HV'-polarisation using a RSO filter

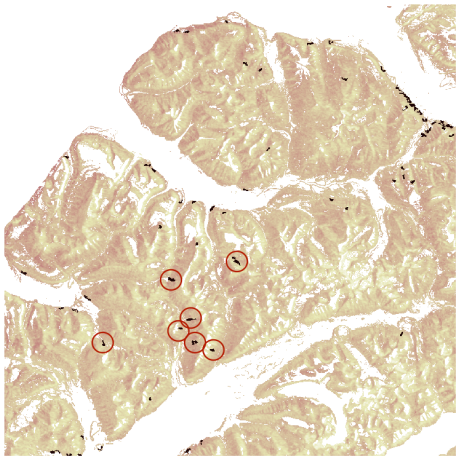

(a) $3dB$

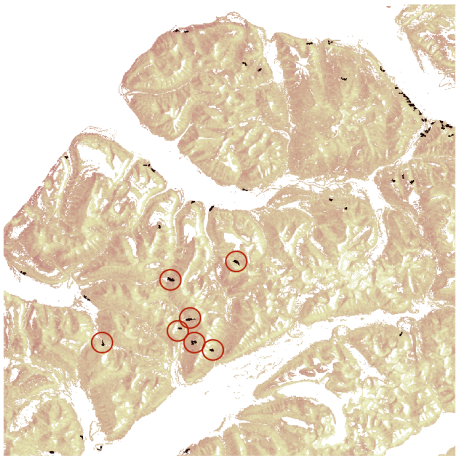

(b) $3.1dB$

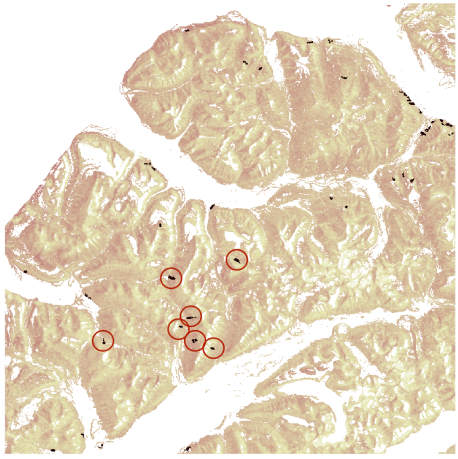

(c) $3.2dB$

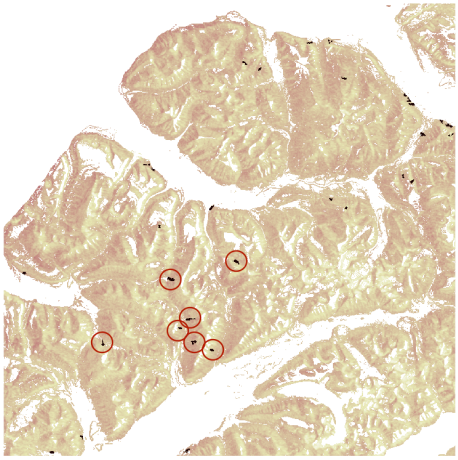

(d) $3.3dB$

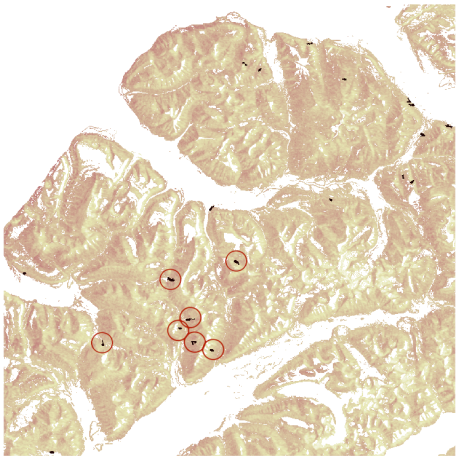

(e) $3.4dB$

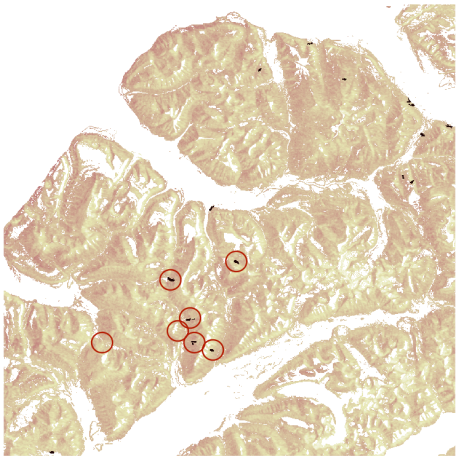

(f) $3.5dB$

Figure B.4: Results of automatic detection method using post-classification filter 2: RSO filter and threshold values between $3dB$ and $3.5dB$ with steps of $0.1dB$ applied on descending Sentinel-1A EW difference image from *'20150318'* and *'20150306'* in 'HV'-polarisation.

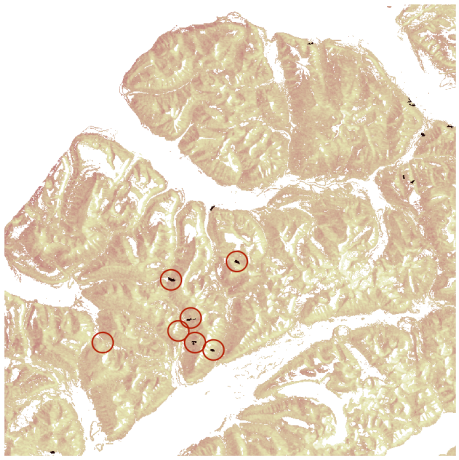

(a) 3.6dB

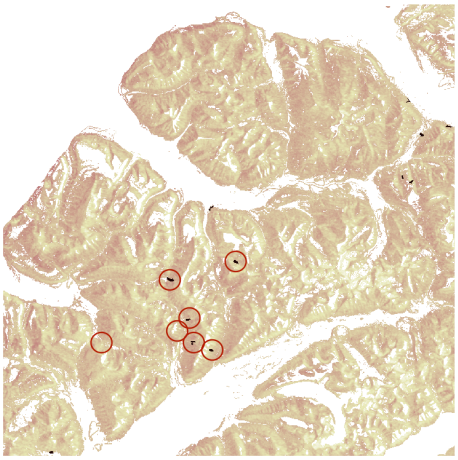

(b) 3.7dB

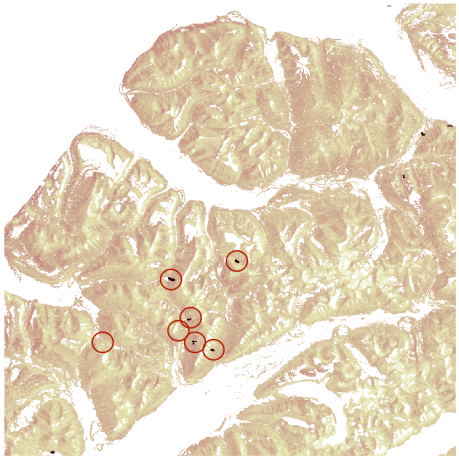

(c) 3.8dB

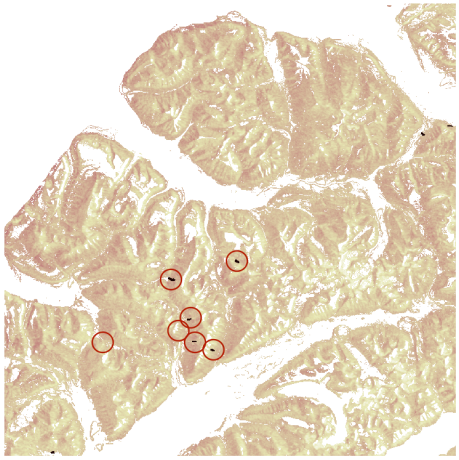

(d) 3.9dB

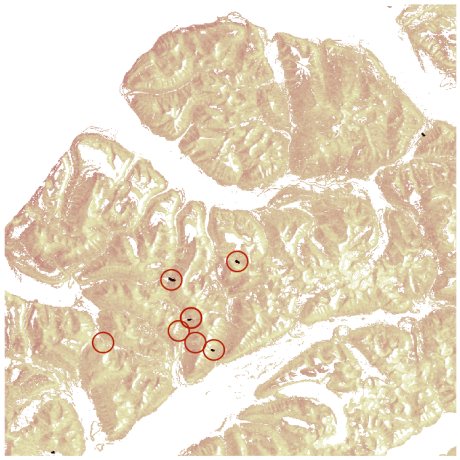

(e) 4dB

Figure B.5: Results of automatic detection method using post-classification filter 2: RSO filter and threshold values between 3.6dB and 4dB with steps of 0.1dB applied on descending Sentinel-1A EW difference image from *'20150318'* and *'20150306'* in 'HV'-polarisation.

B.4 Automatically detected avalanches in descending Sentinel-1A EW mode image in 'HH'-polarisation using a RSO filter

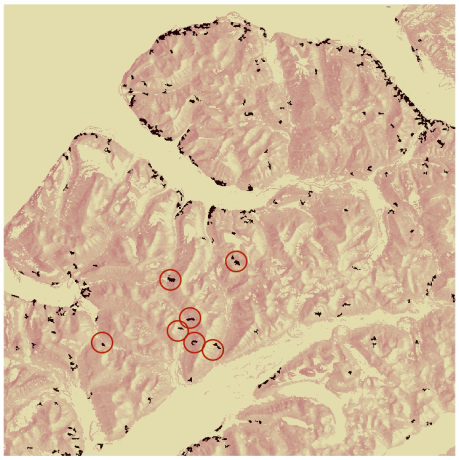

(a) $2dB$

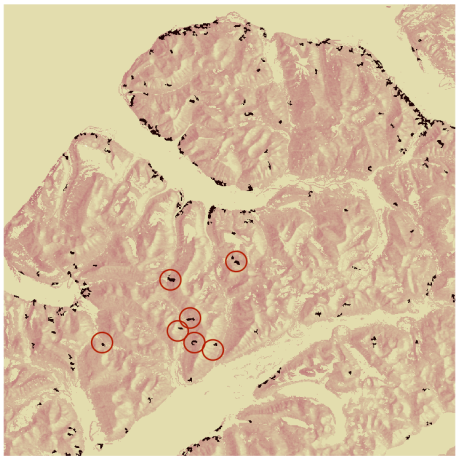

(b) $2.1dB$

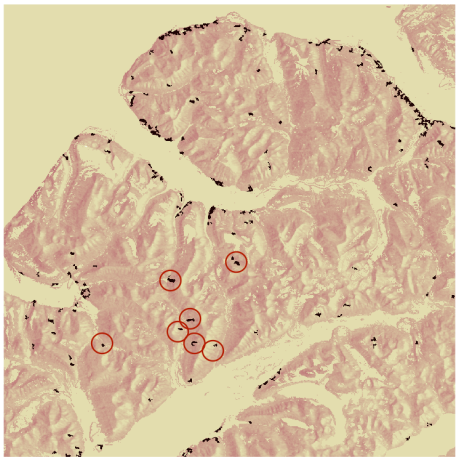

(c) $2.2dB$

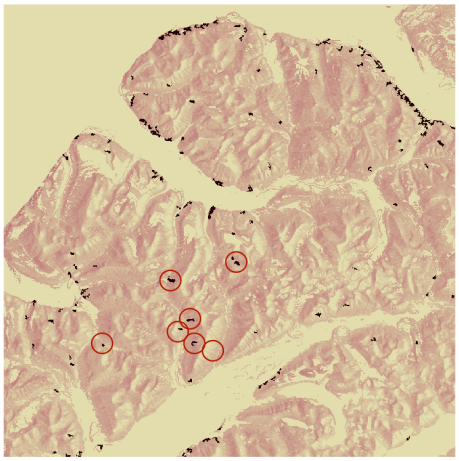

(d) $2.3dB$

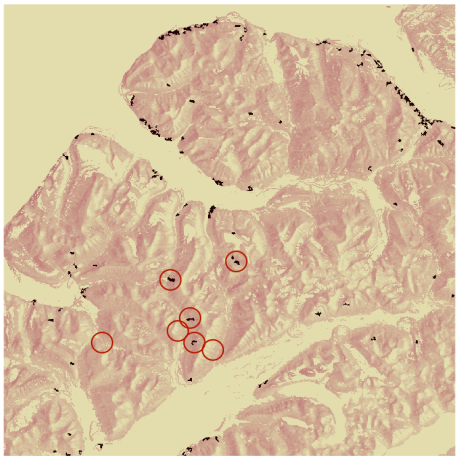

(e) $2.4dB$

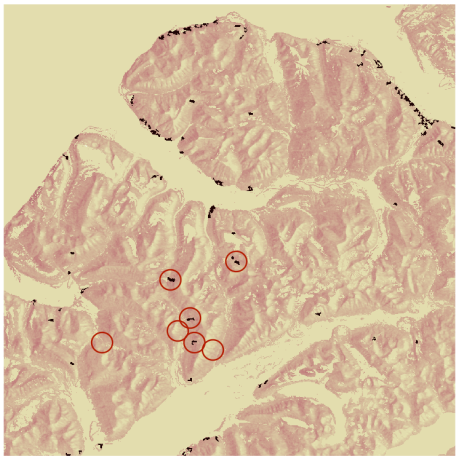

(f) $2.5dB$

Figure B.6: Results of automatic detection method using post-classification filter 2: RSO filter and threshold values between $2dB$ and $2.5dB$ with steps of $0.1dB$ applied on descending Sentinel-1A EW difference image from *'20150318'* and *'20150306'* in 'HH'-polarisation.

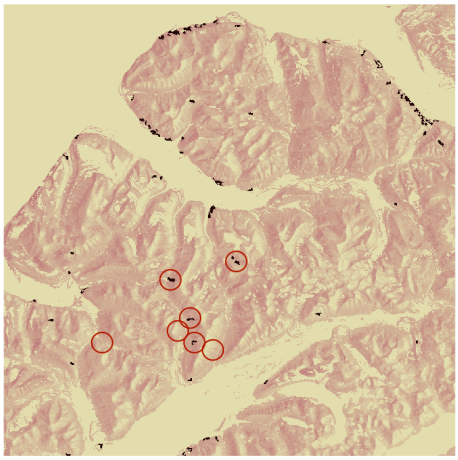

(a) 2.6dB

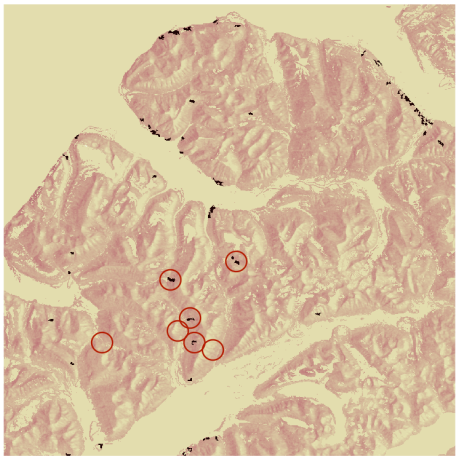

(b) 2.7dB

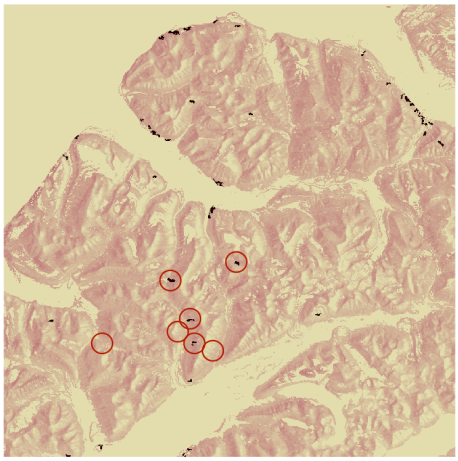

(c) 2.8dB

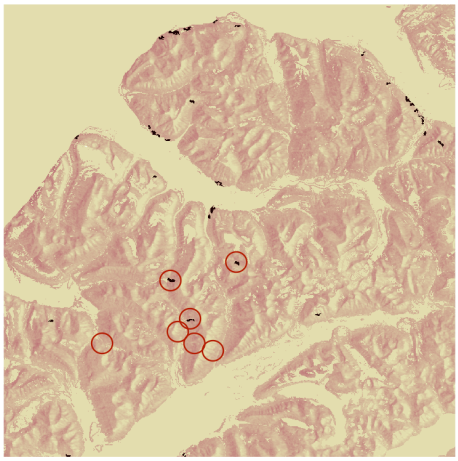

(d) 2.9dB

(e) 3dB

Figure B.7: Results of automatic detection method using post-classification filter 2: RSO filter and threshold values between 2.6dB and 3dB with steps of 0.1dB applied on descending Sentinel-1A EW difference image from *'20150318'* and *'20150306'* in 'HH'-polarisation.

B.5 Automatically detected avalanches in ascending Sentinel-1A EW mode image in 'HV'-polarisation using a RSO filter

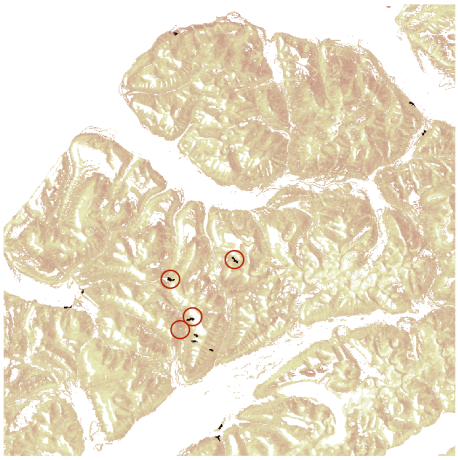

(a) $3dB$

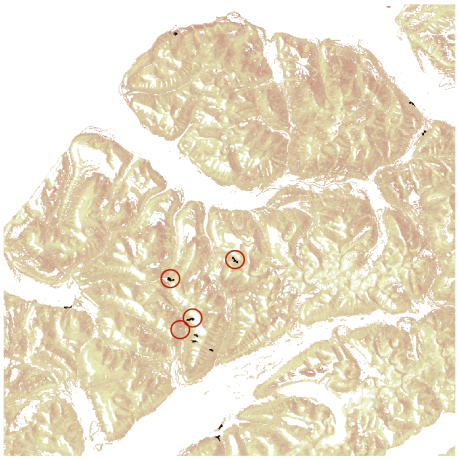

(b) $3.1dB$

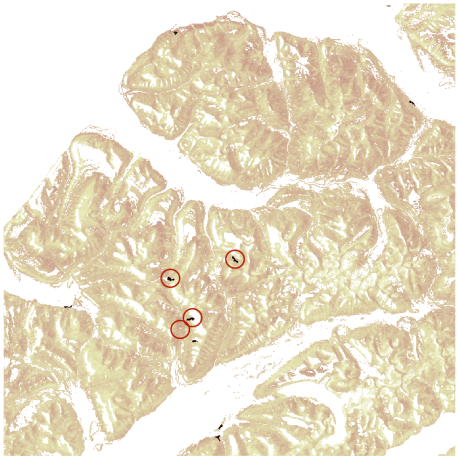

(c) $3.2dB$

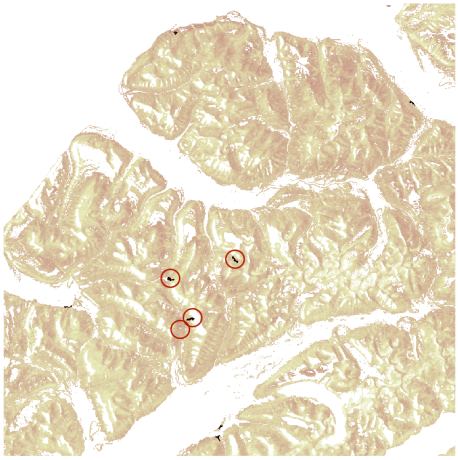

(d) $3.3dB$

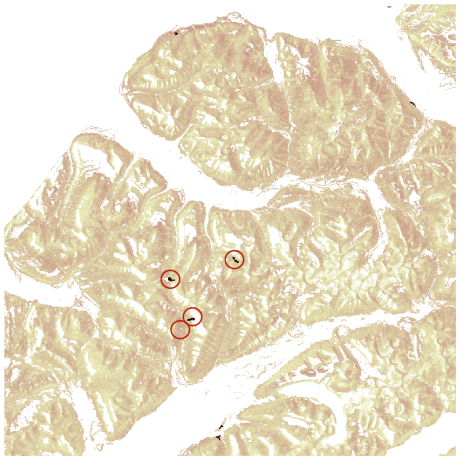

(e) $3.4dB$

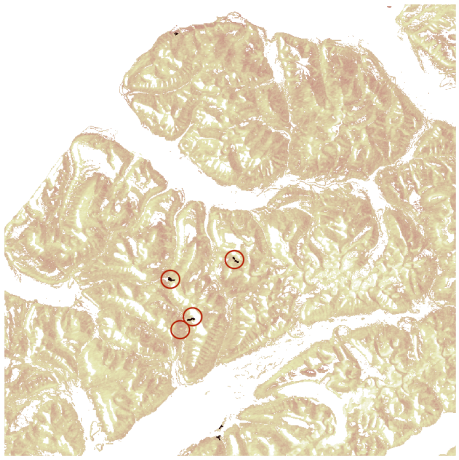

(f) $3.5dB$

Figure B.8: Results of automatic detection method using post-classification filter 2: RSO filter and threshold values between $3dB$ and $3.5dB$ with steps of $0.1dB$ applied on ascending Sentinel-1A EW difference image from *'20150318'* and *'20150306'* in 'HV'-polarisation.

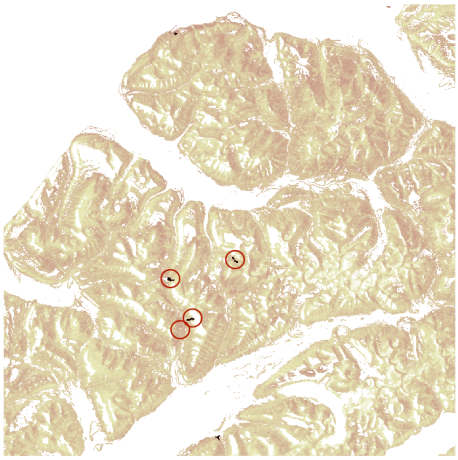

(a) 3.6dB

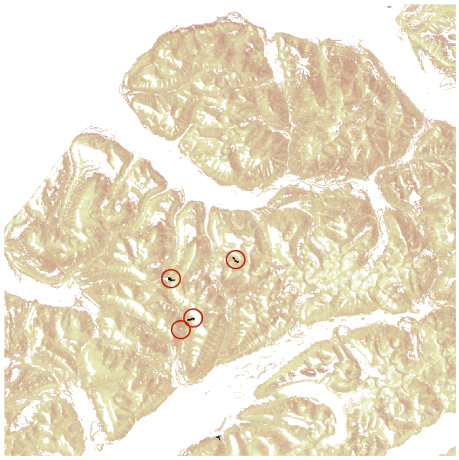

(b) 3.7dB

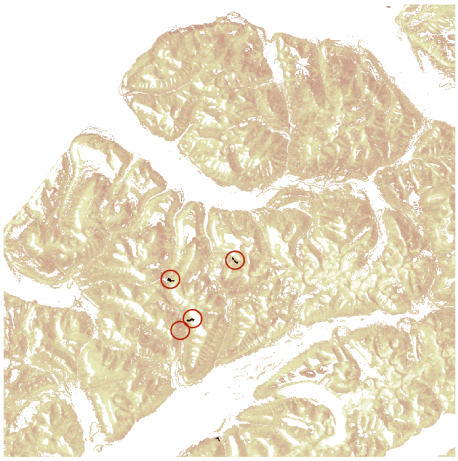

(c) 3.8dB

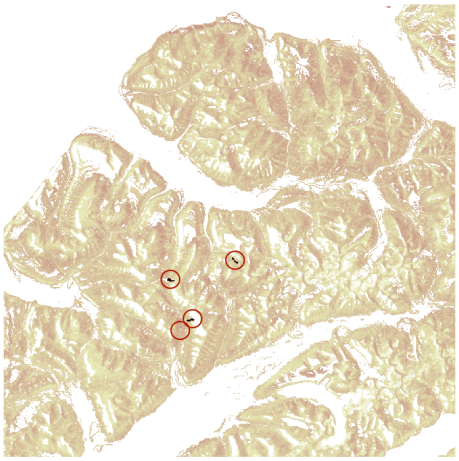

(d) 3.9dB

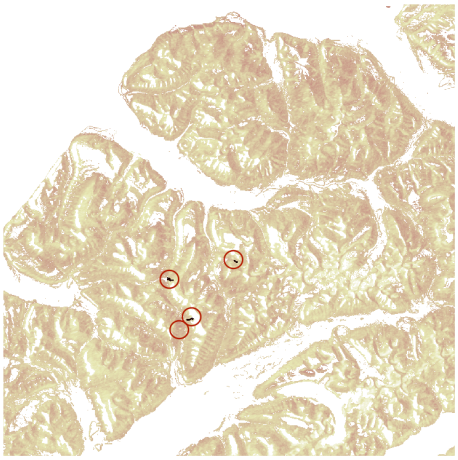

(e) 4dB

Figure B.9: Results of automatic detection method using post-classification filter 2: RSO filter and threshold values between 3.6dB and 4dB with steps of 0.1dB applied on ascending Sentinel-1A EW difference image from *'20150318'* and *'20150306'* in 'HV'-polarisation.

B.6 Automatically detected avalanches in ascending Sentinel-1A EW mode image in 'HH'-polarisation using a RSO filter

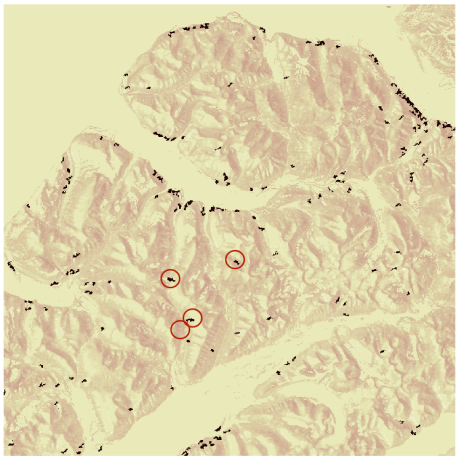

(a) $2dB$

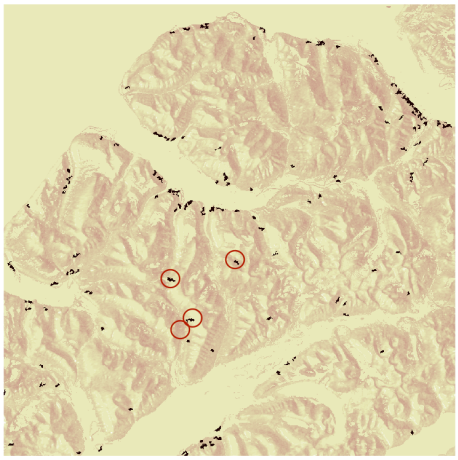

(b) $2.1dB$

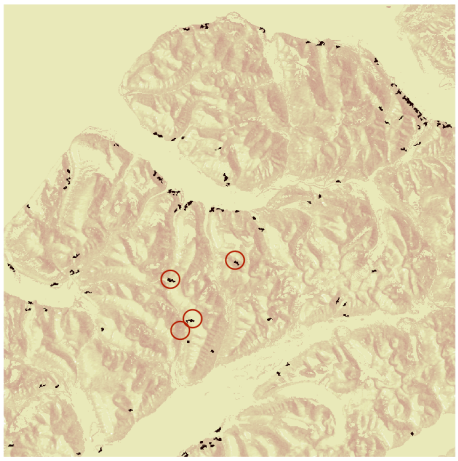

(c) $2.2dB$

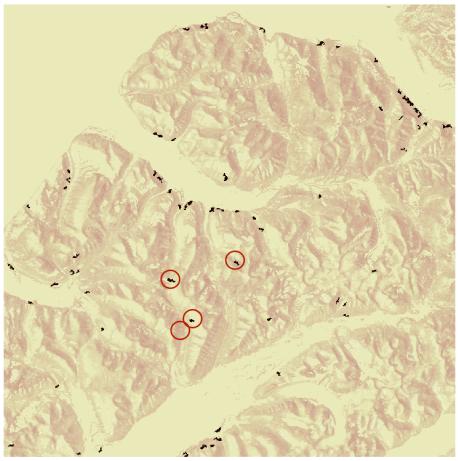

(d) $2.3dB$

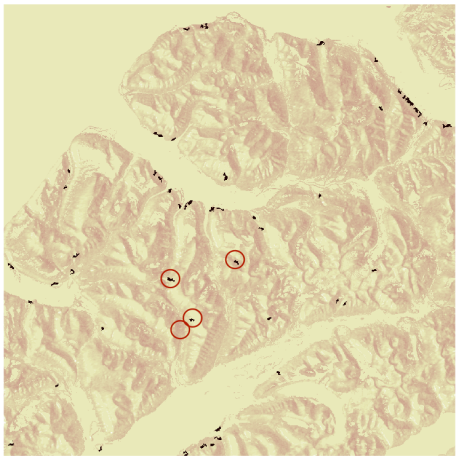

(e) $2.4dB$

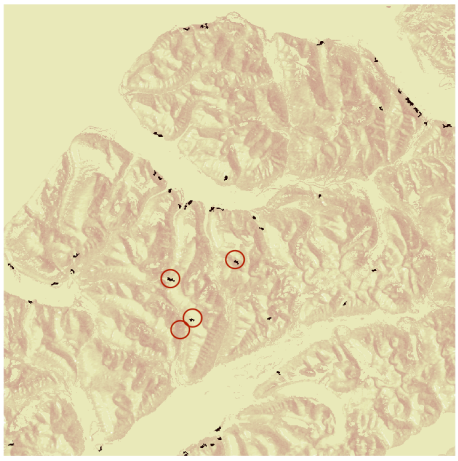

(f) $2.5dB$

Figure B.10: Results of automatic detection method using post-classification filter 2: RSO filter and threshold values between $2dB$ and $2.5dB$ with steps of $0.1dB$ applied on ascending Sentinel-1A EW difference image from *'20150318'* and *'20150306'* in 'HH'-polarisation.

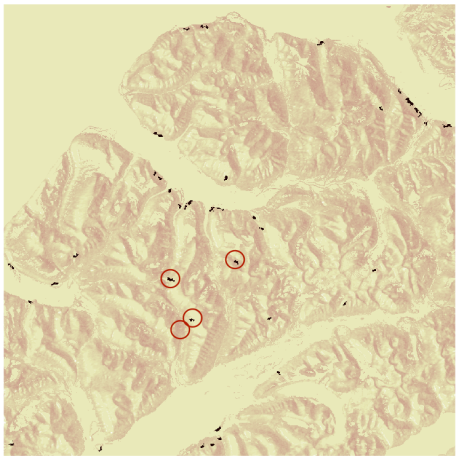

(a) 2.6dB

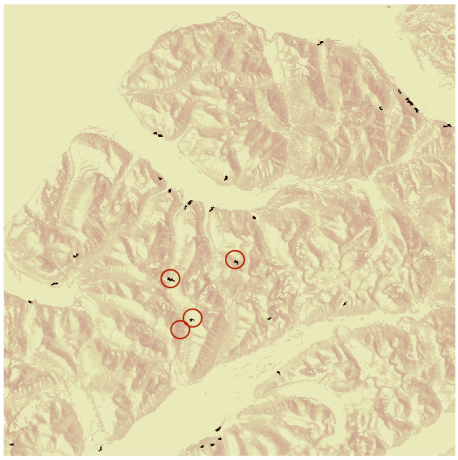

(b) 2.7dB

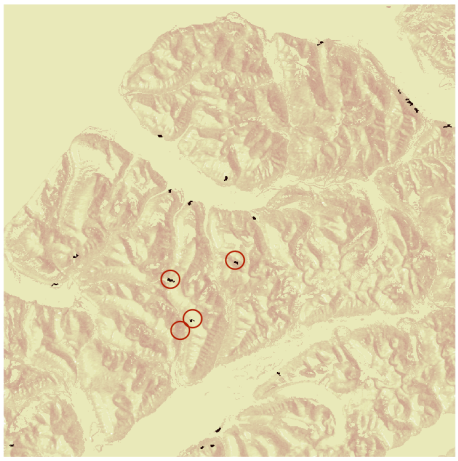

(c) 2.8dB

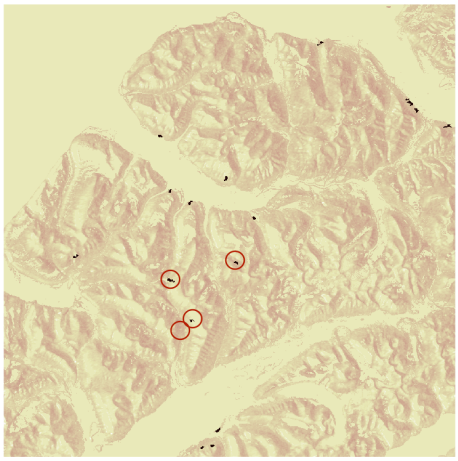

(d) 2.9dB

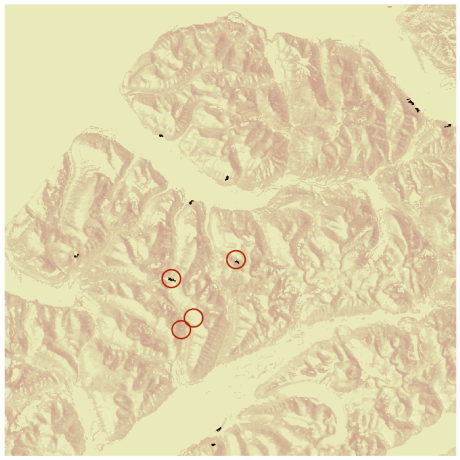

(e) 3dB

Figure B.11: Results of automatic detection method using post-classification filter 2: RSO filter and threshold values between 2.6dB and 3dB with steps of 0.1dB applied on ascending Sentinel-1A EW difference image from *'20150318'* and *'20150306'* in 'HH'-polarisation.

Bibliography

Buhler, Y., Bieler, C., Pielmeier, C., Frauenfelder, R., Jaedicke, C., Bippus, G., Wiesmann, A., and Caduff, R. (2014). Improved Alpine Avalanche Forecast Service. Technical report, SLF, NFI, Enveo, Gamma remote sensing, AAF and ESA.

Bühler, Y., Hüni, A., Christen, M., Meister, R., and Kellenberger, T. (2009). Automated detection and mapping of avalanche deposits using airborne optical remote sensing data. *Cold Regions Science and Technology*, 57(2-3):99–106.

Canadian Space Agency (2011). RADARSAT: Satellite characteristics. Retrieved on November 24, 2015 from http://www.asc-csa.gc.ca/eng/satellites/radarsat/radarsat-tableau.asp.

Colbeck, S., Akitaya, E., Armstrong, R., Gubler, H., Lafeuille, J., Lied, K., McClung, D., and Morris, E. (1990). The international classification for seasonal snow on the ground. Technical report, International Commission on Snow and Ice, World Data Center A for Glaciology, University of Colorado, Boulder, CO, USA.

Duda, R. O., Hart, P. E., and Stork, D. G. (2000). *Pattern Classification*. Wiley, second edition.

Eckerstorfer, M. and Christiansen, H. H. (2011a). The "High Arctic Maritime Snow Climate" in Central Svalbard. *Arctic, Antarctic, and Alpine Research*, 43(1):11–21.

Eckerstorfer, M. and Christiansen, H. H. (2011b). Topographical and meteorological control on snow avalanching in the Longyearbyen area, central Svalbard 2006-2009. *Geomorphology*, 134(3-4):186–196.

Eckerstorfer, M., Farnsworth, W., and Birkeland, K. (2014a). Potential dry slab avalanche trigger zones on wind-affected slopes in central Svalbard. *Cold Regions Science and Technology*, 99:66–77.

Eckerstorfer, M. and Malnes, E. (2015). Multi-sensor and multi-temporal avalanche debris detection using SAR and optical remote sensing data. *Submitted to Cold Regions Science and Technology*.

Eckerstorfer, M., Malnes, E., Frauenfelder, R., Domaas, U., and Brattlien, K. (2014b). Avalanche debris detection using satellite-borne radar and optical remote sensing. In *International Snow Science Workshop 2014*, pages 122–128.

ESA (2012). Report for mission selection: ESA SP-1324/2. Technical report, European Space Agency, Noordwijk, The Netherlands.

ESA Earth Online (2014). ESA EO missions: Sentinel 1. Retrieved on November 24, 2014 from https://earth.esa.int/web/guest/missions/esa-operational-eo-missions/sentinel-1.

European Avalanche Warning Services (2015). Basics. Retrieved on April 13, 2015 from http://www.avalanches.org/eaws/en/main_layer.php?layer=basics.

Gauthier, D., Conlan, M., and Jamieson, B. (2014). Photogrammetry of fracture lines and avalanche terrain: Potential applications to research and hazard mitigation projects. In *International Snow Science Workshop*, pages 109–115.

Greene, E., Atkins, D., Birkeland, K., Elder, K., Landry, C., Lazar, B., McCammon, I., Moore, M., Sharaf, D., Sternenz, B., Tremper, B., and Wiliams, K. (2010). *Snow, weather, and avalanches: Observational guidelines for avalanche programs in the United States*, volume Second Pri. The American Avalanche Association.

Lato, M. J., Frauenfelder, R., and Bühler, Y. (2012). Automated detection of snow avalanche deposits: segmentation and classification of optical remote sensing imagery. *Natural Hazards and Earth System Science*, 12(9):2893–2906.

Magagi, R. and Bernier, M. (2003). Optimal conditions for wet snow detection using RADARSAT SAR data. *Remote Sensing of Environment*, 84(2):221–233.

Malnes, E., Eckerstorfer, M., Larsen, Y., Frauenfelder, R., Jonsson, A., Jaedicke, C., and Solbø, S. a. (2013). Remote sensing of avalanches in northern Norway using Synthetic Aperture Radar. In *Proceedings of the International Snow Science Workshop 2013, Grenoble, France*, number 2, page 5. Northern Research Institute.

Malnes, E., Eckerstorfer, M., Storvold, R., Frauenfelder, R., and Jonsson, A. (2014). SeFaS - Monitoring avalanches in Northern Norway using SAR and UAV borne sensors. In *EARSEL Workshop on Land Ice and Snow*, Bern, Switzerland.

Malnes, E., Eckerstorfer, M., and Vickers, H. (2015). First Sentinel-1 detections of avalanche debris. *The Cryosphere Discussions*, 9(2):1943–1963.

Malone, J. (2014). From Europe and Asia, countries head to Svalbard to monitor the Arctic. *Horizon - The EU Research and Innovation Magazine*.

Martinez-Vazquez, A. and Fortuny-Guasch, J. (2008). A GB-SAR processor for snow avalanche identification. *IEEE Transactions on Geoscience and Remote Sensing*, 46(11):3948–3956.

McClung, D. and Schaerer, P. (2011). *The Avalanche Handbook*, volume 5. The Mountaineers Books, third edition.

McClung, D. M. (2002). The elements of applied avalanche forecasting, part II: The physical issues and the rules of applied avalanche forecasting. *Natural Hazards*, 26(2):131–146.

Nagler, T. and Rott, H. (2000). Retrieval of wet snow by means of multitemporal SAR data. *IEEE Transactions on Geoscience and Remote Sensing*, 38(2):754–765.

NASA (2015). Landsat overview. Retrieved on March 30, 2015 from http://www.nasa.gov/mission_pages/landsat/overview/index.html.

Norwegian Geotechnical Institute (2015). Ulykker. Retrieved on March 6, 2015 from www.ngi.no/no/snkoskred/Ulykker.

Norwegian Polar Institute (2015). TopoSvalbard. Retrieved on April 7, 2015 from toposvalbard.npolar.no.

Rees, W. (2013). *Physical Principles of Remote Sensing*. Cambridge University Press, second edition.

Rott, H. (1984). The analysis of backscattering properties from SAR data of mountain regions. *IEEE Journal of Oceanic Engineering*, 9(5):347–355.

Schweizer, J. (2008). Snow avalanche formation and dynamics. *Cold Regions Science and Technology*, 54:153–154.

Ulaby, F. T., Moore, R. K., and Fung, A. K. (1986). Microwave remote sensing: Active and passive; from theory to applications. *Arbor Ciencia Pensamiento Y Cultura*, 3(3):1120.

Wiesmann, A., Caduff, R., Strozzi, T., Papke, J., and Matzler, C. (2014). Monitoring of dynamic changes in alpine snow with terrestrial radar imagery. In *IGARSS*, pages 3662–3665.

Wiesmann, A., Wegmuller, U., Honikel, M., Strozzi, T., and Werner, C. (2001). Potential and methodology of satellite based SAR for hazard mapping. *Geoscience and Remote Sensing Symposium 2001. Proceedings. IEEE 2001*, 7:3262–3264.

Glossary

CT	Compression Test
DEM	Digital Elevation Model
ECT	Extended Column Test
EW	Extra Wide swath
FN	False Negative
FP	False Positive
FPR	False Positive Rate
GCP	Ground Control Point
GIS	Geographical Information System
GRD	Ground Range Detected
GRS	Geoscience and Remote Sensing
ICSI	International Commission on Snow and Ice
IW	Interferometric Wide swath
LOS	Line Of Sight
NASA	National Aeronautics and Space Administration
NIR	Near Infrared
NORUT	Northern Research Institute
OLI	Operational Land Imager
PRF	Pulse Repetition Frequency
Radar	Radio Detection And Ranging

RAR	Real Aperture Radar
ROI	Region Of Interest
RSO	Remove Small Objects
SAR	Synthetic Aperture Radar
SCNA	ScanSAR Narrow
SCWA	ScanSAR Wide
SLC	Single Look Complex
SNAPS	Snow, Ice and Avalanche Applications
SWE	Snow Water Equivalent
SWIR	Shortwave Infrared
TN	True Negative
TP	True Positive
TPR	True Positive Rate
TIR	Thermal Infrared
TIRS	Thermal Infrared Sensor
TU Delft	Delft University of Technology
UAV	Unmanned Airborne Vehicle
UF	Ultra Fine
UNIS	University Centre in Svalbard
Vis	Visible